DTU Library

Exploration of Archimedean Tessellations in Metal-Organic Frameworks

Chen, Hua

Link back to DTU Orbit

DTU

Exploration of Archimedean Tessellations in Metal-Organic Frameworks

Ph.D. Thesis | **Hua Chen**
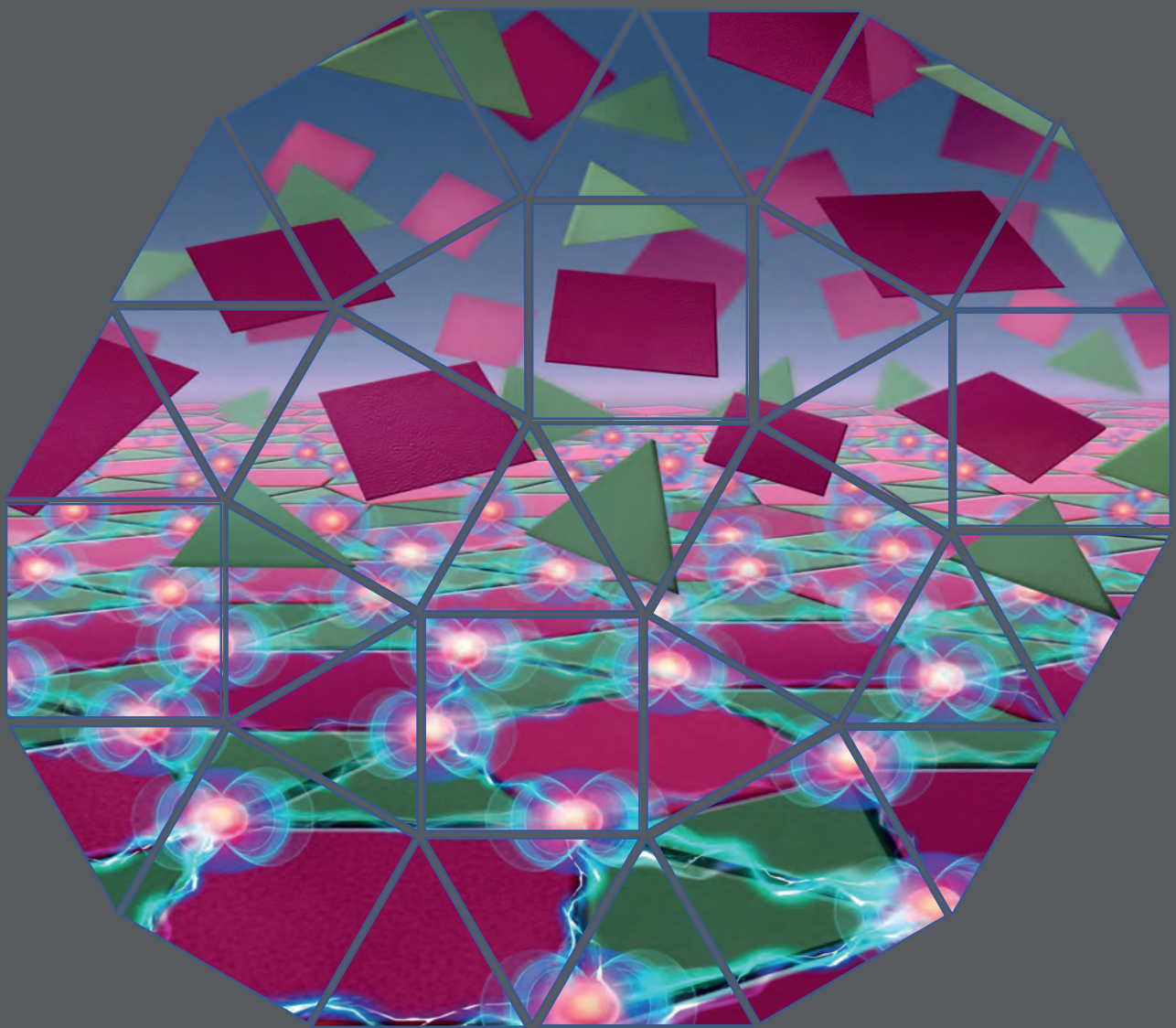
Exploration of Archimedean Tessellations in Metal-Organic Frameworks

Hua Chen

July 2022

Ph.D. Thesis

Department of Chemistry

Technical University of Denmark

Kemitorvet

2800 Kongens Lyngby

Table of Contents

List of abbreviations

AT	Archimedean tessellation
ac	alternating current
bipy	4, 4′-bipyridine
bipy$^{\cdot-}$	4, 4′-bipyridine radical
BDC	1,4-benzodicarboxylate
BTC	1,3,5-benzenetricarboxylate
CF	crystal field
CVD	chemical vapour deposition
DPB	1,4-di(pyridin-4-yl)benzene
dc	direct current
ddQC	dodecagonal quasicrystalline
en	ethane-1,2-diamine
EPR	electron paramagnetic resonance
IR	infrared
IVCT	inter-valence charge transfer
Ln	lanthanide
MeCN	acetonitrile
MOFs	metal-organic frameworks

NIR	near-infrared
pyz	pyrazine
PXRD	powder X-ray diffraction
QTM	quantum tunnelling of the magnetization
XAFS	X-ray absorption fine structure
SCXRD	single crystal X-ray diffraction
SMMs	single molecule magnets
SQUID	superconducting quantum interference device
T_B	blocking temperature
thf	tetrahydrofuran
U_{eff}	effective energy barrier
1D/2D/3D	one-/two-/three-dimensional

Preface

The work presented in this thesis is a result of my PhD studies from August 2019 to July 2022 under the supervision of Professor Kasper Steen Pedersen at the Department of Chemistry, Technical University of Denmark. The project was funded by the Danish National Committee for Research Infrastructure for funding (ESS Lighthouse "SMART"). Furthermore, a three-month external stay was conducted in the laboratory of Associate Professor Stergios Piligkos at the Department of Chemistry, University of Copenhagen.

Significant portions of the thesis' content are present in published and unpublished manuscripts attached at the end of the thesis. This dissertation is divided into several chapters. Chapter 1 introduces the concepts of metal-organic frameworks, magnetism, single-molecule magnets, tessellations, and tessellations in materials. Chapters 2-3 comprise the results and discussions. Chapter 4 presents the future outlook based on the findings. Chapter 5 is a brief discussion of the experiments conducted that are unrelated to the thesis topic. All the experiments and their results are provided in the attached document in detail.

Acknowledgements

First of all, I would like to show my great gratitude to Professor Kasper Steen Pedersen for letting me join your group as a Ph.D. student. Kasper's kindly attitude, guidance, support and vast knowledge about the chemistry have made it a pleasure having you as my supervisor. I am very grateful for your support during the project, which allowed me to learn so much and give me the opportunity to enter deeply into the field of MOFs and synthetic inorganic coordination chemistry. Thank you for your help measuring crystals and PPMS, even in the weekends or during vacations you helping as much as possible. Furthermore, I would also like to thank my second supervisor Professor Søren Kegnæs for your ever so friendly optimistic attitude and enormous support.

I am appreciative that I have been able to meet so many wonderful, intelligent, supportive people at the Department of Chemistry. Thank you to Dr. Mariusz Kubus for his friendly help with the technical support to SCXRD, crystal structure refinement and measure capillaries for PXRD. My sincere thanks also go to Professor René Wugt Larsen and Dr. Dmytro Mihrin for their encouragement and for the many IR measurements. Thank you to Associate Professor Susanne Mossin for helping measure EPR and analyze the data. I further acknowledge all the laboratory technicians and technical staffs, especially Johanne Marie Nielsen, David Frej Nielsen, Andreas Graff Pedersen, Ishaq Khaliqdad, Lars Egede Bruhn, John Nissen and Stephan Jean Jeannenot Galsøe, for their constant kindness and help. Many thanks to Jette Berg Nestén and Monica Esterajher Søndergaard at the reception for their help in sending sample packages and creating a warm and friendly atmosphere in the department.

Of course, I would like to thank all the former and current members of Kasper's group make our lab a friendly, helpful and fun working environment. Thank you

Abstract

Exploration of Archimedean Tessellations in Metal-Organic Frameworks is the thesis authored by Hua Chen describing the research conducted under the supervision of Professor Kasper Steen Pedersen and has been submitted to the Department of Chemistry at the Technical University of Denmark.

Among the classes of highly porous materials, metal-organic frameworks (MOFs) have excellent tunability, structural variety, and chemical and physical properties. MOFs are extended crystalline structures in which metal ions or clusters are connected by multitopic organic linkers. The diversity of metal ions and organic linkers allows an infinite number of combinations. MOFs have been used in several applications such as catalysis, gas sorption and storage, electronics, magneto-electronics, photonics, and quantum technology. The identification of quasicrystals that exhibit long-range order but lack translational symmetry introduced a new class of materials and was a revolutionary breakthrough in crystallography. The combination of quasicrystals and metal–organic structures results in promising multifunctional systems with great potential for applications. Their construction principles have been extensively studied, and they are represented by numerous complex amorphous and crystalline phases. However, the quasicrystalline order in MOFs has been difficult to identify thus far. In this study, Archimedean tessellations were constructed in bulk MOFs by exploiting the inherent tendency of lanthanides to exhibit high coordination numbers. The prepared MOFs were characterized and determined to be quasi-crystalline approximants that exhibited excellent magnetic properties.

The use of the plasticity of lanthanide (Ln) ions arising from the sufficient coordinative nature and the large ionic radii forms pentagonal bipyramidal nodes rarely found in the transition metal coordination chemistry. The self-assembly of

linear {LnI$_2$} nodes with ditopic organic spacers (4,4′-bipyridine (bipy)) results in the formation of MOFs with layers exhibiting rare Archimedean tessellations that mimic the structural motifs of quasi-periodic 2D materials. The prepared MOFs (**LnI$_2$(bipy)$_{2.5}$**) display intriguing magnetic properties and some of MOFs exhibit single molecule magnets behaviour.

Furthermore, the tunability of a coordination network was explored, starting out from **EuI$_2$(pyz)$_{2.5}$** (pyz = pyrazine). The **EuI$_2$(pyz)$_{2.5}$** processes the elongated triangular tiling that can be considered as defect 6-fold nodes, which paves a way for establishing the real 6-fold nodes. The exchange of metal ions and ligands results in forming completely different structures. Furthermore, the magnetic properties of prepared MOFs have also been demonstrated.

Danish Abstract

Exploration of Archimedean Tessellations in Metal-Organic Frameworks er en afhandling skrevet af Hua Chen, der beskriver forskning udført under ledelse af professor Kasper Steen Pedersen og indsendt til Institut for Kemi ved Danmarks Tekniske Universitet.

Blandt klasser af meget porøse materialer er metalorganiske rammer (MOF'er) uovertrufne i deres grad af indstillingsmuligheder og strukturelle variationer samt i deres brede kemiske og fysiske egenskaber. MOF'er er flerdimensionelle krystallinske strukturer, hvor metalioner eller -klynger er forbundet med multitopiske organiske ligander. Mangfoldigheden af metalioner og organiske ligander giver mulighed for et stort set uendeligt antal mulige kombinationer af disse. Derfor er MOF'er blevet anvendt til mange formål, herunder katalyse, gasadsorption og -lagring, elektronik, magneto-elektronik, fotonik og kvanteteknologi. Identifikationen af kvasikrystaller, som udviser langtrækkende orden, men mangler translationssymmetri, markerede både introduktionen af en ny klasse af materialer og var samtidig et revolutionerende gennembrud i krystallografien. Ved at kombinere kvasikrystaller med metal organiske netværk har man fundet lovende multifunktionelle systemer med store anvendelsespotentiale. Deres opbygningsprincipper er blevet undersøgt indgående og er repræsenteret i mange komplekse faser, både amorfe og krystallinske. Indtil nu har det imidlertid været vanskeligt at finde tegn på kvasikrystallinsk orden i MOF'er. I dette studie har vi konstrueret arkimediske tesseleringer i bulk-MOF'er ved at udnytte lanthanidernes naturlige tendens til at have høje koordinationstal. Disse kan betragtes som værende kvasikrystallinske tilnærmelser, der repræsentere en række sjældne eksempler på arkimediske tesseleringer i en MOF med lovende magnetiske egenskaber.

Som følge af deres tilstrækkeligt koordinerende natur og store ionradius kan lanthanidioner danne pentagonal bipyramidale komplekser, som sjældent findes i overgangsmetallers koordinationskemi. Ved at kombinere lineære $\{LnI_2\}$-centre med en ditopisk organisk ligand, 4,4'-bipyridin (bipy), resulterer i dannelsen af lagdelte metal organiske netværk, der udviser sjældne arkimediske tesseleringer, som efterligner strukturmotiver i kvasi-periodiske 2D-materialer. De fremstillede MOF'er (**$LnI_2(bipy)_{2.5}$**) udviser spændende magnetiske egenskaber, og hvoraf enkelte udviser magnetisk adfærd svarende til det fundet i enkeltmolekylemagneter.

Desuden blev effekten ved udskiftning af de organisker ligander undersøgt ved hjælp af **$EuI_2(pyz)_{2.5}$** (pyz = pyrazine). **$EuI_2(pyz)_{2.5}$** besidder den langstrakte trekantede tesselering, som kan betragtes som defekte 6-koordinerede centre, hvilket baner vejen for etableringen af egentlig 6-koordinering af metalcentrene. Udvekslingen af metalioner og ligander resulterer i dannelsen af helt forskellige strukturer. De magnetiske egenskaber af de fremstillede MOF'er er også blevet påvist.

14

Chapter 1. Introduction

Metal-organic frameworks (MOFs), are a class of materials consisting of metal ions or clusters connected by organic linkers to form one-, two-, or three-dimensional structures (**Fig. 1.1**), with high surface areas[1-5]. In the last 30 years, MOFs have been widely applied in gas storage,[6-10] gas separations,[11-15] catalysis,[16-20] owing their high porosity and chemical tunability.[21-25]

Metal ions or clusters   **Organic linkers**   **Metal-organic framework**
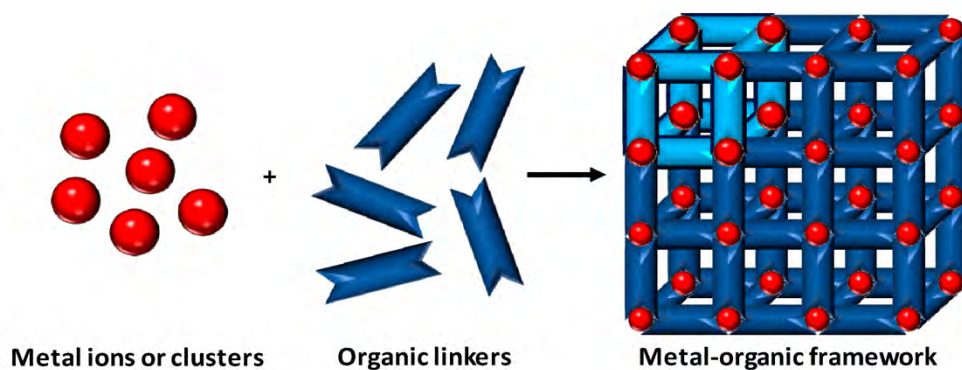
Fig. 1.1 Schematic of MOFs. The blue bar represents the organic linker, and the red ball represents the metal ion or cluster. The linkers and metal ions/clusters coordinate to form MOFs. Adapted with permission from reference.[26] Open access article.

In recent decades, the chemistry of MOFs has evolved rapidly, allowing the customization of size, shape, network topology, and surface area for a wide range of applications. According to crystal engineering principles, the design and synthesis of new MOFs with the desired physical and chemical properties require insights into the molecular and/or intermolecular interactions within the three-dimensional (3D) arrangement.

The structural features of MOFs are mostly governed by the large variety of coordination geometries employed by the metal ions, adoption of oligonuclear metal clusters as nodes, geometric features and versatility of the organic ligands, role of

counter ions, and reaction solvent.[27-31] Depending on the electronic structure of the metal ions, the different coordination geometries which can be adopted by the metal nodes, will determine the topology and dimensionality of the MOF. Transition metal ions (especially those in the first row), lanthanides, and alkaline earth metals, have been used as metal nodes because they exhibit a wide diversity of coordination numbers and geometries, thus providing synthetic and structural versatility. The use of rigid or flexible organic ligands has an enormous impact on the design of MOFs because flexible ligands provide a greater number of degrees of freedom than those by rigid ligands and can lead to unpredictable crystal structures.[31-35] The organic ligands used in MOFs normally contain one or more N-donor or O-donor atoms that act as a bridge between the metal ions. For example, pyridyl (pyrazine and 4,4′-bipyridyl derivatives),[36-41] carboxylates (aliphatic or aromatic containing one or more rings),[42-48] cyano compounds,[49-57] oxalic acid,[58-65] phosphonates,[66-74] and sulfonates[75-79] are the most popular ligands for the synthesis of MOFs.

1.1 Synthesis of metal-organic frameworks

The synthesis of MOFs is determined by several factors related to the reaction time, temperature, solvent used, nature of the metal ions and organic ligands, size of the nodes and their structural features, presence of counterions, and crystallization kinetics, which lead to nucleation and crystal growth. MOFs are typically synthesized in liquid phase by mixing ligands and metal salts. The solvents are chosen based on their reactivity, solubility, and redox potential because the activation energy and thermodynamics of each reaction are affected by the solvent. Despite the difficulties encountered in growing single crystals, solid-state synthesis methods are occasionally used. MOF crystals are often grown by the slow evaporation of the reaction solution. Most MOFs are synthesized under solvothermal (aqueous) conditions at high temperature and pressure, which is the conventional method. Recently, alternative synthetic methods such as chemical vapor deposition and

electrochemical, microwave, and sonochemical methods have been developed, which are less expensive, faster, and more reliable than the conventional method. Some synthetic methods for MOFs are discussed below:
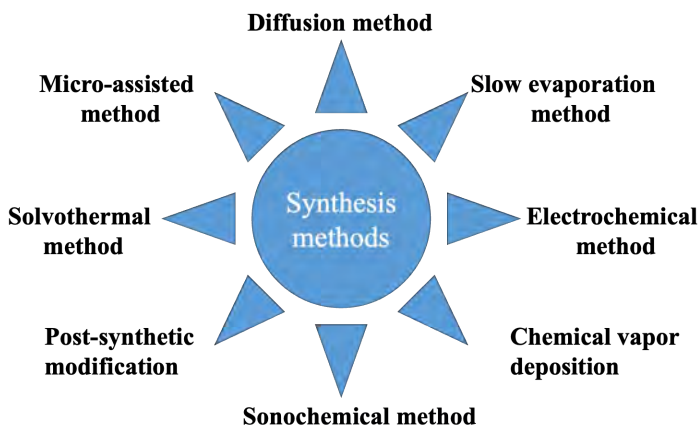
Fig. 1.2 Eight common synthetic methods to prepare MOFs. Reprinted the figure from reference.[80] Open access article.

1.1.1 Diffusion method

In this method, reagent solutions are layered over one another, separated by a layer of solvent, or are gradually diffused through a barrier submerged at a certain distance. In some instances, gel is used as a crystallization and diffusion mediator. Crystals are formed at the interface between the layers after the precipitated solvent gradually diffuses into a separate layer. The diffusion technique is employed when the product is not highly soluble. Yaghi et al. used the diffusion method to prepare MOF-5 and IRMOF-1 by diffusing triethylamine into a solution of $Zn(NO_3)_2$ and H_2BDC in DMF/chlorobenzene.[81]

1.1.2 Slow evaporation method

In this method, reagent solutions are mixed and left to evaporate slowly, forming crystals at a critical concentration that facilitates nucleation and crystal growth. Solvents with low boiling points are used in this method. Halper et al. used slow evaporation to prepare several MOFs. [82-86]

1.1.3 Solvothermal method

In this method, the reaction is conducted in closed vessels under autogenous pressure above the boiling point of the solvent.[83, 87-89] Most of the MOFs reported to date have been prepared using this method.[90-96] Teflon-lined autoclaves are used when high pressure and temperature conditions are required. Solvents with high boiling points are used in this method. [97-99]

1.1.4 Electrochemical method

MOF powders can be synthesized on an industrial scale using this method. The reaction mixture contains organic ligands and electrolytes, and the anode dissolves to provide the metal ions for the MOFs. This method is advantageous compared to the solvothermal method as it requires a lower reaction temperature and affords the desired MOFs rapidly under mild conditions. MOFs such as HKUST-1, ZIF-8, MIL-100 (Al), MIL-53 (Al), and NH_2-MIL-53 (Al) have been synthesized in electrochemical cells using this method, and the influence of several reaction parameters on their yields and textural properties has been studied.[100-106]

1.1.5 Sonochemical method

This method involves the chemical transformation of molecules under high-energy ultrasonic radiation (20 kHz to 10 MHz). When the reaction solution is irradiated by ultrasonic radiation, bubbles are formed, which generate short-lived local hotspots of high temperature and pressure, thereby promoting chemical reactions and the rapid formation of crystalline nuclei.[107-109] Using this method, high-quality MOF-5 and MOF-177 crystals were synthesized using 1-methyl-2-pyrrolidone as the solvent.

18

The crystals exhibited sizes of 5–20 μm and 5–25 μm, respectively, with shorter reaction times than those when the solvothermal method was used.[110-115]

1.1.6 Microwave assisted method

This method is commonly used to synthesize organic and nanoporous inorganic materials.[116] and has been used for the synthesis of metal clusters[117] and MOFs.[118-125] This method is advantageous because of its short reaction time, high yield, and low cost. Compared with the traditional solvothermal method, the microwave-assisted synthesis of HKUST-1 afforded the product in higher yield and required less reaction time.[126]

1.1.7 Post-synthetic modification

This method has been extensively used to prepare isomeric MOFs with different physical and chemical properties.[127-129] Post-synthetic modifications include the replacement of the structural units of MOFs using solvent-assisted ligand exchange and displacement of non-bridging ligands and metal junctions.[130]

1.1.8 Chemical vapor deposition (CVD)

In this method, gaseous substances are reacted with solids to produce solid deposits of high purity exhibiting the desired properties. Recently, researchers have successfully used CVD to prepare MOFs. [131-134]

1.2 Magnetism

A compound can be either diamagnetic or paramagnetic.[135] In diamagnetic materials, the magnetic flux density is lower inside the material than outside, whereas in paramagnetic materials, the magnetic flux density is greater inside the material than outside (**Fig. 1.3**).[136] All matter that originates from the interaction between paired electrons and an applied magnetic field exhibit diamagnetism.[136] When paired

electrons interact with an applied magnetic field, they produce a magnetic field that is oriented in the opposite direction to the applied magnetic field according to Lenz's law.[136] In contrast, paramagnetism occurs because of the angular momentum of the unpaired electrons interacting with an applied magnetic field.[136]

In the absence of a magnetic field, a paramagnetic material will have randomly oriented spins to minimize the energy of the system, as depicted in **Fig. 1.4**, resulting in no magnetization.[137] When a magnetic field is added, the magnetic moments align with the magnetic field. However, a thermal effect results in the opposite of this arrangement. In a paramagnetic material, if the magnetic behavior of a single paramagnetic ion is unrelated to its neighboring ions, it is termed as magnetically dilute, whereas if the behavior of the neighboring magnetic centers is not independent, then it is called magnetically concentrated.[137]

The main types of magnetic interactions are ferromagnetic, antiferromagnetic and ferrimagnetic (**Fig. 1.4**). In ferromagnetic interactions, adjacent spins tend to align parallel to each other. In antiferromagnetic interactions, adjacent spins are aligned antiparallel to each other. In ferrimagnetic interactions, adjacent spin centers are coupled antiparallelly, but adjacent magnetic moments have different magnitudes.
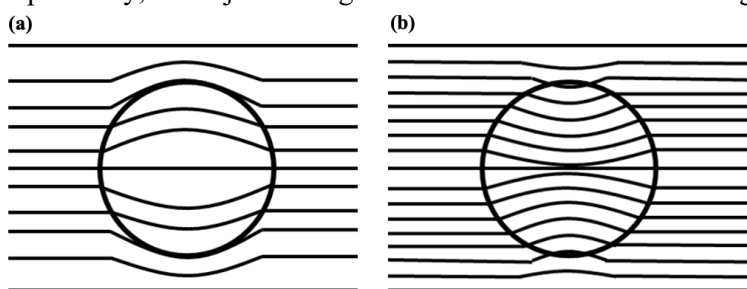
Fig. 1.3 Lines of flux in (a) diamagnetic and (b) paramagnetic materials. Reprinted with the permission from reference.[138] Open access article.
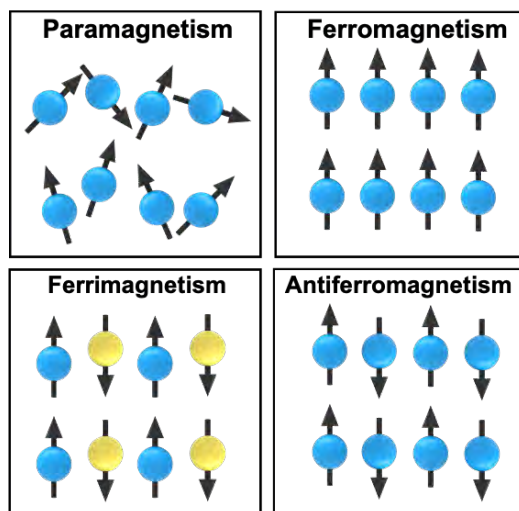
Fig. 1.4 Arrangement of the spins in different types of magnetic materials. All spins are aligned randomly in paramagnetic interactions, which can be categorized as ferromagnetic, ferrimagnetic, and antiferromagnetic interactions depending on the alignment of spins. Reprinted with permission from reference.[137] Copyright 2020 American Chemical Society.

1.3 Synthetic routes for magnetic metal-organic frameworks

A few factors must be considered when designing a magnetic material. To exhibit good magnetic properties, neighboring spins should have significant interactions, resulting in a long-range magnetic order.[139] Different synthetic strategies can be considered to obtain such magnetic MOFs, as shown in **Fig. 1.5**. One strategy is to use a short ligand that can shorten the distance between the metal centers and enable the interaction of the spins of the neighboring metal centers. A second strategy is to use a metal complex that can act as a ligand and spin center that can react with the metal nodes, resulting in long-range magnetic order. Using this strategy, oligonuclear complexes based on oxyamines[140] and phthalocyanine[141-144] have been synthesized. A third approach to promote exchange coupling between the metal

centers of MOFs is to add additional spin carriers to organic ligands such as radical ligands. [145, 146]

Use of short ligand   Use of metalloligand   Use of radical ligand
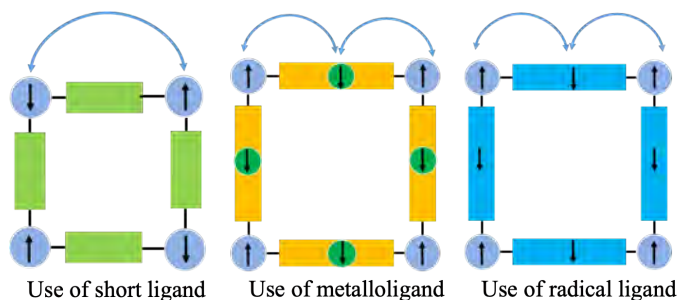
Fig. 1.5 Different synthetic routes for the preparation of magnetic MOFs. The rectangle, circle, arrow, and bent arrow represent ligands, metal nodes, spins, and interaction between spins, respectively. Reprinted with permission from reference.[139] Open access article.

1.4 Single molecule magnets

The traditional macroscopic magnet consists of magnetic domains and 3D regions of atoms/molecules within which the spins are aligned, which are divided by domain walls.[147] Hysteresis is apparent when magnetization vs. magnetic field (M vs. H) is plotted. This is related to the energy cost associated with breaking the domain walls to alter magnetization. Owing to the persistence of the domains, magnetization can persist for a long time after the field is removed.[147]

Single molecule magnets (SMMs) are nano-sized magnetic materials in which each molecule can act as a magnetic unit and exhibit paramagnetic behavior under blocking temperatures (T_B).[148] A SMM consists of individual molecules that do not interact and therefore have a single magnetic domain. Although there are no domain walls between the molecules themselves, these complexes are magnetically isolated and do not interact with each other.[147] As a result, SMMs exhibit properties associated with conventional macroscopic magnets.

SMMs can exhibit the hysteresis phenomenon of conventional magnets and thus have potential applications in quantum computing, molecular spintronics and ultra-dense information storage.[148-153] Since 1921, German chemists Fischer and Weinland first synthesized $Mn_{12}O_{12}(OAc)_{16}(H_2O)_4$ (also known as Mn_{12}) and in 1993, scientists Gatteschi and Christou reported that Mn_{12} shows hysteresis and frequency dependence in an alternative magnetic field.[154, 155] This has opened up a new interdisciplinary field of research that combines physics, chemistry, and materials. In recent years, compounds with higher T_B and energy barrier (U_{eff}) have been synthesized, enabling practical applications. Attempts were made to synthesize SMMs with better performance, and research on the hysteresis mechanism, origin of magnetic behavior, and SMMs is gradually progressing.[156-159] Therefore, SMMs have become an effective means to study the coexistence of quantum and classical effects and the link between quantum theory and classical magnetic theory, thus demonstrating its profound significance in theoretical research.[160, 161]

When an SMM is magnetized, the unpaired spins of molecules align in the magnetic field direction, which is the most energy-efficient orientation. When the magnetic field is removed, magnetization can be retained in that direction for some time at low temperatures. The larger the energy barrier of the spin reversal (U, **Fig. 1.6**) is, the longer the magnetization can be maintained and the higher the temperature at which it can be observed. The time required to reverse the spins is called the relaxation time of magnetization (τ).
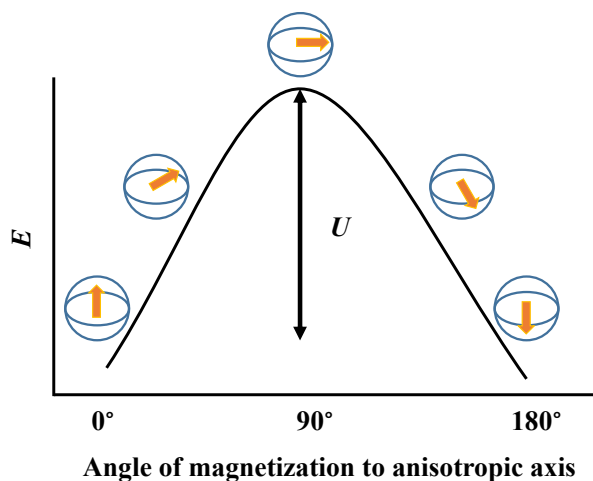
Fig. 1.6 Slow relaxation of magnetization in SMMs with an easy axis owing to an energetic preference for the magnetization to be aligned along the predominant axis of magnetic anisotropy. The spin must overcome the energy barrier U to reverse itself. Reprinted with permission from reference.[147] Copyright 2014 Elsevier.

The energy barrier to reverse the spin is related to magnetic anisotropy. A molecule is magnetically anisotropic if its magnetic properties depend on the orientation of the applied magnetic field; for many SMMs, it is preferable to have a magnetization orientation. This is called the "easy axis" and the most unfavorable orientation of magnetization is perpendicular to that axis and is called the "hard plane". Hence, there are different energies for different orientations of magnetic moments.[162] The difference between the energy levels is important for understanding magnetic behavior. The anisotropy of the magnetization is a result of the zero-field splitting (ZFS),[163-165] which can be simply quantified by the parameter D. The effect of ZFS is well understood for 3d metal complexes, but is more complicated for 4f complexes because of the strong spin-orbit coupling of Ln(III) ions.[166] In a 3d metal complex with total spin S, there are $2S+1$ possible substates exist, each with a spin quantum number M_S. M_S is the summation of the individual spin quantum numbers of unpaired electrons. Hence, the values of M_S range from $-S$ to S in increments of one, where

negative M_S values are "spin down" and positive M_S values are "spin up". Each M_S state corresponds to a different orientation of spin projection. All M_S states are degenerate if there is no ZFS, whereas the ZFS disrupts degeneracy. When D is negative, the largest magnitude $M_S = \pm S$ has the lowest energy. As a result, at low temperatures, magnetization can be trapped in one of the two $M_S = \pm S$ states because of the high-energy intermediate states and barrier U between the states. (**Fig. 1.7**)
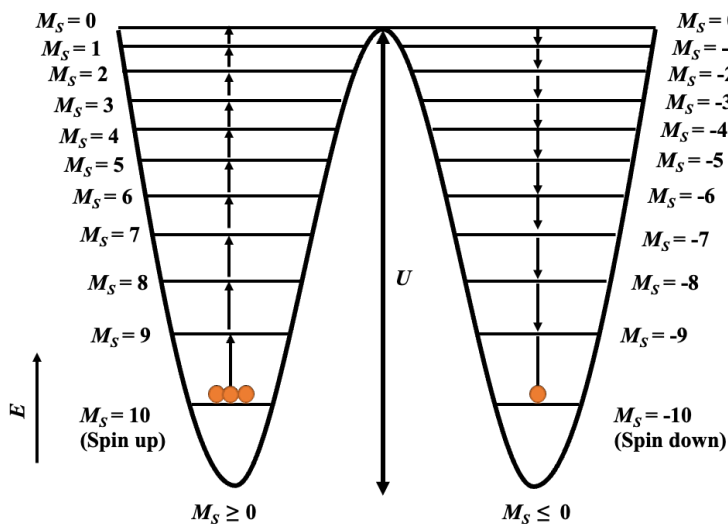
Fig. 1.7 Energy splitting of the $S = 10$ ground state of Mn_{12} into 21 sublevels owing to ZFS and relaxation of the magnetization from the "spin up" ($M_S = 10$) to "spin down" ($M_S = -10$) state at $H = 0$ and low temperature. Reprinted with permission from reference.[147] Copyright 2014 Elsevier.

For SMMs, the energy of the system varies with the external temperature, magnetic field strength, and several other factors. As shown in **Fig. 1.8**, in the absence of an applied magnetic field, the two degenerate ground states of the SMM have the same occupancy, although the spin directions are opposite; thus, magnetic behavior is not observed.[147] At low temperatures and when a magnetic field is applied, one state becomes more favorable, and the magnetization is trapped in one of the two M_S

ground states, reaching its saturation value.[147, 159] When the external magnetic field is removed, the split energy levels return to their initial degenerate state, and the occupancy of the states are evenly distributed. To achieve this, a fraction of the spins must cross an energy barrier to return to their original state, which was observed as a hysteresis loop.[167]
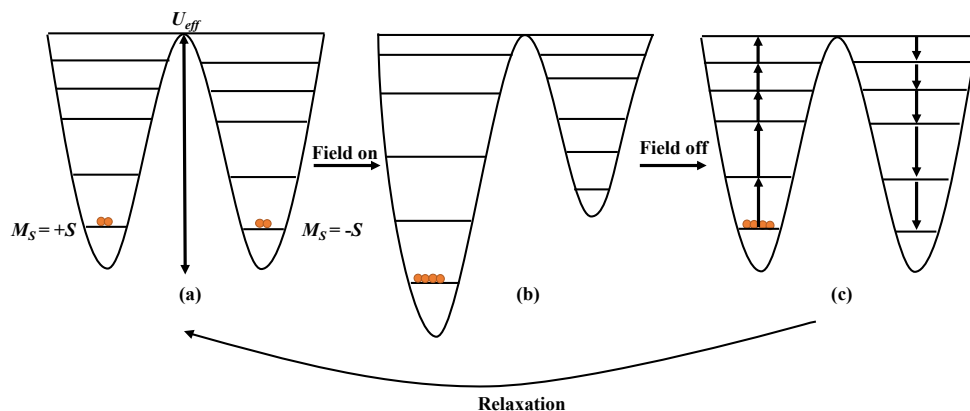
Fig. 1.8 Energy levels for a spin state S with a negative D at low temperatures. (a) State in zero field where the two states are equally populated, (b) state in which one well becomes more populated after the application of a magnetic field, and (c) state after the field has been removed and the system has returned to equilibrium in a stepwise manner. Reprinted with permission from reference.[168] Copyright Materials Research Society 2000.

Before discussing the 4f SMMs, the electron configuration of the Ln ions must be discussed, which will help in understanding lanthanide SMM behavior. The Ln atoms in the electronic ground state are characterized by the gradual filling of the 4f shell, with the general configuration $[Xe]4f^n6s^2$ (with the exception of La, Ce, Gd, and Lu, where the ground state configuration is $[Xe]4f^n5d^16s^2$). Hence, the most stable lanthanide ions are tripositive and obtained by the loss of one 5d and two 6s electrons or two 6s and one 4f electrons; Eu^{2+}, Ce^{4+}, and Tb^{4+} which have stable electronic configurations are the exceptions to this phenomenon. In Ln atoms, the electrons in the 4f shell are shielded by the completely filled 5s and 5p orbitals, and

26

their behavior is less affected by the coordination environment than that of the 3d series. The Ln ions exhibit an unquenched orbital momentum because the core-like character of the 4f orbitals prevents the crystal field from quenching the orbital momentum.

The energy level structure of the 4f states is determined by the following interaction: electron-electron interaction, spin orbital coupling, and crystal field. Compared to that of the 3d transition metal ions, the spin-orbit coupling is stronger owing to the higher nuclear mass, whereas its crystal field is lower because the 4f electrons that are located close to the core are shielded by 5s and 5p electrons. Because the spin-orbit coupling of Ln ions is strong, the total spin and orbital angular momentum (L) are strongly coupled, resulting in a total angular momentum (J). Therefore, describing their magnetic properties in terms of S is not sufficient. In contrast to that in the M_S states (for negative D), the M_J states do not have the maximum value as the ground state as they depend on the crystal field because J contains the spatial information of L. Thus, the magnetic behavior of lanthanide complexes is more complicated than that of 3d metal complexes.

The Russell–Saunders[169] coupling scheme is used to depict the electronic structure of Ln ions, where the total spin (S) and total orbital angular momentum (L) are strongly coupled to give the total angular momentum (J). J splits the ^{2S+1}L term into multiplets with different J values ($^{2S+1}L_J$), which is further split by the crystal field into $2J+1$ states; depending on the symmetry, these states can be a combination of M_J states, where M_J is the projection of J along the Z-axis. (**Fig. 1.9**). The magnitude of the M_J state splitting depends on the ligand.[140] To achieve a high performing SMM, the energy gap between the M_J ground state and the first excited M_J state should be as large as possible.[163] To ensure that a high magnetic moment can be maintained at temperatures where only the ground state is populated, the ground state should be doubly degenerate and consist of a large $|M_J|$ component.[170] Double

degeneracy is important because the SMM is defined by the bistability of its ground state and therefore the singlet ground state has no magnetic interest.[140] Kramers ions exhibit such doubly degenerate states in zero field. A Kramers ion has an odd number of electrons such as Dy(III) comprising f^9 electrons. A non- Kramers ion has an even number of electrons such as Tb(III) comprising f^8 electrons.[140] The $^{2S+1}L_J$ terms are energetically separated such that at room temperature or lower, only the ground state term is populated and contributes to the magnetic properties. Using Hund's rule, we can determine which J multiplet is the ground state. When the 4f shell is less than half-filled, $J = |L-S|$, whereas if the 4f shell is more than half-filled, $J = L+S$.[140] **Table 1** shows the ground state multiplets of the different trivalent lanthanide ions obtained by applying the above mentioned rules.
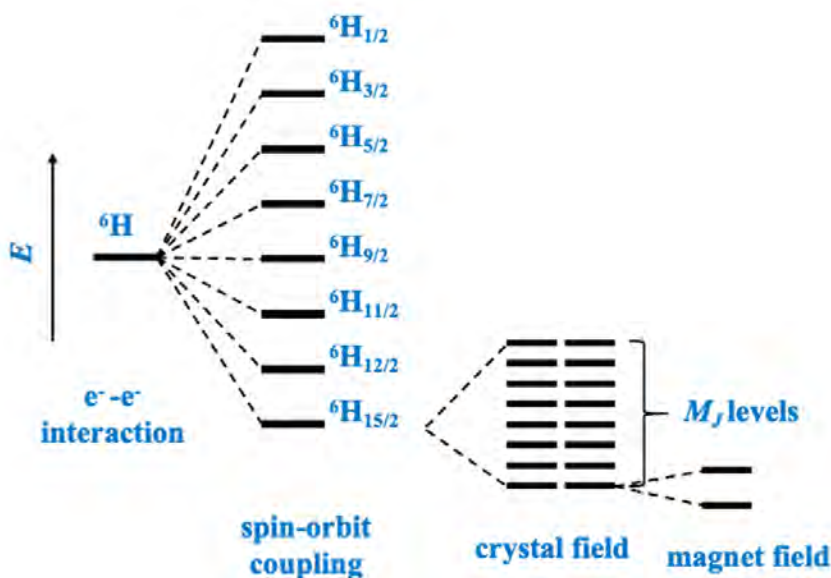
Fig. 1.9 Ground state electronic structure of the Dy(III) ion. The ground state term $^6H_{15/2}$ is split into $2J + 1$ states, each with the quantum number M_J. Reprinted with permission from reference.[147] Copyright 2014 Elsevier.

Table 1 Ground state multiplets of trivalent lanthanide ions

La	Ce	Pr	Nd	Pm	Sm	Eu
$^5F_{5/2}$	$^5F_{5/2}$	$^3H_4$	$^4I_{9/2}$	$^4I_4$	$^6H_{5/2}$	$^7F_0$
Gd	Tb	Dy	Ho	Er	Tm	Yb
$^8S_{7/2}$	$^7F_6$	$^6H_{15/2}$	$^5I_8$	$^4I_{15/2}$	$^3H_6$	$^2F_{7/2}$

The basic shape of the lowest *J* state can be mathematically described by the quadrupole moment of the f-electron charge cloud. (**Fig. 1.10**) The shape can be prolate (axially elongated), oblate (equatorially expanded), or isotropic (spherical). This shape change in the f-electron charge cloud is caused by the strong angular dependence of the f orbitals.
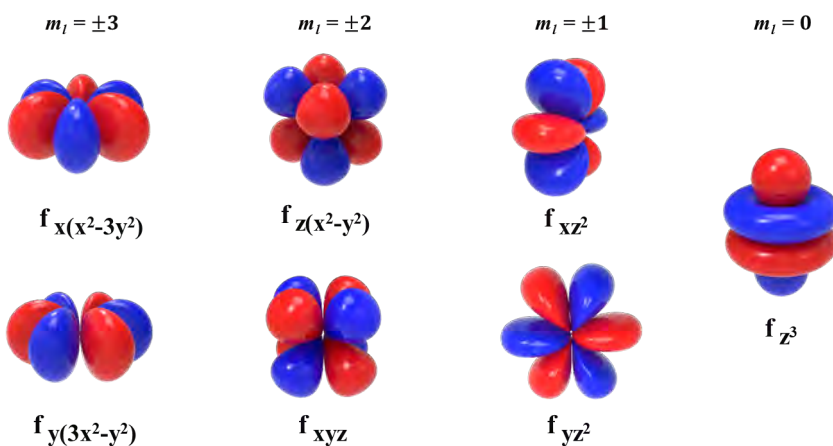
Fig. 1.10 Illustrations of the 4f orbitals from the highest magnitude m_l (most oblate shape) to the lowest magnitude m_l (most prolate shape). Reprinted with permission from reference.[170] Open access article.

Because orbital occupancy is determined by Hund's rule, the distribution of the free electron density for each ion can be approximated. (**Fig. 1.11**)
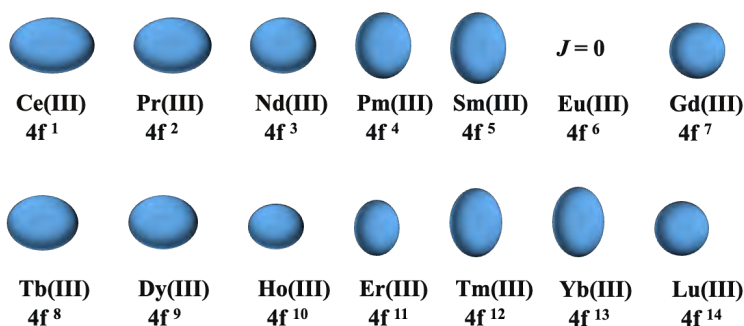
Fig. 1.11 Quadrupole approximations of the 4f-shell electron distribution for the trivalent lanthanides. Reprinted with permission from reference.[170] Open access article.

To maximize the magnetic anisotropy of an oblate ion, it should be placed in a crystal field where the electron density of the ligand is concentrated above and below the xy-plane. In this type of crystal field, the ground state has a bistable direction with M_J parallel and antiparallel to the molecular axis (large M_J) as these configurations can minimize repulsive contacts between the electron densities of the ligand and oblate ion. In contrast, a lower magnitude of the M_J orientation, such as the excited state, brings the electron density of the f-electron into direct contact with the ligand, resulting in a high-energy state (**Fig. 1.12a**). Therefore, for prolate ions, the electron density of the ligand should be concentrated in the equatorial plane to minimize contact with the f-electron density in the axial orientation (**Fig. 1.12b**).

Different spin relaxation pathways exist for lanthanide complexes (**Fig. 1.13**). In one pathway, the spin relaxes within the ground state doublet through the quantum tunnelling of the magnetization (QTM) (**Fig. 1.13a**). QTM is often the dominant relaxation pathway at low temperatures, but the QTM can probably decrease by increasing molecular symmetry and adding an extra static direct current (dc) magnetic field.[171-173] The other three relaxation pathways, the direct, Raman, and Orbach processes, are thermal activation processes.
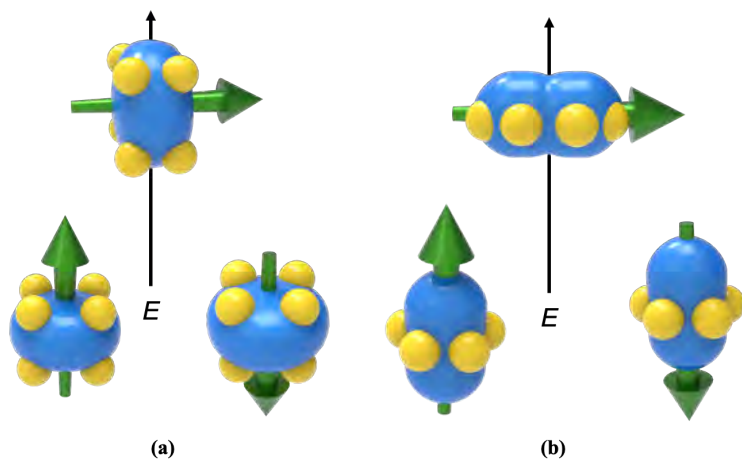
Fig. 1.12 Schematic of the f-orbital electron density in low- and high-energy configurations for a 4f ion with an (a) oblate or (b) prolate electron density. The green arrows demonstrate the orientation of the spin angular momentum coupled to the orbital moments. In the case of the oblate electron density, an axial sandwich-type crystal field minimizes the energy of the $M_J = J$ (high moment) state, making it suitable for designing single-molecule magnet. In contrast, in the case of the prolate electron density, an equatorial electron configuration minimizes the energy of the $M_J = J$ state. Reprinted with permission from reference.[170] Open access article.

In the direct relaxation pathway (**Fig. 1.13b**), the molecule transitions directly from the M_J ground state to the excited state along with tunnelling the energy barrier. The energy difference is absorbed by the spin system as a phonon.[159] In the Raman relaxation pathway (**Fig. 1.13c**), the spin is excited to a higher virtual state before the spin relaxes to the ground state.[159, 174] In the Orbach relaxation pathway (**Fig. 1.13d**), the spin is excited by an absorbed phonon and subsequently relaxes to the ground state, emitting a phonon.[159, 175, 176] The overall relaxation process can be described by the following equation:[162, 177]

$$\tau^{-1} = \frac{B_1}{1 + B_2 H^2} + AH^{n_1}T + CT^{n_2} + \tau_0^{-1}\exp\left(-\frac{U}{k_B T}\right)$$

where $\frac{B_1}{1+B_2H^2}, AH^{n_1}T, CT^{n_2}$, and $\tau_0^{-1}\exp\left(-\frac{U}{k_BT}\right)$ represent the QTM, direct, Raman, and Orbach processes, respectively; A, C, and τ_0 are free parameters; U is the energy gap between the ground state and the first excited crystal field state; k_B is the Boltzmann constant; n_1 is a variant exponent; $n_1 = 2$ for a non-Kramers ion; $n_1 = 4$ for a Kramers ion; and n_2 is a variant exponent that is usually 7 and 9 for non-Kramers and Kramers ions, respectively.[159, 178, 179]
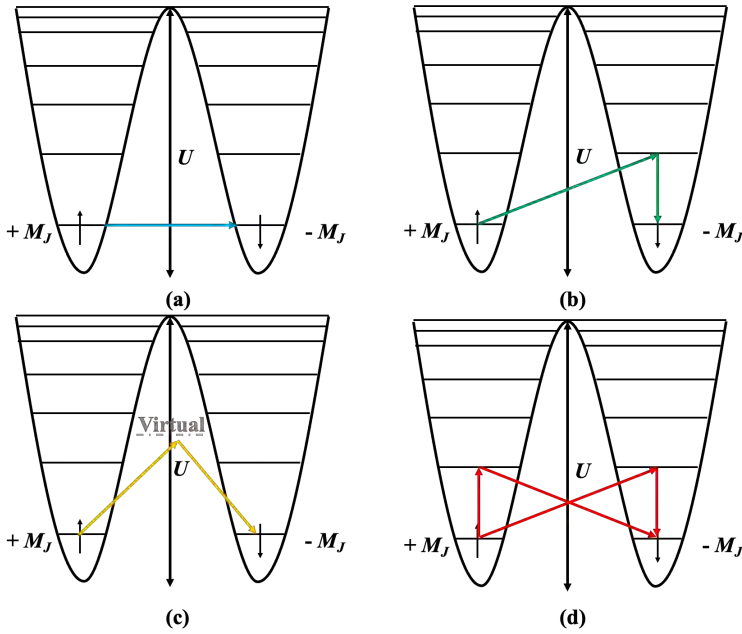
Fig. 1.13 Different relaxation processes: (a) Quantum tunnelling of the magnetization, and (b) direct, (c) Raman, and (d) Orbach relaxation processes. Reprinted with permission from reference.[179] Open access article.

A SQUID magnetometer is a powerful technique for measuring the SMM behavior and magnetic properties down to 2 K. The behavior of the compound in direct current (dc) and alternating current (ac) magnetic fields can be measured. Magnetization (M) describes how the energy changes with a magnetic field. In addition, magnetic

susceptibility (χ) describes the susceptibility of a compound for magnetization. The magnetic susceptibility can be described as follows:

$$\chi = \frac{\partial M}{\partial B}$$

where B is the applied magnetic field.

For free lanthanide ions, the magnetic susceptibility is expected to be close to the Curie constant at room temperature, and can be expressed as follows:[163]

$$\chi T = \frac{N_A g^2 \mu_B^2}{3k_B} J(J+1) A = \pi r^2 \approx \frac{g^2}{8} J(J+1) = C$$

where C is the Curie constant, N_A is Avogadro's number, g is the Landé factor, J is the total angular momentum and μ_B is Bohr magneton.

For lanthanide complexes, this phenomenon can indeed be observed experimentally as long as the crystal field splitting (CFS) is much smaller than room temperature. However, CFS usually tends to be larger than room temperature, in which case the magnetic susceptibility is smaller than the Curie constant.[163]

One strategy to assess potential SMM behavior is to measure the compound's response to an alternating current magnetic field. In this technique, a weak oscillating magnetic field is applied, which provides the in-phase (χ') and out-of-phase (χ'') components of magnetic susceptibility. If the alternating current susceptibility shows a non-zero χ'', it means that the magnetization of the compound does not alternate as quickly as the phase of the magnetic field. This is owing to the energy barrier of spin reversal, which means that the spins require time to reorient, indicating that the compound exhibits SMM behavior. The time that the molecule takes to reorient is the relaxation time (τ), which can be determined from the

maximum χ'' value as it can be expressed by the frequency as follows: $\tau = 1/(2\pi v)$.[163]

1.5 Tessellations

The tessellation of surfaces is found in pure art,[180] mathematics,[181-183] material physics[11] and molecular science.[184] Four centuries ago, Johannes Kepler discovered the existence of 11 tessellation lattices based on symmetric polygonal cells in the Euclidean plane. Three of these lattices consist of one type of polygon (squares, triangles, and hexagons) with regular tilings, whereas the other eight require a combination of two or more polygons (triangles, squares, hexagons, octagons, and dodecagons). Tessellation that involves more than one type of polygon is called Archimedean tessellation. Some of the 11 tessellations are shown in **Fig. 1.14**.
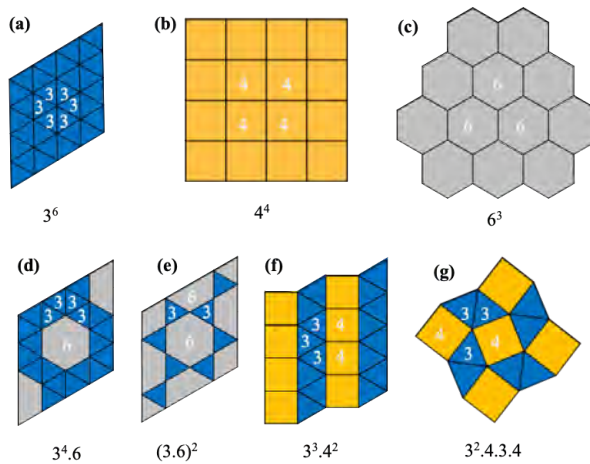
Fig. 1.14 Seven of the eleven regular (a, b, c) and semiregular Archimedean (d, e, f, g) tessellations in the Euclidean plane. Tilings from (a) to (g): triangular, square, hexagonal, snub hexagonal, trihexagonal (kagomé), elongated triangular, and snub square. Reprinted with permission from reference.[185] Open access article.

1.6 Tessellations in materials

Over the last few decades, surface-confined nanoarchitectures with supramolecules on their surfaces have been developed.[186-188] In surface-confined structures, the structure is determined by the arrangement of molecules and interactions between the molecules and substrates. Metal-directed assembly protocols are robust methods that result in spatial regularity and are often used for synthesizing surface-confined structures.[189, 190] Therefore, a wide variety of metal-directed assembly procedures were introduced to exploit the coordination ability of transition metals and their affinity to molecular species, especially those configured with carbonitrile,[191-193] pyridyl,[194-196] and carboxylate functional groups.[197-199] Urgel et al. investigated the formation of flexible carbonyl-lanthanide (cerium and gadolinium) coordination using scanning tunnelling microscopy and density functional theory.[200] Complex networks were prepared by employing linear linkers equipped with terminal carbonyl functional groups and by tuning the local rare-earth metals to molecular stoichiometry, as shown in **Fig. 1.15**.
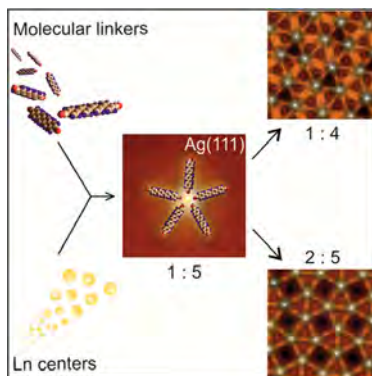
Fig. 1.15 Schematic of the five-vertex lanthanide coordination on surfaces. Adapted with permission from reference.[200] Copyright 2014, American Chemical Society.

Urgel et al. built two-dimensional quasicrystalline tilings on a well-defined gold substrate using rare-earth-directed assembly. By stoichiometrically controlling the Eu centers and functional linkers, they designed a porous network containing four-, five-, and six-fold vertices simultaneously (**Fig. 1.16**).[201]
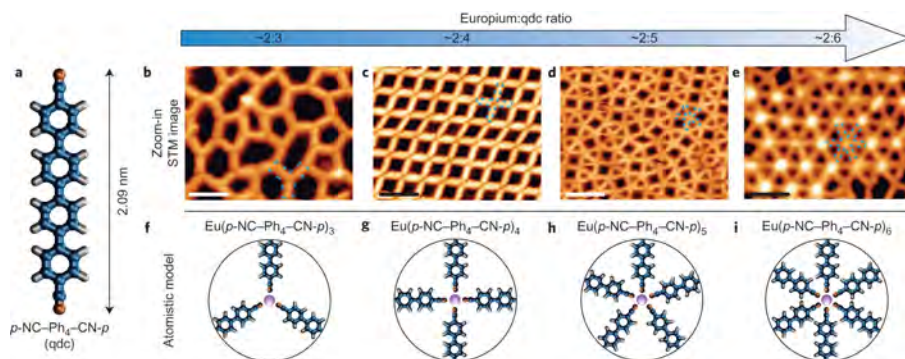
Fig. 1.16 (a) The para-quaterphenyl–dicarbonitrile (qdc) molecule. (b)–(e), High-resolution STM images of the distinct coordination networks designed at varying Eu:linker stoichiometries: (b) 2:3, (c) 2:4, (d) 2:5, and (e) 2:6; $V_{bias} = -1.2$ V, measured at 300 K; scale bar, 5 nm. (f)–(i), Atomistic models of (b)–(e) highlighting the distinct coordination nodes that stabilize the assemblies: (f) three-fold, (g) four-fold, (h) five-fold, and (i) six-fold. Color code: C, blue; N, brown; H, white; and Eu, purple. Adapted with permission from reference.[201] Copyright 2016, Nature Publishing Group.

However, in Urgel's work, all the compounds were layers rather than bulk materials. In 2020, Kasper Steen Pedersen et al.[185] reported a five-vertex node of Yb(II) in a two-dimensional (2D) coordination solid, $YbI_2(bipy)_{2.5}$. The semi-regular Archimedean tessellation structure approached quasicrystallinity and provided a route to achieve lanthanide-based metal–organic materials with intriguing photonic and magnetic properties. This indicates that metal–organic quasicrystalline phases can exist in a bulk material.
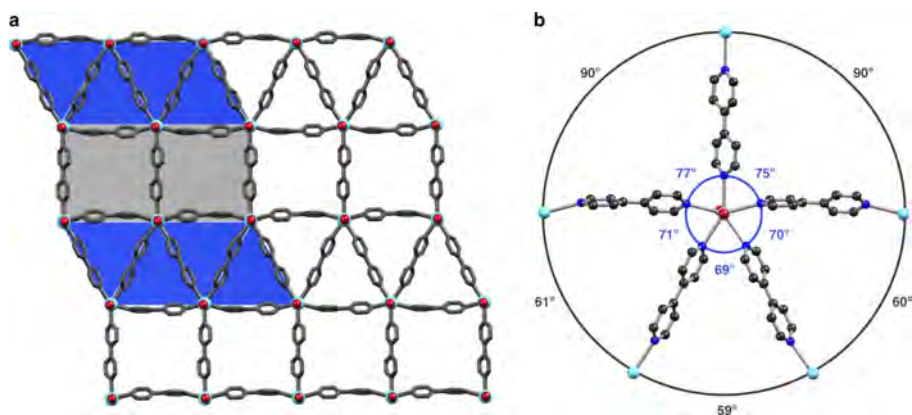
Fig. 1.17 Crystal structure of YbI$_2$(bipy)$_{2.5}$ as determined by single-crystal X-ray diffraction (SCXRD) at $T = 120$ K. (a) Fragment of the constituent coordination layers with an overlay of the ideal 33.42 tessellation. (b) Five-vertex node of trans- and bipy linkers in YbI$_2$(bipy)$_{2.5}$. The ∠N–Yb–N and ∠Yb–Yb–Yb are shown in blue and gray, respectively. Selected bond lengths (Å): Yb–I 3.1210(4), 3.1321(4), Yb–N 2.564 (4)–2.633(4). Yb···Yb separations (Å) amount to 12.14 and 12.25 for the squares, and 12.32, 12.14, and 12.34 for the triangles. Color codes: Yb, light blue; I, dark red; N, blue; C, gray; hydrogen atoms and co-crystallized CH$_3$CN have been omitted for clarity). Adapted with permission from reference.[185] Open access article.

# Chapter 2. Complex tessellations in magnetic metal-organic frameworks

The geometry of the organic linkers and coordination pattern of the inorganic metal ions or metal ion clusters can be controlled depending on the desired properties for the target MOF. The design and implementation of complexes and aperiodic 2D tessellations in molecular-based materials is a new strategy to imbue the materials with new photonic, electronic, and magnetic properties. The complex tessellations synthesized using this strategy will be different from their periodic counterparts.[202-204]

At the atomic and molecular levels, regular tessellations are ubiquitous in crystalline planes, surfaces of molecular crystals, and honeycomb structures such as graphene sheets and supramolecular lattices. Archimedean tessellations represent geometrically frustrated magnets[205] and can be used to synthesize photonic crystals.[206] Among the Archimedean tessellations, only the trihexagonal tiling (also called the Kagomé lattice) is widely reported in the literature.[207-213] The 2D dodecagonal quasicrystalline phase (**Fig. 2.1**, ddQC) is prominent in both hard and soft materials as well as in supramolecular networks. In the ddQC system, the periodicity disappears, and local 12-fold rotational symmetry appears. Typically, ddQCs often co-occur with periodic Archimedean tessellations, which are referred to as quasicrystal approximants.[214] For example, a single atomic layer of the quasi-crystalline phase in an MOF was achieved through the co-evaporation of Eu atoms and organic linkers.[201] Different types of tessellations are obtained based on the ratio of the metal ions and organic linkers (**Fig. 1.16**), which inspired this study.

To achieve an MOF with a two-dimensional ddQC, five- and six-fold nodes must be constructed along with five or six chemical bonds confined to the plane. Hence, most transition metal ions cannot be used in this construction, but larger metal ions such as those found in the f-block may be sufficiently large. However, the oxidation state of the 4f ion nodes remain uncharacterized. Moreover, quasicrystals have not been

realized in the more robust bulk coordination networks and MOFs.[202] This may be owing to the difficulty in crystallographic identification and absence of structures that can express quasicrystallinity.
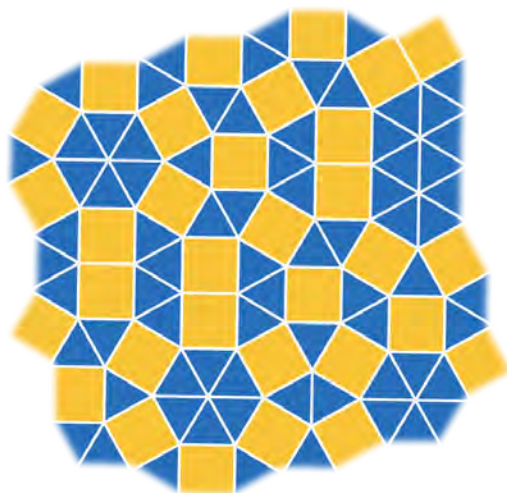
Fig. 2.1 Example of a random tiling in a dodecagonal quasicrystalline phase.

Smetana et al. proposed the first example of snub square tiling in a bulk metal–organic material using the pentagonal bipyramidal coordination of uranyl ions. Kasper Steen Pedersen et al. used $\{Yb^{II}I_2\}$ nodes as the five vertices of elongated triangular tiling to form **$Yb^{II}I_2(bipy)_{2.5}$**.[185] Lanthanides can be used to achieve Archimedean tessellations and ddQC phases because they can be effectively incorporated into various local coordination geometries owing to their coordinative plasticity. In addition, their weak interactions with ligands are compatible with those that are intrinsic to aperiodic structures. Divalent lanthanide units must be used to construct the **$YbI_2(bipy)_{2.5}$** framework. However, as previously mentioned, trivalent Ln ions are common. To overcome this problem, we developed a novel strategy for fabricating magnetic Archimedean tessellations incorporating trivalent lanthanide ions. Furthermore, we introduced radical ligands into MOFs. The presence of radical spins leads to strong magnetic interactions of the metal centers, which can be

controlled by the organic radical, metal ion, and the overlap of their magnetic orbitals containing an unpaired electron.[146]

In the following sections, the incorporation of Ln(III) (Ln = Gd, Dy, Tb, Ho, and Er) as a five-fold vertex node to form quasicrystalline approximants will be presented. The assembly of {LnI$_2$} nodes with ditopic ligands, 4,4′-bipyridine (bipy) and its anion radicals, provides a rare example of Archimedean tessellations in MOFs. The expression of Archimedean tessellations in Ln(III) coordination solids provides a blueprint for designing quasiperiodic MOFs with unique magnetic properties.

2.1 Synthesis procedures

2.1.1 Preparation of radical ligands

Tomonari et al. reported that the reaction of sodium with aromatic compounds generates anion radicals.[215] However, to date, only one single-crystalline compound bearing anion radicals, $Na^+(en)(bipy^{\bullet-})$ (en = ethane-1,2-diamine), has been reported.[216] Therefore, we reacted sodium with bipy to produce bipy radicals ($bipy^{\bullet-}$) whose formation is shown in **Fig. 2.2**.
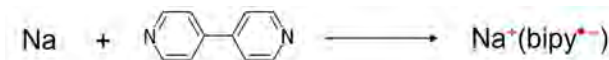
Fig. 2.2 Schematic of bipy radical formation.

The reaction of sodium with 2.5 molar equivalents of bipy in CH$_3$CN afforded a dark-blue solution. The electron paramagnetic resonance spectrum of the frozen solution showed a single narrow resonance at $g = 2.00$, which is attributed to the formation of an organic radical and is identical to that in the spectrum of $Na^+(en)(bipy^{\bullet-})$ ($g = 2.00429$) (**Fig. 2.3**).[216]
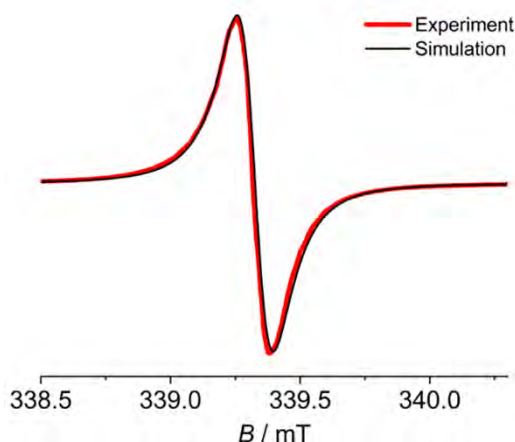
Fig. 2.3 Frozen-solution (CH_3CN) X-band (9.52 GHz) electron paramagnetic resonance spectrum at 77 K of the reaction product obtained from 1 equivalent of Na metal and 2.5 molar equivalent of bipy.

2.1.2 Preparation of $GdI_2(bipy)_{2.5}$

Powdered GdI_3 (135 mg, 250 µmol) and acetonitrile (14 mL) were vigorously stirred for 30 min. An acetonitrile solution containing 7 mL of 4,4′-bipyridine (195 mg, 1.25 mmol) and sodium metal (5.8 mg, 250 µmol) was added to the GdI_3 suspension with stirring. A dark-blue microcrystalline powder was immediately formed. The mixture was stirred for 10 min. The solid material was isolated by suction filtration and washed with cold acetonitrile (–20 °C; 2 ×10 mL). Yield: 90 mg (45%). Anal. calcd. (found) for $C_{27}H_{23}GdI_2N_6$ ($GdI_2(bipy)_{2.5}$·CH_3CN) %: C, 38.5 (38.2); H, 2.73 (2.81); N, 9.98 (9.91); I, 30.2 (29.7); Gd, 18.7 (18.3).

Dark-blue single crystals suitable for single-crystal X-ray diffraction (SCXRD) were obtained via slow diffusion (**Fig. 2.4**). Powdered GdI_3 (135 mg, 250 µmol) was placed at the bottom of a glass test tube (160 mm ×16 mm). Acetonitrile (14 mL) and $Na^+(bipy^{•-})$/bipy solution were gently layered on top of the powder. The test tube was covered and kept in a refrigerator (–20 °C) for 14 days.
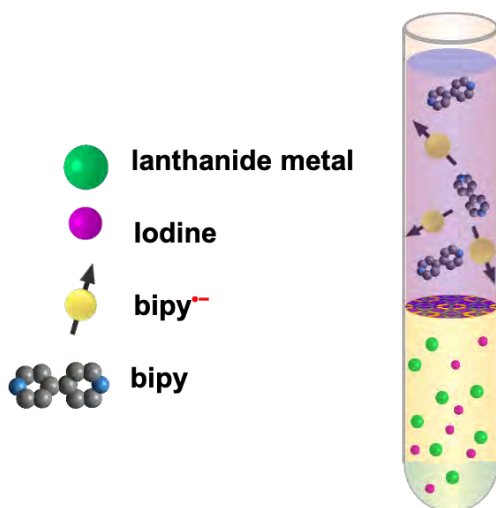
Fig. 2.4 Schematic of the crystal growth procedure.

2.1.3 Preparation of DyI$_2$(bipy)$_{2.5}$

The synthesis procedure of **DyI$_2$(bipy)$_{2.5}$** was same as that of **GdI$_2$(bipy)$_{2.5}$** where single crystals of **DyI$_2$(bipy)$_{2.5}$** were grown using DyI$_3$. Yield: 86 mg (43%). Anal. calcd. (found) for C$_{27}$H$_{23}$DyI$_2$N$_6$ (DyI$_2$(bipy)$_{2.5}$·CH$_3$CN): C, 38.2 (38.1); H, 2.73 (2.76); N, 9.91 (9.87); I, 29.9 (29.9); Dy, 19.2 (19.3).

2.1.4 Preparation of HoI$_2$(bipy)$_{2.5}$

The synthesis procedure of **HoI$_2$(bipy)$_{2.5}$** was same as that of **GdI$_2$(bipy)$_{2.5}$** where single crystals of **HoI$_2$(bipy)$_{2.5}$** were grown using HoI$_3$. Yield: 134.6 mg (66.6%). Anal. calcd. (found) for C$_{27}$H$_{23}$HoI$_2$N$_6$ (HoI$_2$(bipy)$_{2.5}$·CH$_3$CN): C, 38.12 (37.97); H, 2.71 (2.72); N, 9.88 (9.81); I, 29.88 (29.76); Ho, 19.41 (19.34).

2.1.5 Preparation of TbI$_2$(bipy)$_{2.5}$

The synthesis procedure of **TbI$_2$(bipy)$_{2.5}$** was identical to that of **GdI$_2$(bipy)$_{2.5}$** where single-crystals of **TbI$_2$(bipy)$_{2.5}$** were grown using TbI$_3$. Yield: 121.2 mg (60.39%).

Anal. calcd. (found) for $C_{27}H_{23}TbI_2N_6$ (TbI$_2$(bipy)$_{2.5}$·CH$_3$CN): C, 38.38 (38.85); H, 2.73 (2.85); N, 9.95 (10.63); I, 30.09 (29.19); Tb, 18.84 (18.26).

2.1.6 Preparation of ErI$_2$(bipy)$_{2.5}$

The synthesis procedure of **ErI$_2$(bipy)$_{2.5}$** was same as that of **GdI$_2$(bipy)$_{2.5}$** where single crystals of **ErI$_2$(bipy)$_{2.5}$** were grown using ErI$_3$. Yield: 121.2 mg (60.39%). Anal. calcd. (found) for $C_{27}H_{23}ErI_2N_6$ (ErI$_2$(bipy)$_{2.5}$·CH$_3$CN): C, 38.03 (36.91); H, 2.70 (2.64); N, 9.86 (9.49); I, 29.81 (29.12); Tb, 19.60 (19.23).

2.2 Archimedean tessellations and magnetic properties of GdI$_2$(bipy)$_{2.5}$

Two isomers of **GdI$_2$(bipy)$_{2.5}$**, **Gd** and **Gd′**, were formed simultaneously and could not be separated. The isomer mixture of **GdI$_2$(bipy)$_{2.5}$** was used in all measurements except in SCXRD. In the following section, the crystal structures of **Gd** and **Gd′** are elucidated.

2.2.1 Crystal structures of GdI$_2$(bipy)$_{2.5}$

The careful layering of the bipy/bipy$^{•-}$ solution on CH$_3$CN-covered GdI$_3$ yielded dark blue **Gd** crystals, which are suitable for SCXRD. **Gd** crystallized in the tetragonal $I4_122$ space group and had the ideal snub square tessellation (**Fig. 2.5**), where the five-fold {GdI$_2$} nodes are linked by the bipy/bipy$^{•-}$ linkers. Locally, the Gd–I bond lengths (3.04–3.05 Å) were slightly longer than those in [Gd^{III}I$_2$(thf)$_5$]$^+$ (thf = tetrahydrofuran, of 3.00 Å),[217] and significantly shorter than the Eu–I bonds found in Eu^{II}I$_2$(thf)$_5$ (3.22–3.24 Å),[218] which indicates the presence of Gd(III) and not Gd(II) in the **Gd**. The angle of I–Gd–I is linear (179.25°), and N–Gd–N angles are in the range of 67.9°–75.5° (**Fig. 2.6a**), indicating that the local coordination environment is similar to the D_{5h} symmetry. In addition, the crystal

structure of **Gd** along the crystallographic c-axis revealed the presence of interpenetrating 2D layers (**Fig. 2.6b**).
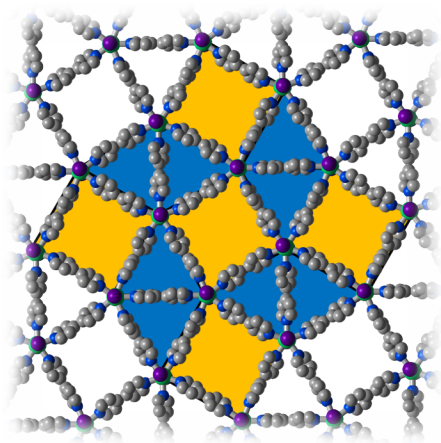
Fig. 2.5 Single-crystal X-ray structure of **Gd** viewed perpendicular to one of the snub square tiling layers. Color codes: Gd, green; I, purple; N, blue; C, gray. H atoms and co-crystallized CH_3CN molecules have been omitted for clarity.
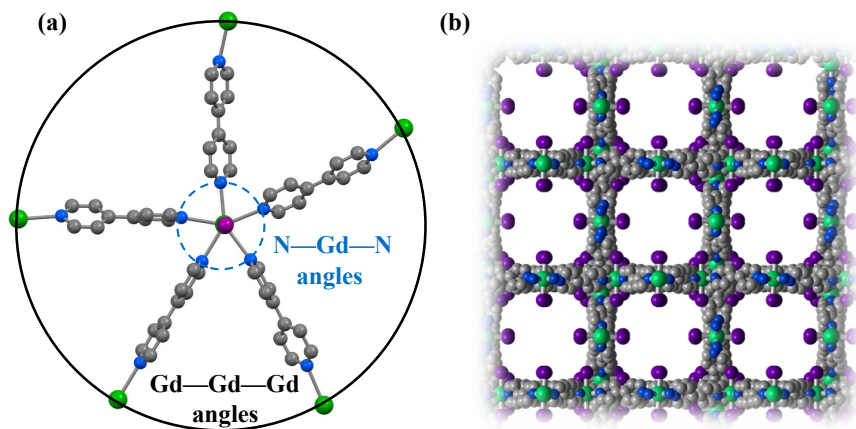
Fig. 2.6 (a) Fragment of the structure of **Gd** displaying the N–Gd–N (blue) and Gd–Gd–Gd angles (black). (b) Crystal structure of **Gd** along the crystallographic c-axis showing the

presence of interpenetrating 2D layers. Color codes: Gd, green; I, purple; N, blue; C, gray. H atoms and co-crystallized CH_3CN molecules have been omitted for clarity.

Goicoechea et al. previously demonstrated that the interpyridinic bond distance in bipy was shortened by ~4% under one-electron reduction.[216] Similarly, in this study, we observed that the two crystallographically independent Gd centers are each linked by three bipy$^{0/•−}$ ligands with longer C–C bond lengths (1.48–1.51 Å) and two bipy$^{0/•−}$ ligands with short C–C bond lengths (1.45 Å), corresponding to a ~4% reduction in the bond distances. Moreover, the bipy$^{•−}$ ligands are localized, forming $\{Gd^{III}_4(bipy^{•−})_4\}$ rhombi (**Fig. 2.7**).
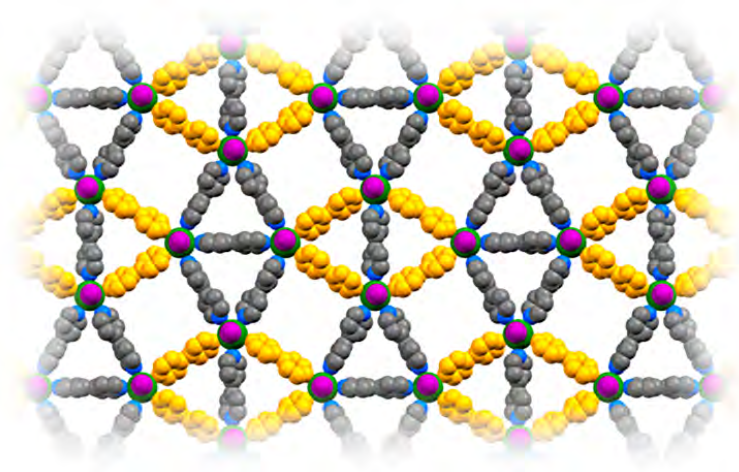
Fig. 2.7 Formation of $\{M^{III}_4(bipy^{•−})_4\}$ rhombi in **Gd** as suggested by single-crystal X-ray diffraction analysis. Color code: bipy$^{•−}$, yellow; bipy^0, grey; Gd, green; I, purple; N, blue; H atoms and co-crystallized CH_3CN molecules have been omitted for clarity.

Interestingly, in each crystallization batch, a few dark-blue crystals for **Gd′** were obtained. Structural analysis of **Gd′** indicated an identical chemical composition to $GdI_2(bipy)_{2.5} \cdot CH_3CN$. The space group of **Gd′** is triclinic $P\bar{1}$ and it has elongated

triangular tiling (**Fig. 2.8**). The tiling angle (α) of **Gd′** is 101° which is different from that of **YbI₂(bipy)$_{2.5}$** (90°). Therefore, **Gd′** can also be considered as a defective six-fold node, corresponding to $\alpha = 120°$.
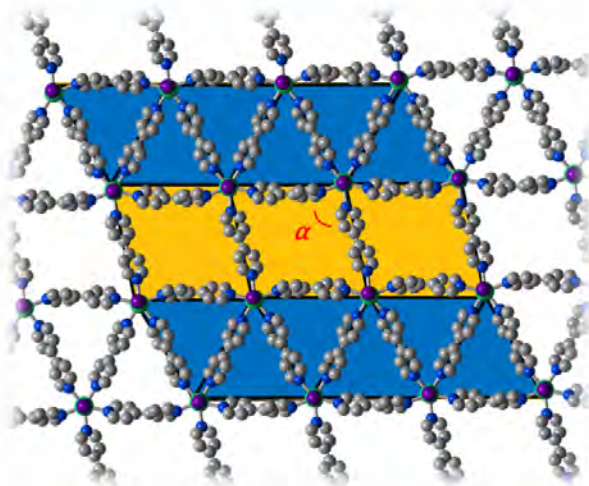
Fig. 2.8 SCXRD structure of the **Gd′**. Color codes: Gd, green; I, purple; N, blue; C, gray. H atoms and co-crystallized CH_3CN molecules have been omitted for clarity.

Locally, the Gd–I bond length is 3.02 Å and two-fifths of the bipy display short inter-pyridinic C–C bonds with an average length of 1.44 Å, whereas three-fifths exhibit normal, longer C–C bonds with lengths in the range 1.51–1.53 Å. This indicates the existence of Gd(III), bipy, and bipy$^{\bullet-}$ in **Gd′**. Furthermore, the N–Gd–N angles are in the range 70.94°–73.66°, and the I–Gd–I is linear (175.15°). In contrast to **Gd**, the layers of **Gd′** follow the AB-type stacking and are not porous (**Fig. 2.9**). (If the top layer is directly stacked on the bottom layer, the stacking type is called AA-stacking. Furthermore, AB-stacking can be obtained by shifting the top layer of AA-stacking.[219])

The powder X-ray diffraction (PXRD) pattern (**Fig. 2.10**) shows that **GdI₂(bipy)$_{2.5}$** has two phases, which is consistent with the overlap of the **Gd** and **Gd′** simulation

patterns and confirms **GdI₂(bipy)₂.₅** was successfully prepared. The PXRD results are consistent with the crystallographic results and indicate that the compound does not have other impurities.

Fig. 2.9 Schematic of layer-to-layer stacking of **Gd′**. Color codes: Gd, green; I, purple; N, blue; C, gray. H atoms and co-crystallized CH₃CN molecules have been omitted for clarity.

Fig. 2.10 Experimental powder X-ray diffraction data of **GdI₂(bipy)₂.₅** (black curve). Simulated data of **Gd** (blue curve) and **Gd′** (red curve) are obtained from the SCXRD.
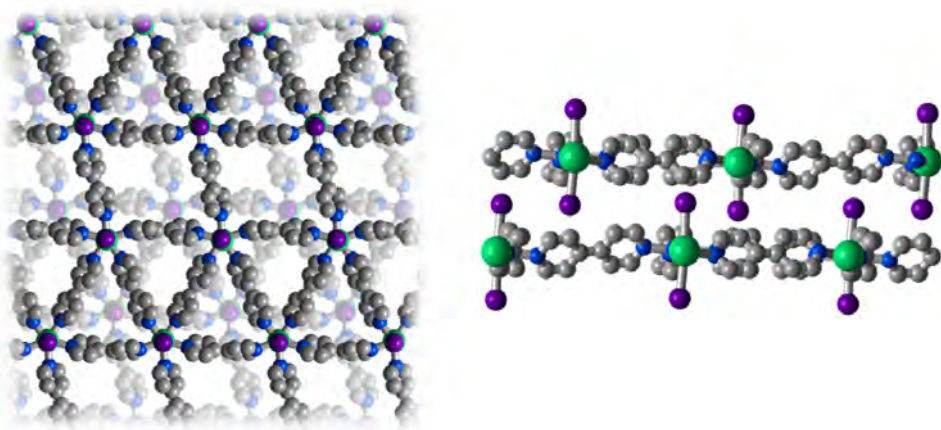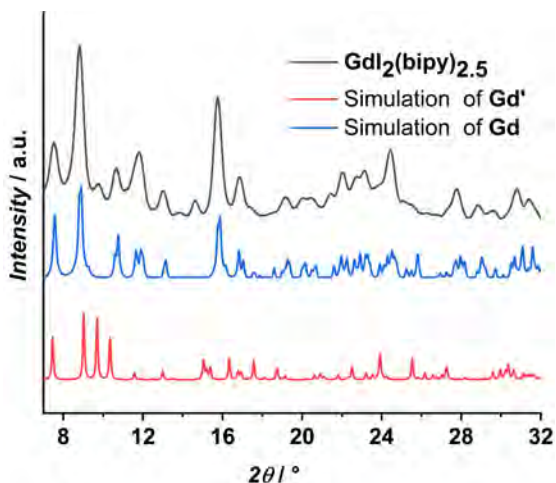
Owing to the mixed-valency in bipy$^{0/\bullet-}$, strong intervalence charge transfer (IVCT) transitions may occur in the mid- to near-infrared regions such as those observed for the transition metal complexes of mixed-valent 2,2′-bipyridine$^{0/\bullet-}$.[220] However, no such IVCT bands were observed for **GdI$_2$(bipy)$_{2.5}$** (**Fig. 2.11**), which is ascribed to the weakly covalent nature of the metal-ligand bonds and localization of the unpaired electrons, as determined from crystallography.
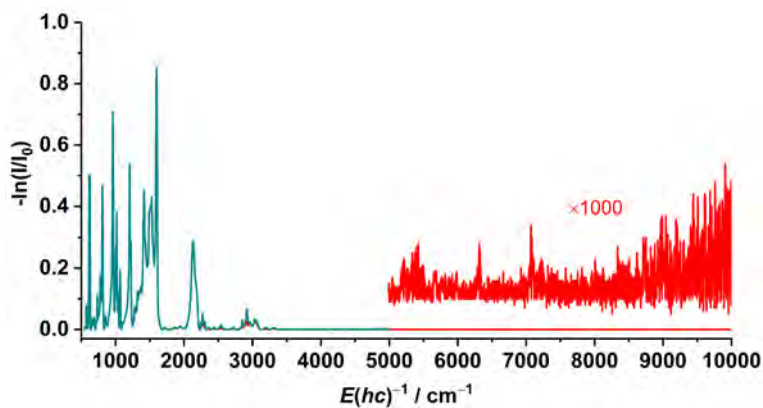
Fig. 2.11 Mid-IR/near-IR absorbance spectrum of **GdI$_2$(bipy)$_{2.5}$** obtained at room temperature. Weak gas-phase absorption lines are observed at approximately 5300–5400 cm^{-1} (OH stretching and bending fundamentals) and those at 7100-7200 cm^{-1} (first overtone of the OH stretching fundamental) correspond to uncompensated water vapor absorption.

2.2.2 Magnetic properties of GdI$_2$(bipy)$_{2.5}$

In last section, the crystal structures and characterizations of **GdI$_2$(bipy)$_{2.5}$** were introduced. Then I would like to discuss the magnetic properties of **GdI$_2$(bipy)$_{2.5}$**.

The room temperature value of the magnetic susceptibility-temperature products, χT, of **GdI$_2$(bipy)$_{2.5}$** is 8.6 cm^3 K mol^{-1}, which is comparable to the expected value of an uncorrelated pair of a Gd (III) ion (4f^7) and an organic radical ($S = 1/2$, $g = 2.0$) of 8.3 cm^3 K mol^{-1}. When the temperature was decreased, the χT product only slightly decreased, which is attributed to the relatively weak Gd^{III}-bipy$^{\bullet-}$

superexchange interactions. Moreover, the field-dependence of the magnetization, M vs. H, showed that M saturates at low temperature at 8.0 μ_B at 9 T, as predicted for one Gd^{III} and one bipy$^{\bullet-}$ for each formula unit (**Fig. 2.12**).

In addition, structural analyses confirmed the presence of $\{Gd^{III}_4(bipy^{\bullet-})_4\}$ rhombi. Therefore, adjacent Gd^{III} and bipy$^{\bullet-}$ are expected to be coupled via the superexchange mechanism. Thus, the magnetization data were modelled for an eight-membered ring of alternating Gd(III) ions and bipy$^{\bullet-}$ radicals using the spin Hamiltonian (Eq. 1) as follows:

$\hat{H} = g\mu_B B\sum_i \hat{S}_i + J\,(\hat{S}_{Gd1}\hat{S}_{rad1} + \hat{S}_{Gd2}\hat{S}_{rad1} + \hat{S}_{Gd2}\hat{S}_{rad2} + \hat{S}_{Gd3}\hat{S}_{rad2} + \hat{S}_{Gd3}\hat{S}_{rad3} + \hat{S}_{Gd4}\hat{S}_{rad3} + \hat{S}_{Gd4}\hat{S}_{rad4} + \hat{S}_{Gd1}\hat{S}_{rad4})$ (Eq. 1)

where $g = 2$ is the isotropic g factor for both Gd^{III} and the radical spins, μ_B is the Bohr magneton, B is the magnetic field, $\hat{S}$ is a spin operator indexed appropriately for each Gd^{III} and bipy$^{\bullet-}$, and J is the coupling constant. $g\mu_B B\sum_i \hat{S}_i$ represents the Zeeman interaction for all Gd^{III} and radical spins, and $J\,(\hat{S}_{Gd1}\hat{S}_{rad1} + \hat{S}_{Gd2}\hat{S}_{rad1} + \hat{S}_{Gd2}\hat{S}_{rad2} + \hat{S}_{Gd3}\hat{S}_{rad2} + \hat{S}_{Gd3}\hat{S}_{rad3} + \hat{S}_{Gd4}\hat{S}_{rad3} + \hat{S}_{Gd4}\hat{S}_{rad4} + \hat{S}_{Gd1}\hat{S}_{rad4})$ represents the superexchange interaction. Anisotropy terms are neglected because they are expected to be small for Gd^{III} and for the bipy$^{\bullet-}$ radicals. The χT data of **GdI$_2$(bipy)$_{2.5}$** was fitted to the spin Hamiltonian (Eq. 1), which resulted in the best-fit superexchange coupling constant $J/hc = 0.073(4)$ cm^{-1} (**Fig. 2.12a**, black trace).
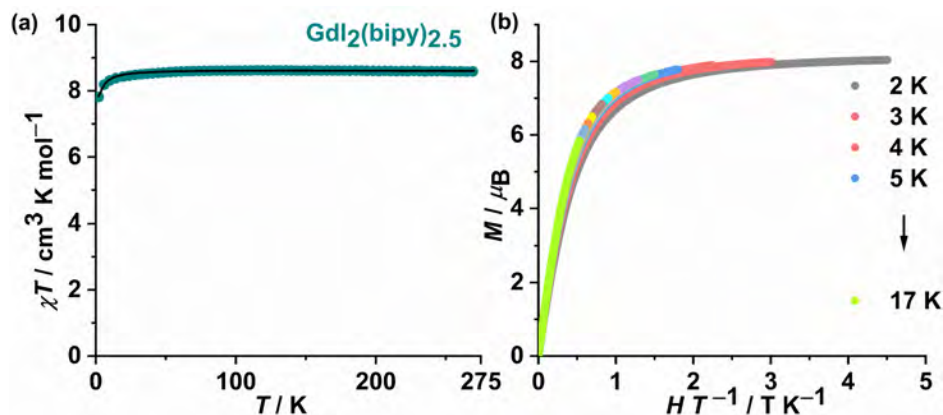
Fig. 2.12 (a) Temperature dependence of the magnetic susceptibility-temperature product, χT, for polycrystalline **GdI$_2$(bipy)$_{2.5}$** obtained under a direct current magnetic field of $H =$ 0.1 T. (b) The field dependence of the reduced magnetization, M vs. H/T, for **GdI$_2$(bipy)$_{2.5}$**.

2.3 Archimedean tessellations and magnetic properties of DyI$_2$(bipy)$_{2.5}$

2.3.1 Crystal structure of DyI$_2$(bipy)$_{2.5}$

The careful layering of the dark-blue solution of Na$^+$/bipy$^{•-}$/bipy on a CH$_3$CN-covered DyI$_3$ yielded dark-blue crystals of **DyI$_2$(bipy)$_{1.5}$** suitable for SCXRD. **DyI$_2$(bipy)$_{2.5}$** crystallized in the tetragonal $I4_122$ space group and features an ideal snub square tessellation of DyI$_2$(bipy)$_{2.5}$·xCH$_3$CN (**Fig. 2.13**), where five-fold {DyI$_2$} nodes are linked by the bipy/bipy$^{•-}$ linkers, which are isostructural to **Gd**. Locally, the Dy–I bond lengths (3.05 Å) were slightly longer than those in [Gd^{III}I$_2$(thf)$_5$]$^+$ (3.00 Å),[72] and significantly shorter than the Eu–I bonds found in trans-[Eu^{II}I$_2$(thf)$_5$] of 3.22–3.24 Å.[218] This indicates the presence of Dy(III) and not Dy(II) in **DyI$_2$(bipy)$_{2.5}$**. The I–Dy–I angle is linear (177.91°) and N–Dy–N angles are in the range 70.74°–74.11°, indicating that the local coordination environment is similar to the D_{5h} symmetry. Furthermore, the crystal structure of **DyI$_2$(bipy)$_{2.5}$** along the crystallographic c-axis shows interpenetrating 2D layers, similar to that in **Gd**.
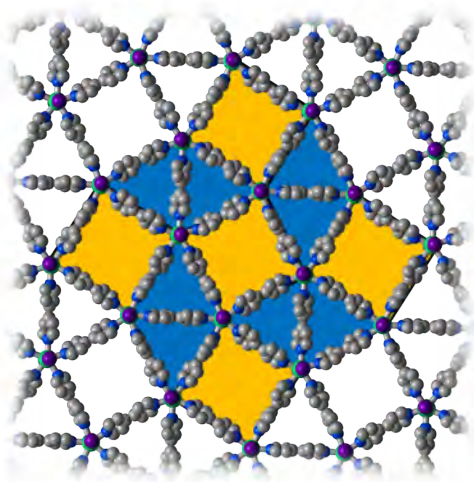
Fig. 2.13 SCXRD structure of **DyI₂(bipy)₂.₅** viewed perpendicular to one of the snub square tiling layers. Color codes: Dy, Green; I, purple; N, blue; C, gray. H atoms and co-crystallized CH₃CN molecules have been omitted for clarity.

2.3.2 Magnetic properties of DyI₂(bipy)₂.₅

The room temperature χT product of **DyI₂(bipy)₂.₅** was 13.8 cm³ K mol⁻¹ (**Fig. 2.14a**), which is only slightly lower than the expected value (14.2 cm³ K mol⁻¹) for a free Dy³⁺ ion with a ⁶H₁₅/₂ ground state and a bipy˙⁻ ligand. At lower temperatures, the χT product decreased slightly because of the depopulation of the excited ligand field states. Below 15 K, the χT product dropped dramatically, which may be attributed to magnetic superexchange interactions and the ligand field, resulting in only the ground state being populated. Furthermore, the non-overlap of the curves in the *M* vs. *H* data (**Fig. 2.14b**) for **DyI₂(bipy)₂.₅** indicates the existence of anisotropy.
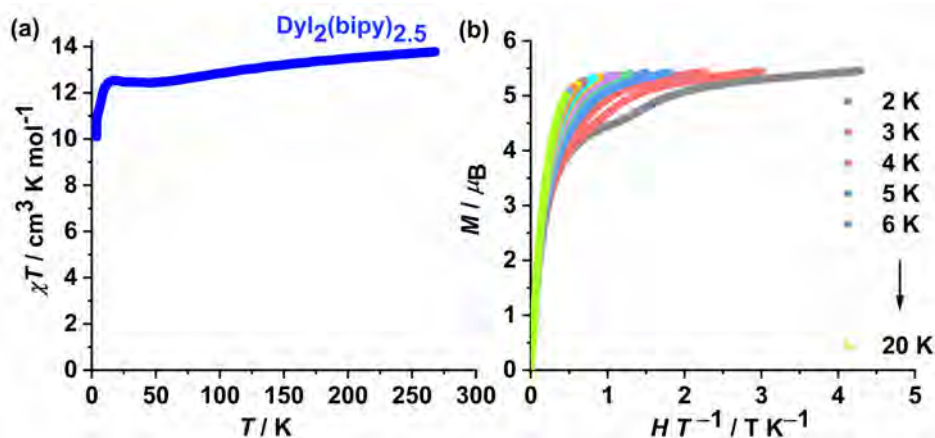
Fig. 2.14 (a) Temperature dependence of the magnetic susceptibility-temperature product, χT, for polycrystalline **DyI$_2$(bipy)$_{2.5}$** obtained under a direct current magnetic field of $H = 0.1$ T. (b) Field dependence of the reduced magnetization, M vs. H/T, for **DyI$_2$(bipy)$_{2.5}$**.

To investigate whether **DyI$_2$(bipy)$_{2.5}$** is an SMM or not, the relaxation time of the electronic spins was investigated using alternating current susceptometry. As mentioned in the introduction, this technique applies a weak oscillating magnetic field and reveals the in-phase (χ') and out-of-phase (χ'') components of the magnetic susceptibility. If χ'' is non-zero, it means that the magnetic moment of the molecule cannot reorient following the oscillation of the magnetic field, and the time that the molecules take to reorient is the relaxation time (τ) of the molecules.

We performed a temperature scan of **DyI$_2$(bipy)$_{2.5}$** which revealed a χ'' signal in the frequency-dependent alternating current susceptibility in the absence of a direct current magnetic field (**Fig. 2.15**). The non-zero χ'' signal indicates that **DyI$_2$(bipy)$_{2.5}$** has long relaxation time of the magnetization, indicating that **DyI$_2$(bipy)$_{2.5}$** is an SMM. Furthermore, **DyI$_2$(bipy)$_{2.5}$** shows one peak for each temperature, and as the temperature increased, the peaks shifted to higher frequencies, indicating that the thermally activated processes are active.

The temperature of the spin-lattice relaxation rate was approximated from the maxima of χ'' using the equation $\tau^{-1} = 2\pi \nu_{ac}$ (**Fig. 2.16**). It was expressed as the sum of a term governing the temperature-independent QTM and a term representing the two-phonon Orbach process, which is often used to rationalize the relaxation in lanthanide-based SMMs, as shown below:

$$\tau(T)^{-1} = \tau_{QTM}^{-1} + \tau_0^{-1}e^{-\Delta/k_B T} \quad \text{(Eq. 2)}$$

The τ vs T data are expressed by $\tau_{QTM} = 0.4$ μs and $\Delta/hc = 22$ cm^{-1} ($\tau_0^{-1} = 1.2 \times 10^{-7}$ s; **Fig. 2.16**, green trace). The tunnelling pathway is disrupted by the application of a sizable direct current magnetic field of 3 T (**Fig. 2.16**, red trace), and the τ vs. T data can be expressed using only the Orbach process ($\Delta/hc = 63$ cm^{-1}, $\tau_0^{-1} = 3.5 \times 10^{-10}$ s).
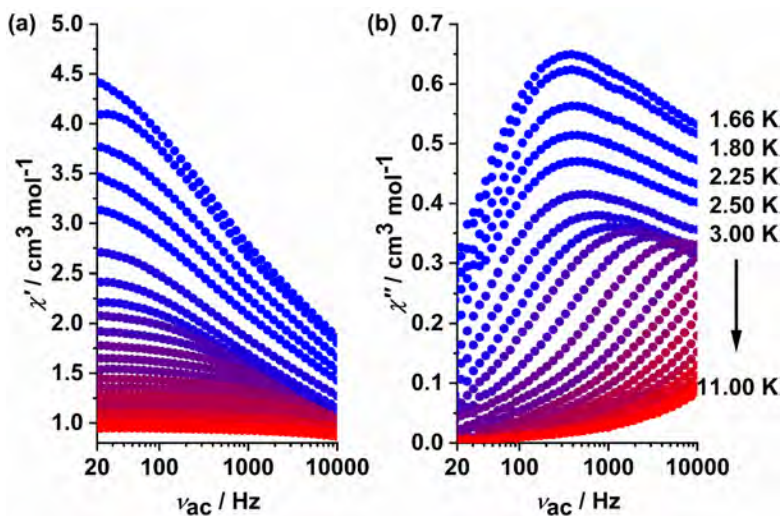
Fig. 2.15 (a) In-phase (χ') and (b) out-of-phase (χ'') alternating current susceptibility data for polycrystalline **DyI$_2$(bipy)$_{2.5}$** obtained at selected temperatures and in the absence of a static (direct current) magnetic field.
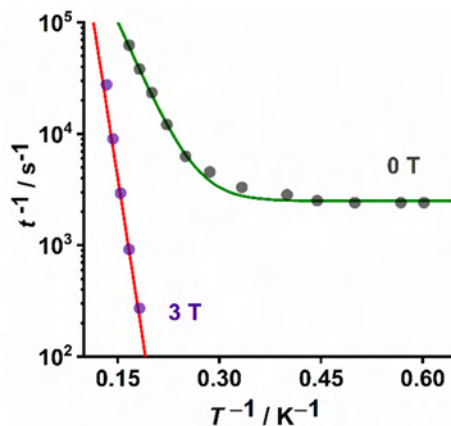
Fig. 2.16 Temperature dependence of the paramagnetic relaxation rate of **DyI$_2$(bipy)$_{2.5}$**, τ^{-1}, vs. temperature. Gray data points were obtained without static direct current magnetic field, and purple data points are obtained in a 3 T static direct current magnetic field.

2.4 Tunability of LnI$_2$(bipy)$_{2.5}$

To demonstrate the general applicability of the synthesis method, TbI$_3$, HoI$_3$, and ErI$_3$ were used to grow single crystals of the respective lanthanides. Single crystals of **TbI$_2$(bipy)$_{2.5}$**, **HoI$_2$(bipy)$_{2.5}$**, and **ErI$_2$(bipy)$_{2.5}$** were not obtained because they are intrinsically difficult to prepare and easily decompose. Hence, we prepared a crystalline powder of each compound. The PXRD patterns (**Fig. 2.17**) of all three compounds are consistent with the simulation patterns of **DyI$_2$(bipy)$_{2.5}$**, which confirms that **TbI$_2$(bipy)$_{2.5}$**, **HoI$_2$(bipy)$_{2.5}$**, and **ErI$_2$(bipy)$_{2.5}$** are pure and isostructural to **DyI$_2$(bipy)$_{2.5}$**.

54
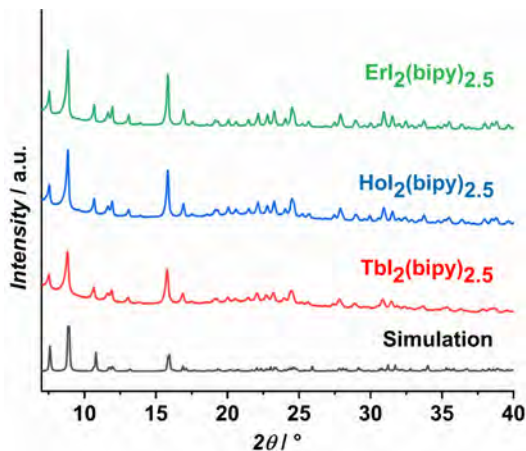
Fig. 2.17 Powder X-ray diffractograms of **TbI₂(bipy)₂.₅** (red), **HoI₂(bipy)₂.₅** (blue), and **ErI₂(bipy)₂.₅** (green) measured at room temperature. The simulation in black corresponds to the 120 K single-crystal X-ray structure of **DyI₂(bipy)₂.₅**.

The χT values of **TbI₂(bipy)₂.₅** are shown in **Fig. 2.18a**. The experimental χT value at room temperature was 11.69 cm³ K mol⁻¹, which is in good agreement with the Curie constant of the free Tb(III) ion and one radical (12.19 cm³ K mol⁻¹). The χT value decreased with decreasing temperature, which is attributed to the depopulation of the crystal field levels. Moreover, the field dependence of the magnetization was measured in the range 4–30 K, as shown in **Fig. 2.18b**. The non-overlap of the curves at different temperatures indicates the anisotropy of **TbI₂(bipy)₂.₅**. **HoI₂(bipy)₂.₅** and **ErI₂(bipy)₂.₅** also show similar behavior to **TbI₂(bipy)₂.₅** (**Fig. 2.19 and Fig. 2.20**). The experimental χT value of **HoI₂(bipy)₂.₅** at room temperature was 14.28 cm³ K mol⁻¹ which is comparable to the Curie constant of the free Ho(III) ion and one radical (14.44 cm³ K mol⁻¹). The experimental χT value of **ErI₂(bipy)₂.₅** at room temperature was 11.18 cm³ K mol⁻¹, which is consistent with the Curie constant of the free Er(III) ion and one radical (11.83 cm³ K mol⁻¹).
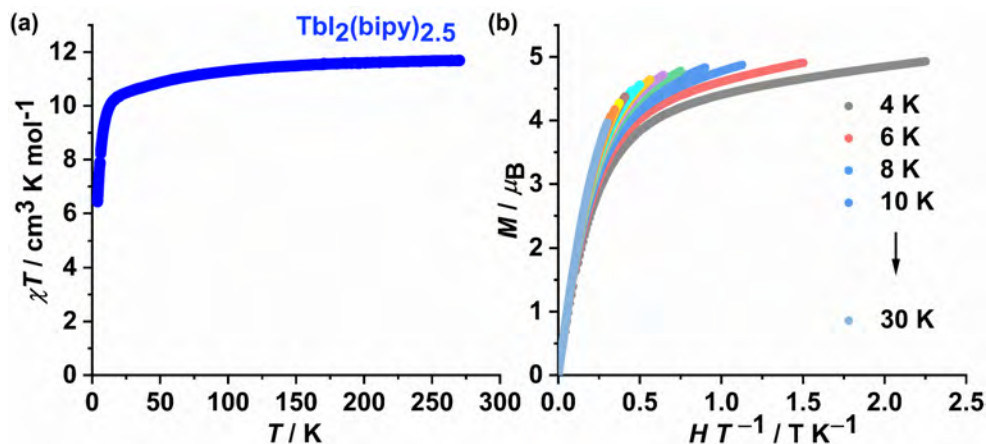
Fig. 2.18 (a) Temperature dependence of the magnetic susceptibility-temperature product, χT, for **TbI$_2$(bipy)$_{2.5}$** obtained under a direct current magnetic field of H = 1 T. (b) Field dependence of the reduced magnetization, M vs. H/T, for **TbI$_2$(bipy)$_{2.5}$**.
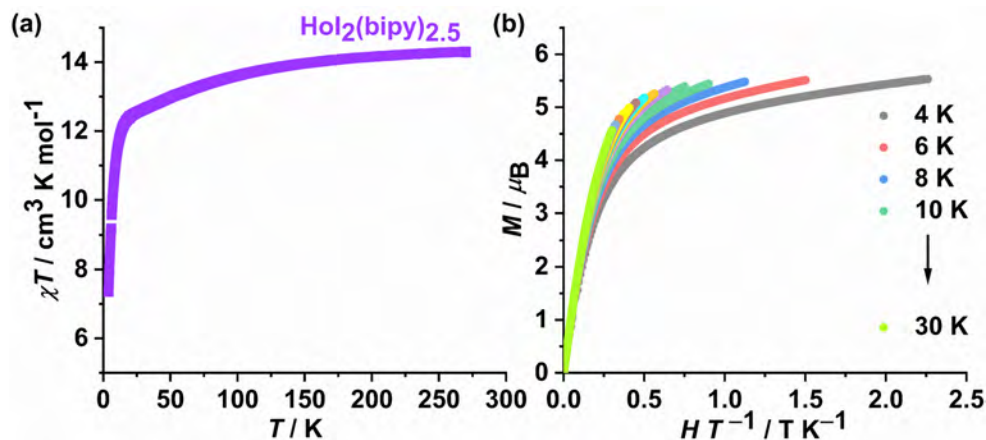
Fig. 2.19 (a) Temperature dependence of the magnetic susceptibility-temperature product, χT, for **HoI$_2$(bipy)$_{2.5}$** obtained under a dc magnetic field of H = 1 T. (b) The field dependence of the reduced magnetization, M vs. H/T, for **HoI$_2$(bipy)$_{2.5}$**.
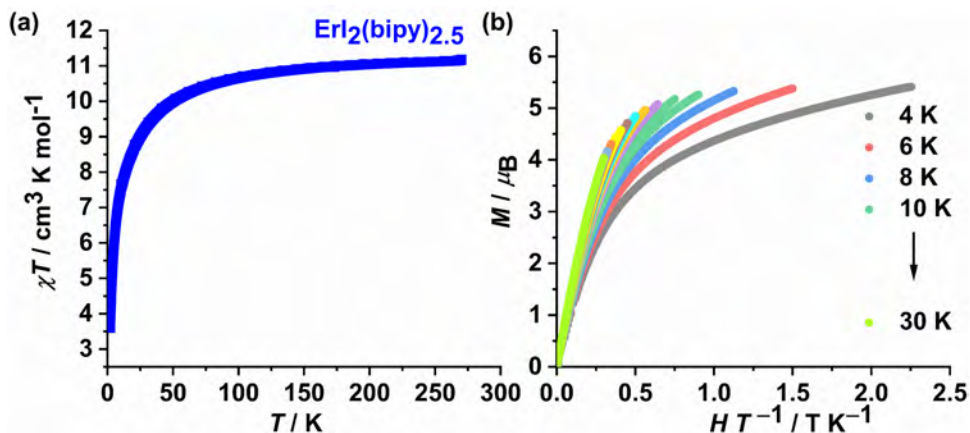
Fig. 2.20 (a) Temperature dependence of the magnetic susceptibility-temperature product, χT, for **ErI$_2$(bipy)$_{2.5}$** obtained under a direct current magnetic field of $H = 1$ T. (b) Field dependence of the reduced magnetization, M vs. H/T, for **ErI$_2$(bipy)$_{2.5}$**.

Tb-, Ho-, and Er-based complexes can normally exhibit SMM behaviour.[221-235] To investigate whether the **TbI$_2$(bipy)$_{2.5}$**, **HoI$_2$(bipy)$_{2.5}$**, and **ErI$_2$(bipy)$_{2.5}$** are SMMs or not, the relaxation time of the electronic spins was measured using alternating current susceptometry.

The frequency dependency of the alternating current susceptibility at 2 K was measured in different static applied magnetic fields. **Fig. 2.21a** shows the frequency dependency of **TbI$_2$(bipy)$_{2.5}$**. A non-zero χ'' signal was observed, indicating that **TbI$_2$(bipy)$_{2.5}$** exhibits SMM behavior. In the absence of a direct current magnetic field, no χ'' signal was observed at 2 K for either **HoI$_2$(bipy)$_{2.5}$** (**Fig. 2.21b**) or **ErI$_2$(bipy)$_{2.5}$** (**Fig. 2.21c**), indicating the presence of high QTM. When a direct current magnetic field is applied, QTM can be partially suppressed or fully quenched. All three compounds showed weak non-zero χ'' signals, and the peaks for all measured magnetic fields were outside the measured frequency. According to the equation $\tau = 1/(2\pi v)$, the higher the frequency, the shorter the relaxation time, which indicates weak SMM behavior; therefore, further measurements were not taken.
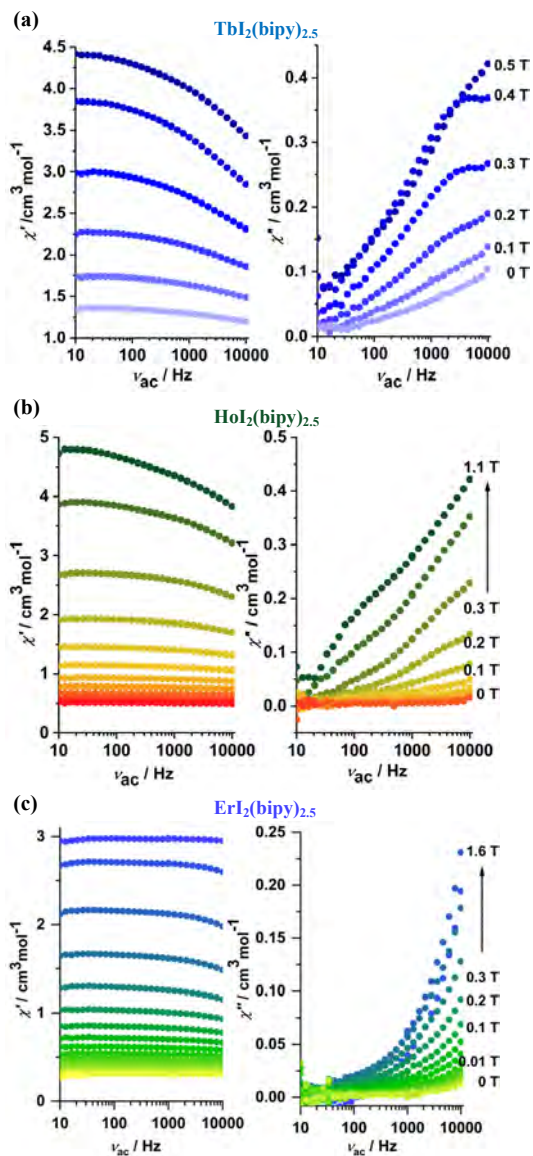
Fig. 2.21 Frequency dependence of the alternating current susceptibility for (a) **TbI₂(bipy)₂.₅,** (b) **HoI₂(bipy)₂.₅**, and (c) **ErI₂(bipy)₂.₅** in varying magnetic fields.

The optimal magnetic field to measure the frequency dependence of the alternating current susceptibility for **TbI₂(bipy)₂.₅** was determined to be 0.4 T. Using the 0.4 T direct current magnetic field, the temperature scan of **TbI₂(bipy)₂.₅** was performed. **TbI₂(bipy)₂.₅** showed zero χ'' signals below 10 K, and the χ'' signals were observed with decreasing temperature. Furthermore, no peaks were observed in the measured frequency range, which confirmed the weak SMM behavior (**Fig. 2.22**).
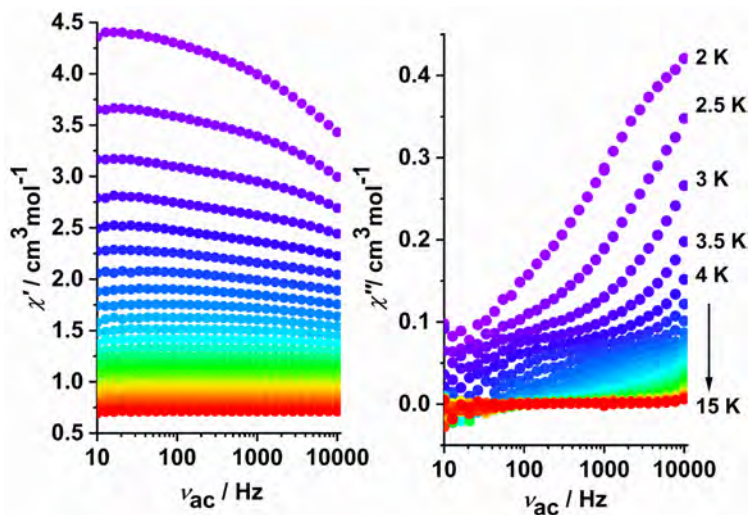
Fig. 2.22 Frequency dependence of the alternating current susceptibility for **TbI₂(bipy)₂.₅** at varying temperatures.

2.5 Conclusions

The self-assembly of linear {LnI₂} nodes with ditopic organic spacers (bipy) results in the formation of complex tiling patterns that mimic the structural motifs of quasi-periodic 2D materials, because their ability to host more than four ligands in the equatorial plane is significantly different from that of d-block metals. The semiregular Archimedean tessellations, snub square and elongated triangular tilings, were realized using paramagnetic Ln ions, Gd(III), Dy(III), Tb(III), Ho(III), and

Er(III) and a radical ligand (bipy$^{\bullet-}$) to form **LnI$_2$(bipy)$_{2.5}$**. The ligand bipy$^{\bullet-}$ improves magnetic properties. Among the **LnI$_2$(bipy)$_{2.5}$** compounds, **DyI$_2$(bipy)$_{2.5}$**, **TbI$_2$(bipy)$_{2.5}$**, **HoI$_2$(bipy)$_{2.5}$**, and **ErI$_2$(bipy)$_{2.5}$** show SMM behaviors.

In this chapter, we designed lanthanide-based Archimedean tessellations in bulk crystalline materials. This will promote the development of next-generation materials with complex and non-periodic tiling structures that exhibit novel photonic and magnetic phenomena owing to the unique physical properties of lanthanide ions.

Chapter 3. Archimedean tessellations in europium(II) coordination solids

All divalent lanthanide ions are reducing owing to their strong preference for the trivalent oxidation state. In this chapter, we report the construction of tessellations in magnetic metal–organic frameworks using different divalent lanthanides and ligands of different lengths.

As discussed in previous chapters, lanthanide chemistry is shaped by the nature of the 4f orbitals, which are close to the nucleus, as opposed to the spatially extended 3d orbitals. Lanthanide ions exhibit ample coordinated plasticity and possess large ionic radii that allow their incorporation into arrays based on irregular molecules. Our group previously reported the preparation of $CrCl_2(pyz)_2$ (pyz = pyrazine) by reacting $CrCl_2$ with pyrazine.[236] $CrCl_2(pyz)_2$ exhibits a ferrimagnetic order below 55 K and high electrical conductivity at room temperature, which are attributed to the redox activity of pyrazine ligands. Eu(II) is the most stable divalent lanthanide species with an aqueous reduction potential of $E_{Eu(III)/Eu(II)} = -0.35V$, which is similar to that of Cr(II) ($E_{Cr(III)/Cr(II)} = -0.41$ V). These comparable reduction potentials motivated us to explore potential tessellations in MOF materials. EuI_2 reacts with pyz in MeCN. Subsequently, different divalent lanthanide ions (Eu(II), Sm(II), and Yb(II)) and ligands (pyz, 4-4′-bipy, and 1,4-di(pyridin-4-yl)benzene (DPB)) were introduced to explore the effect of the size of the lanthanide ions and ligands on tessellation.

3.1 Synthesis procedures

3.1.1 Preparation of EuI$_2$(pyz)$_{2.5}$

EuI$_2$ (101.3 mg, 250 µmol) and pyz (500 mg, 6.25 mmol) were dissolved in 4 mL of MeCN separately. The two solutions were then mixed by stirring for 1 h at room temperature. A reddish crystalline powder was formed. The solid material was isolated using suction filtration. Yield: 38.3 mg (25.3%). Anal. calcd. (found) for C$_{10}$H$_{10}$I$_2$N$_5$Eu (**EuI$_2$(pyz)$_{2.5}$**): C, 19.91 (19.80); H, 1.67 (1.65); N, 11.53 (11.55); I, 41.51 (41.91); Eu, 24.79 (25.08).

Reddish single crystals suitable for SCXRD were obtained via slow diffusion. EuI$_2$ powder (101.3 mg, 250 µmol) was placed in a standard test tube (160 mm × 16 mm, soda glass). An acetonitrile solution (8 mL) of pyz (800 mg, 10 mmol) was slowly layered on top of it, and the reaction mixture was left undisturbed in a refrigerator at –20 °C for 11 days to afford dark-reddish crystals.

3.1.2 Preparation of SmI$_2$(pyz)$_{2.5}$

The dark-green crystals of SmI$_2$(pyz)$_{2.5}$ were grown from SmI$_2$ using the same procedure used for **EuI$_2$(pyz)$_{2.5}$**.

3.1.3 Preparation of YbI$_2$(pyz)$_{2.5}$

The dark-green crystals of YbI$_2$(pyz)$_{2.5}$ were grown from YbI$_2$ using the same procedure used for **EuI$_2$(pyz)$_{2.5}$**.

3.1.4 Preparation of EuI$_2$(bipy)$_{2.5}$

EuI$_2$ (101.3 mg, 250 µmol) and bipy (195 mg, 1.25 mmol) were dissolved in 7 mL of MeCN separately. The two solutions were then mixed by stirring for 2 h at room temperature. A reddish crystalline powder was formed. The solid material was isolated using suction filtration. Yield: 134.6 mg (64.34%). Anal. calcd. (found) for

$C_{27}H_{23}I_2N_6Eu$ ($EuI_2(bipy)_{2.5}\cdot C_2H_3N$): C, 38.71 (38.44); H, 2.75 (2.65); N, 10.04 (9.92); I, 30.35 (30.14); Eu, 18.16 (18.04).

Single crystals suitable for SCXRD were obtained via slow diffusion. EuI_2 powder (10.1 mg, 25μmol) was placed in an NMR test tube (tube diam. 5 mm, size 7 in.). An acetonitrile solution (bipy (19.5 mg, 125 μmol) dissolved in 2 mL MeCN) was slowly layered on top of it, and the reaction mixture was left undisturbed in a refrigerator at –20 °C for 14 days.

3.1.5 Preparation of $EuI_2(DPB)_{2.5}$

Single crystals suitable for SCXRD were obtained via slow diffusion. EuI_2 powder (10.1 mg, 25μmol) was placed in a standard test tube (160 mm × 16 mm, soda glass). DPB (29 mg, 0.125 mmol) was dissolved in 12 mL of MeCN. The MeCN solution was then slowly layered on top of the EuI_2 powder. The reaction mixture was left undisturbed in a refrigerator at –20 °C for 2 days to afford reddish crystals.

3.1.6 Preparation of $SmI_2(bipy)_{2.5}$

Single crystals suitable for SCXRD were obtained via slow diffusion. SmI_2 powder (152 mg, 0.375 mmol) was placed in a test tube (160 mm × 16 mm, soda glass). The solid was carefully covered with 18 mL of MeCN using a pipette to avoid swirling the SmI_2 layer at the bottom of the test tube. An MeCN solution (3 mL, 293 mg, 1.88 mmol) was slowly layered on top of it, and the reaction mixture was left undisturbed in a refrigerator at –20 °C for 7 days to afford dark-green crystals.

3.1.7 Preparation of $BaI_2(bipy)_2$

Single crystals suitable for SCXRD were obtained as follows: BaI_2 (9.8 mg, 0.025 mmol) and bipy (19.5 mg) were dissolved in 1 mL of MeCN separately. The two solutions were then mixed, and MeCN was slowly evaporated for 24 h to afford large white crystals.

3.2 Archimedean tessellations and magnetic properties of EuI$_2$(pyz)$_{2.5}$

The self-assembly reaction of EuI$_2$ and pyz at –20 °C yielded dark-orange single crystals of **EuI$_2$(pyz)$_{2.5}$** suitable for SCXRD. **EuI$_2$(pyz)$_{2.5}$** crystallized in the triclinic space group $P\overline{1}$ with the formula C$_{10}$H$_{10}$EuI$_2$N$_5$, forming a {EuN$_5$} moiety, and the two Eu ions share one pyz ligand. The {EuN$_5$} moiety skews slightly from planarity with a maximum distortion of ~3.7% from ideality for I1–Eu1–N4 and is comparable to a D_{5h} coordination environment. The N–Eu–N angles were in the range 64.81°–91.39°, distorting from the ideal angle of 72° (**Fig. 3.1b**). The bond lengths of Eu–I were 3.186-3.189 Å, which are slightly shorter than those in Eu(II)I$_2$(thf)$_5$ and Eu(II)I$_2$(CH$_3$CN)$_5$ (3.22–3.24 Å),[218, 237] confirming the presence of Eu(II) in the structure. The I–Eu–I angle was 174.28°, which is marginally different from the linear 180°. Furthermore, **EuI$_2$(pyz)$_{2.5}$** formed a layered structure with each layer comprising an elongated triangular tessellation (**Fig. 3.1a**). Within the 2D plane, Eu(II) and pyz form both triangular and rhombus tiles. The triangles and rhombi are nearly equilateral geometries and the Eu–Eu distances were 8.19, 8.23, and 8.27 Å for the triangles and 8.19 and 8.22 Å for the rhombi. The 2D interplane layer distance was ~7.3 Å (the cavities of the adjacent layers) with an AB-type stacking (**Fig. 3.2**). As mentioned before, in an AA-type stacking, the top layer is directly stacked on the bottom layer. Furthermore, AB-stacking can be obtained by shifting the top layer of the AA-stacking.[219]
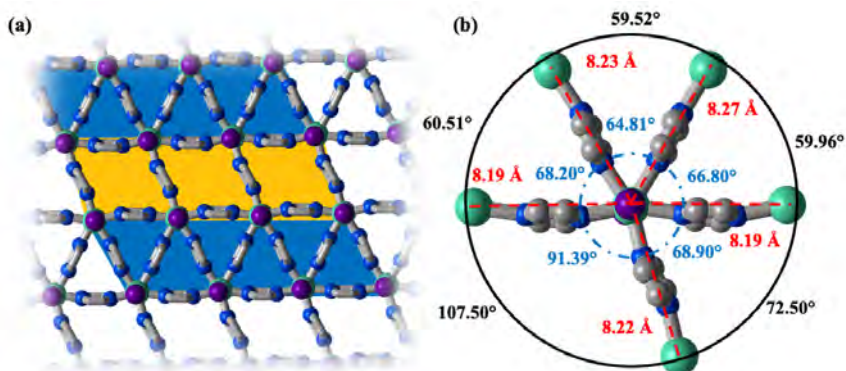
Fig. 3.1 Crystal structure of **EuI₂(pyz)₂.₅** as determined by SCXRD at $T = 120$ K. (a) Overlay of the fragments composing the coordination layer with the elongated triangular tessellation. (b) Five-vertex node of {EuI₂}^{II} and pyz linkers in **EuI₂(pyz)₂.₅**. ∠N–Eu–N and ∠Eu–Eu–Eu are shown in blue and black, respectively. The Eu-Eu distances are shown in red. Color code: Eu, light green; I, dark purple; N, blue; C, gray; hydrogen atoms and co-crystallized CH₃CN have been omitted for clarity.
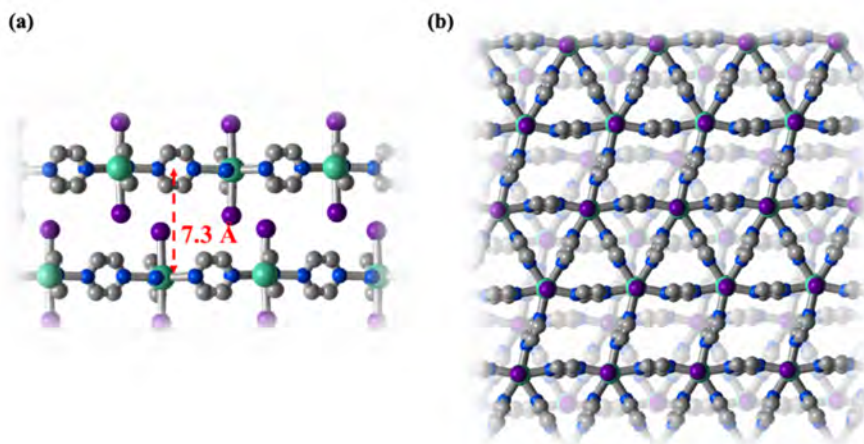
Fig. 3.2 Layer structures of the crystal structure of **EuI₂(pyz)₂.₅**. (a) Layer distances of **EuI₂(pyz)₂.₅** showing cavities of the adjacent layers. (b) Schematic of the layer-stacking.

Color code: Eu, light green; I, dark purple; N, blue; C, gray; hydrogen atoms and co-crystallized CH_3CN have been omitted for clarity.

PXRD was employed to confirm the purity of **EuI$_2$(pyz)$_{2.5}$**. As shown in **Fig. 3.3a**, the experimental result is in good agreement with the simulation result for the single-crystal structure, which confirms the purity and validity of the as-prepared sample. The X-ray absorption fine structure (XAFS) is the modulation of the X-ray absorption coefficient at energies near and above the X-ray absorption edge, which is a specific energy at which the absorption coefficient increases.[238, 239] The absorption edge is generated by the excitation of electrons in the inner layers of the atoms of the sample to the vacant or free state.[239] The absorption edge is determined by the elemental species of the absorbing atoms.[238] Therefore, XAFS is a powerful tool for studying the local environment of a compound, such as its atom oxidation state. Depending on the different inner-layer electron excitations, the absorption edges are named K-edge (1s electron excitation), L_1-edge (2s electron excitation), L_2-edge ($2p_{1/2}$ electron excitation), and L_3-edge ($2p_{3/2}$ electron excitation).[239] The XAFS spectra of the Eu L-edge corroborated the crystallographic information, as shown in **Fig. 3.3b-d**. All L-edge spectra of **EuI$_2$(pyz)$_{2.5}$** overlap well with that of the Eu(II) reference compound EuI$_2$ but not with that of the Eu(III) compound EuCl$_3$, which further confirms that Eu(II) and not Eu(III) is in the structure.
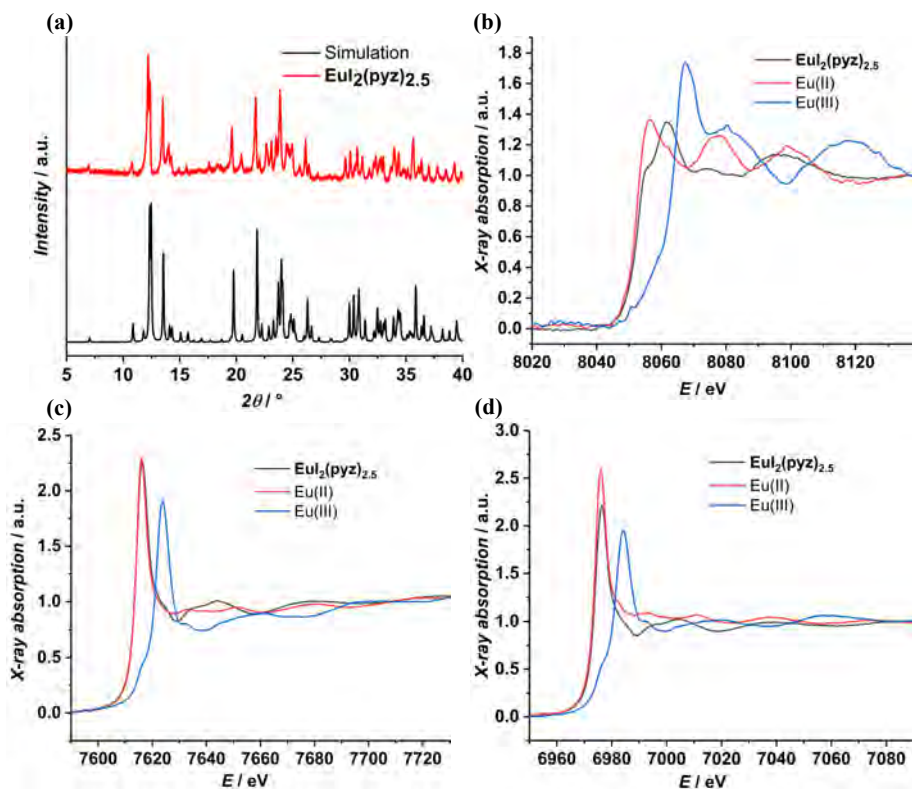
Fig. 3.3 (a) PXRD pattern of **EuI₂(pyz)₂.₅**. X-ray absorption fine structure (XAFS) at Eu L-edges of **EuI₂(pyz)₂.₅**: (b) L_1-edge, (c) L_2-edge, and (d) L_3-edge. The Eu(II) and Eu(III) reference compounds are EuI₂ and EuCl₃, respectively.

χT of **EuI₂(pyz)₂.₅** at room temperature was 7.8 cm³ K mol⁻¹, which is comparable to the anticipated value of Eu(II) ion ($g = 2$, $S = 7/2$, 7.88 cm³ K mol⁻¹) (**Fig. 3.4a**). The χT product decrease sharply at 13 K, indicating that the Eu-Eu superexchange interactions are weak and that only the ground state is populated at low temperatures. Moreover, the field dependence of the magnetization (M vs. H) revealed that the saturation of M at low temperatures

is 7.0 μ_B in a 9 T applied magnetic field (**Fig. 3.4b**). The magnetization curves at different temperatures overlapped, indicating the magnetic isotropy of **EuI$_2$(pyz)$_{2.5}$**.
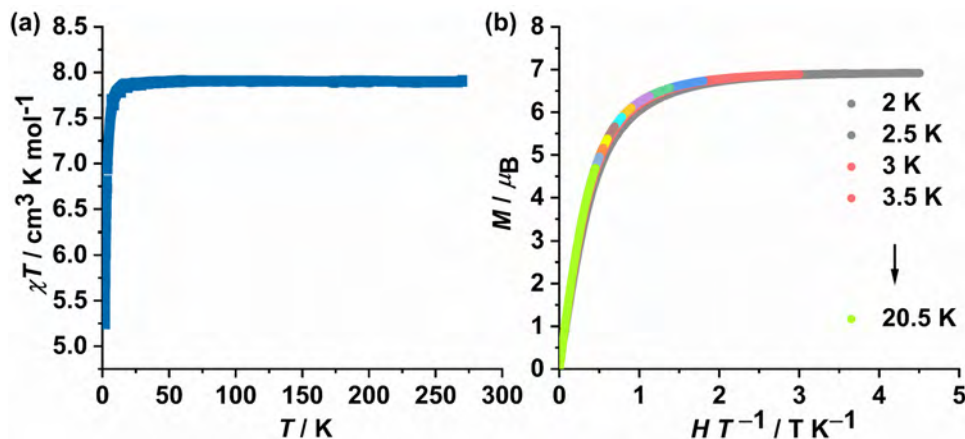
Fig. 3.4 (a) Temperature dependence of the χT product for **EuI$_2$(pyz)$_{2.5}$**. (b) Field dependence of the reduced magnetization, M vs. H/T, for **EuI$_2$(pyz)$_{2.5}$**.

3.3 Tunability of EuI$_2$(pyz)$_{2.5}$

3.3.1 Influence of metal ion

Atomic radii play an important role in coordination chemistry and might affect tessellation. To explore the influence of the metal ions on the structure, EuI$_2$ was replaced by SmI$_2$ and YbI$_2$.

The self-assembly reaction of SmI$_2$ and pyz at –20 °C yielded dark-green single crystals (**SmI$_2$(pyz)$_{2.5}$**) suitable for SCXRD. The **SmI$_2$(pyz)$_{2.5}$** crystallized in the triclinic space group $P\overline{1}$ with the formula C$_{10}$H$_{10}$SmI$_2$N$_5$, forming a {SmN$_5$} moiety with two Sm ions sharing one pyz ligand. The skews of the {SmN$_5$} moiety are comparable to a D_{5h} coordination environment, and the N–Sm–N angles were in the range 64.91°–90.96°, distorting from the ideal angle of 72° (**Fig. 3.5b**). The bond lengths of Sm–I were in the range 3.190–3.194 Å, which are slightly shorter than

68

those in $Sm(II)I_2(thf)_5$ and $Eu(II)I_2(CH_3CN)_5$ (3.22–3.24 Å)[218, 237] and comparable to those in **EuI_2(pyz)_{2.5}**, thus confirming the existence of Sm(II) in the structure. The I–Sm–I angle was 174.14°, which is nearly linear. In addition, **SmI_2(pyz)_{2.5}** formed a layered structure, and each layer has an elongated triangular tessellation Within the 2D plane, the Sm(II) and pyz forms both triangular and rhombus tiles (**Fig. 3.5a**).

YbI_2(pyz)_{2.5} has similar tessellation and geometry to those of **EuI_2(pyz)_{2.5}** and **SmI_2(pyz)_{2.5}**. The I–Yb bond length confirmed the presence of Yb(II) in **YbI_2(pyz)_{2.5}**. (**Fig. 3.6**).
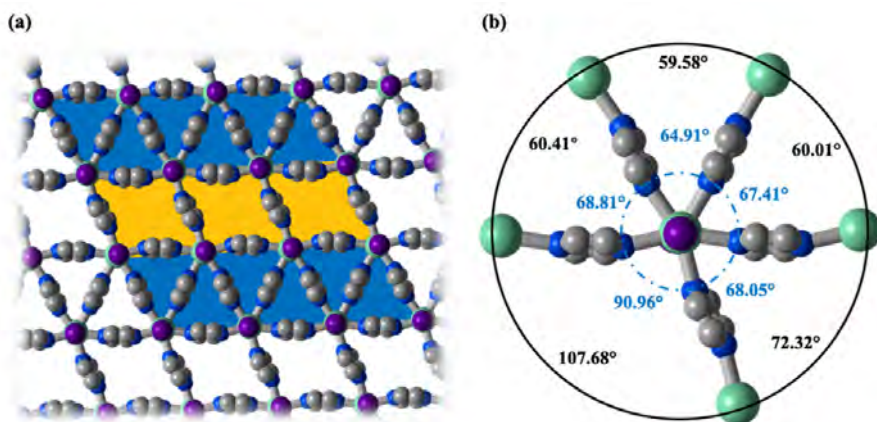
**Fig. 3.5** Representations of the crystal structure of **SmI_2(pyz)_{2.5}** as determined by SCXRD at $T = 120$ K. (a) Overlay of the fragments composing the coordination layer with the elongated triangular tessellation. (b) Five-vertex node of {SmI_2} and pyz linkers in **SmI_2(pyz)_{2.5}**. ∠N–Sm–N and ∠Sm–Sm–Sm are shown in blue and black, respectively. Color code: Sm light green; I dark purple; N blue; C gray; hydrogen atoms and co-crystallized CH_3CN have been omitted for clarity.
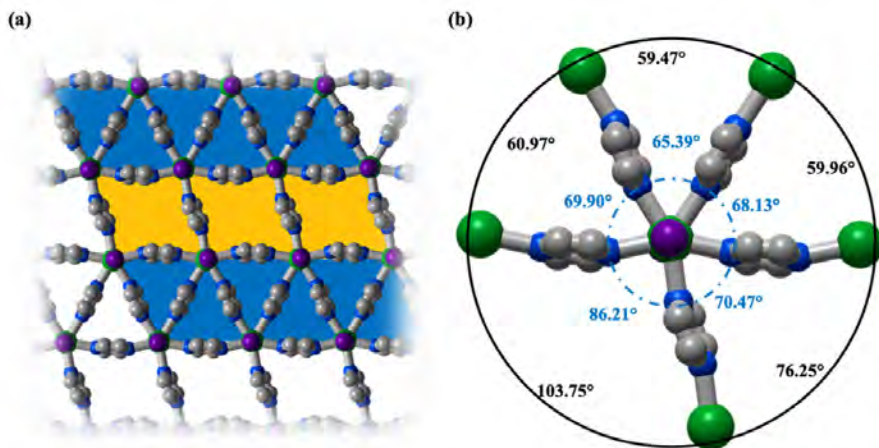
Fig. 3.6 Representations of the crystal structure of **YbI$_2$(pyz)$_{2.5}$** determined by SCXRD at T = 120 K. (a) Overlay of the fragments composing the coordination layer with the elongated triangular tessellation. (b) The five-vertex node of {YbI$_2$} and pyz linkers in **YbI$_2$(pyz)$_{2.5}$**. The ∠N–Yb–N and ∠Yb–Yb–Yb are shown in blue and black, respectively. Color code: Yb green; I dark purple; N blue; C gray; hydrogen atoms and co-crystallized CH$_3$CN have been omitted for clarity.

3.3.2 Influence of ligand

Crystallization of EuI$_2$ with bipy in MeCN yielded orange crystals of **EuI$_2$(bipy)$_{2.5}$**, and its SCXRD showed that the structure has a pentagonal bipyramidal coordination similar to that of **EuI$_2$(pyz)$_{2.5}$**. **EuI$_2$(bipy)$_{2.5}$** crystallized in the $P\overline{1}$ space group and consists of layers of an elongated triangular tiling in which nearly five-fold {EuI$_2$} nodes are linked by bipy linkers to form rhombi and triangles (**Fig. 3.7a**). Locally, the coordination geometry around Eu resembles that of a defective D_{5h} coordination with N–Eu–N angles in the range 68.63°–80.3°, where the ideal angle is 72° (**Fig. 3.7b**). In addition, the Eu–Eu–Eu angles were as expected for the elongated triangular tessellation. Moreover, as discussed before, electron transfer from Eu to the pyz ligands does not occur in **EuI$_2$(pyz)$_{2.5}$** despite the properties of Eu(II) ($E_{Eu(III)/Eu(II)}$ = -0.35 V). The reduction potential of bipy is similar to that of pyz,[240]

therefore, Eu(II) ion must be present in **EuI₂(bipy)₂.₅**. The SCXRD data indicates that the bond length of Eu–I is 3.21 Å, which is slightly shorter than those in Eu(II)I₂(thf)₅ and Eu(II)I₂(CH₃CN)₅ (3.22–3.24 Å),[218, 237] and the I–Eu–I angle is 177.1°, which is approximately linear, confirming that Eu(II) is in the structure.

Fig. 3.7 Representation of the crystal structure of **EuI₂(bipy)₂.₅** as determined by SCXRD at $T = 120$ K. (a) Overlay of the fragments composing the coordination layer with the elongated triangular tessellation. (b) Five-vertex node of {EuI₂} and bipy linkers in **EuI₂(bipy)₂.₅**. ∠N–Eu–N and ∠Eu–Eu–Eu are shown in blue and black, respectively. Color code: Eu, light green; I, dark purple; N, blue; C, gray; hydrogen atoms and co-crystallized CH₃CN have been omitted for clarity.

Fig. 3.8a shows the experimental PXRD, which are in good agreement with the simulation crystallographic result. XAFS at the Eu L-edge corroborated the crystallographic information shown in **Fig. 3.8b-d**. All the L-edge spectra of **EuI₂(bipy)₂.₅** are superimposable with the Eu(II) reference compound but also suggest the presence of small amounts of Eu(III), which is ascribed to the partial oxidation of the compound during the measurement or contamination of the compound during the preparation of the XAFS sample. The Eu(II) and Eu(III) reference compounds are EuI₂ and EuCl₃, respectively.
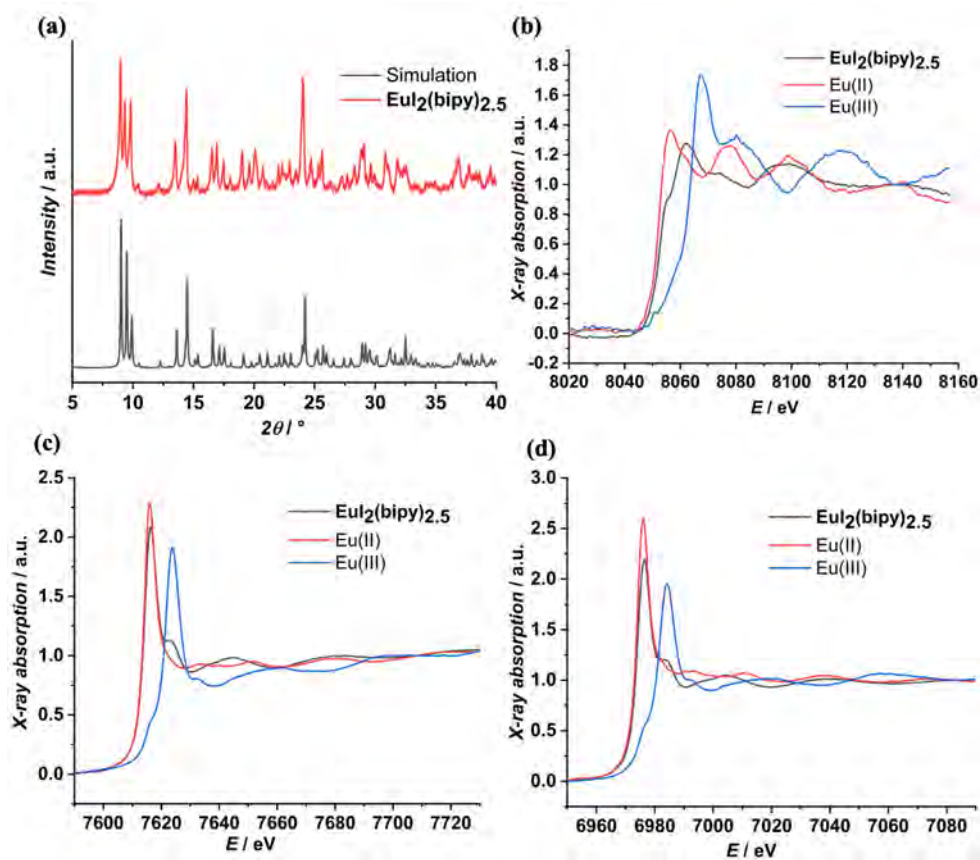
Fig. 3.8 (a) PXRD pattern of **EuI$_2$(bipy)$_{2.5}$**. XAFS at Eu *L*-edges of **EuI$_2$(bipy)$_{2.5}$**: (b) *L$_1$*-edge, (c) *L$_2$*-edge, and (d) *L$_3$*-edge. The Eu(II) and Eu(III) reference compounds are EuI$_2$ and EuCl$_3$, respectively.

The crystallization of EuI$_2$ with DPB in MeCN yielded orange crystals. The compound crystallized in the tetragonal space group I4$_1$/amd with the formula EuI$_2$(DPB)$_{2.5}$·CH$_3$CN. Each Eu ion coordinates with five DPB ligands, forming a pentagonal bipyramidal coordination environment. However, in each **EuI$_2$(DPB)$_{2.5}$** moiety, one of the five Eu atoms adjacent to the central Eu atom is rotated by 90° and coordinated with DPB ligands forming a 3D structure (**Fig. 3.9**), which is different from the previous structures observed in this study and has never been reported thus far. Furthermore, the Eu–I bond length is 3.26 Å, which is slightly

72

longer than those in $Eu(II)I_2(thf)_5$ and $Eu(II)I_2(CH_3CN)_5$ (3.22–3.24 Å),[218, 237] indicating that Eu(II) is in the structure.
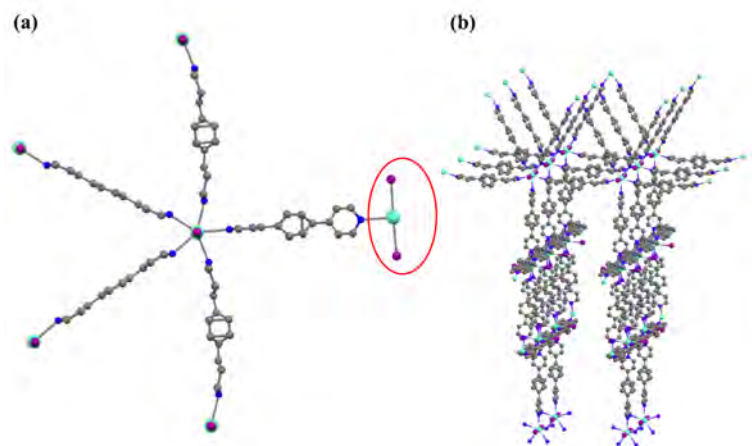
Fig. 3.9 (a) Five-vertex node of {EuI$_2$} and DPB linkers in **EuI$_2$(DPB)$_{2.5}$**. The atoms in the red circle are the Eu and two I ions that are rotated by 90°. (b) Schematic of the 3D structure of **EuI$_2$(DPB)$_{2.5}$**. Color code: Eu, light green; I, dark purple; N, blue; C, gray; hydrogen atoms and co-crystallized CH_3CN have been omitted for clarity.

As shown in this thesis, all the elongated triangular tessellations in the compounds with bipy as the ligand are similar to those of the previously reported **YbI$_2$(bipy)$_{2.5}$**. Nevertheless, the tilting angle (α) (**Fig. 3.10**) of **YbI$_2$(bipy)$_{2.5}$** (90°) is different from that of **EuI$_2$(bipy)$_{2.5}$** (111.97°). Hence, **EuI$_2$(bipy)$_{2.5}$** could have the defective six-fold nodes ($\alpha = 120°$). This may be attributed to the ionic radius of Eu^{2+} (1.39 Å), which is larger than that of Yb^{2+} (1.28 Å) owing to the Ln contraction. To explore the influence of the atomic radii on the tilting angle, SmI_2 (ionic radii, 1.41 Å) and BaI_2 (ionic radii, 1.56 Å) were reacted with bipy in MeCN separately.
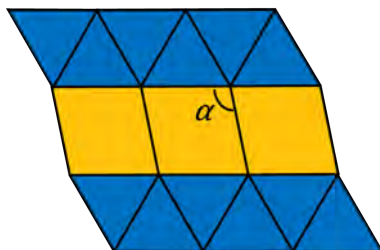
Fig. 3.10 An example of the semiregular elongated triangular tiling.

Dark-green crystals formed when SmI_2 is reacted with bipy in MeCN crystallized in the $P\overline{1}$ space group with elongated triangular tiling, which is identical to that of **EuI$_2$(bipy)$_{2.5}$** (**Fig. 3.11**). However, the tiling angle was 105.2°, which is not expected, as it should be larger than 111.97° as observed for **EuI$_2$(bipy)$_{2.5}$**. The Sm–I bond length was 3.23 Å, which is similar to those in $Eu(II)I_2(thf)_5$ and $Eu(II)I_2(CH_3CN)_5$ (3.22–3.24 Å),[218, 237] indicating that Sm(II) is in the structure.

However, when BaI_2 reacts with bipy in MeCN, white crystals of **BaI$_2$(bipy)$_2$** crystallize in the $P2_1/c$ space group. The crystal structure was completely different from that of previously observed structures in this study. The two Ba ions are bridged by iodine ions, forming a step-like layer (**Fig. 3.12**, **Fig. 3.13**).
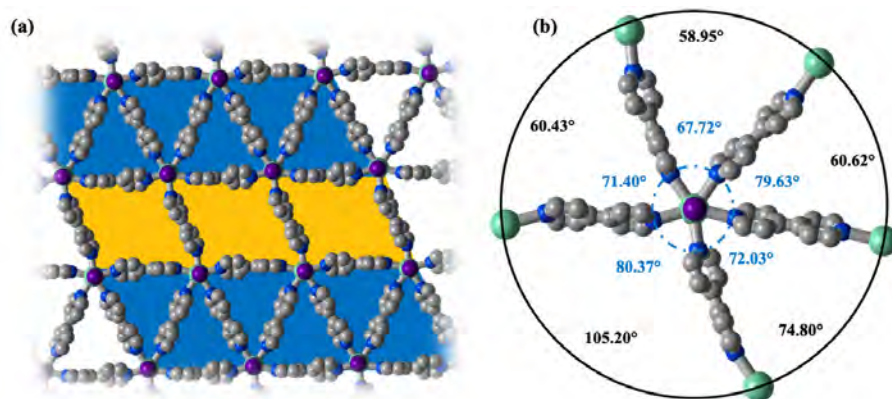
Fig. 3.11 Representation of the crystal structure of **SmI$_2$(bipy)$_{2.5}$** as determined by SCXRD at T = 120 K. (a) Overlay of the fragments composing the coordination layer with the

elongated triangular tessellation. (b) Five-vertex node of {SmI$_2$} and bipy linkers in **SmI$_2$(bipy)$_{2.5}$**. ∠N–Sm–N and ∠Sm–Sm–Sm are shown in blue and black, respectively. Color code: Sm, light green; I, dark purple; N, blue; C, gray; hydrogen atoms and co-crystallized CH$_3$CN have been omitted for clarity.
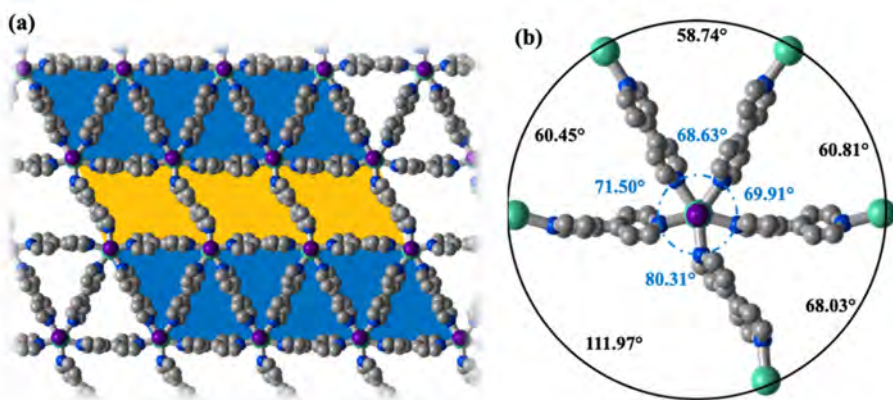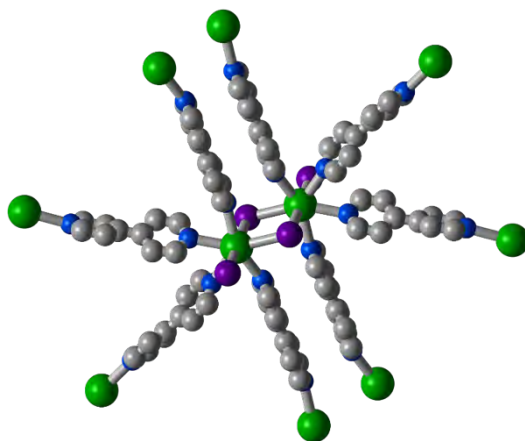

Fig. 3. 12 Structure of **BaI$_2$(bipy)$_2$** determined by SCXRD at T = 120 K. Fragment of the structure showing the connectivity of the Ba ions. Color code: Ba, light green; I, dark purple; N, blue; C. gray; hydrogen atoms and co-crystallized CH$_3$CN have been omitted for clarity.
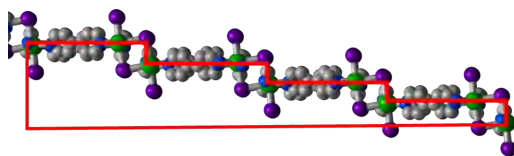
Fig. 3. 13 Step-like layer of **BaI$_2$(bipy)$_2$** determined by SCXRD at T = 120 K. Color code: Ba, light green; I, dark purple; N, blue; C, gray; hydrogen atoms and co-crystallized CH$_3$CN have been omitted for clarity.

3.4 Conclusions

In this chapter, the tunability of the coordination network of **EuI$_2$(pyz)$_{2.5}$**, **SmI$_2$(pyz)$_{2.5}$**, **YbI$_2$(pyz)$_{2.5}$**, **EuI$_2$(bipy)$_{2.5}$**, **EuI$_2$(DPB)$_{2.5}$**, **SmI$_2$(bipy)$_{2.5}$**, **BaI$_2$(bipy)$_2$** were explored. **EuI$_2$(pyz)$_{2.5}$** has the elongated triangular tiling of defective six-fold nodes, which paves the way for establishing the real six-fold nodes. Despite the reduction potential between Eu(II) and pyz, the mixed valency of pyz and IVCT in the compound could not be confirmed. The use of Ln(II) ions larger and smaller (Sm(II) and Yb(II), respectively) than Eu(II) resulted in a similar elongated triangular tiling to that of **EuI$_2$(pyz)$_{2.5}$**. The use of ligands other than pyz resulted in different structures. **EuI$_2$(bipy)$_{2.5}$** displayed elongated triangular tiling, whereas **EuI$_2$(DPB)$_{2.5}$** exhibited a 3D structure that is completely different from previously reported structures. Hence, the ligand plays a significant role in structural construction. Furthermore, **SmI$_2$(bipy)$_{2.5}$** and **BaI$_2$(bipy)$_2$** were prepared in an attempt to construct a six-fold node system. Nevertheless, **SmI$_2$(bipy)$_{2.5}$** showed identical elongated triangular tessellation to that of **EuI$_2$(bipy)$_{2.5}$**, whereas **BaI$_2$(bipy)$_2$** exhibited a different structure from a six-fold node structure, which is likely owing to its difficult assembly.

Chapter 4. Outlook

The research presented in this thesis illustrates a chemical strategy to tailor Archimedean tessellation topologies in MOFs by exploiting Ln ions with high coordination numbers. The five-vertex tilings indicate the occurrence of metal–organic quasicrystalline phases in a bulk material. The findings of this study promote the development of next-generation materials with complex and aperiodic structures exhibiting novel magnetic phenomena originating from the unique physical properties of Ln ions.

In chapter 2, we discussed the preparation of bipy radical ligands and introduced them into the MOFs. Although these MOFs have interesting magnetic properties and Archimedean tessellations, their precarious structures limit their applications. Therefore, more stable MOFs with unique structures and different Ln ions and ligands should be synthesized and their properties must be investigated.

In chapter 3, we presented MOFs containing longer ligands than pyz and different Ln ions, which altered the structures of the MOFs. These phenomena must be further explored by combining different ligands and metal ions to construct various MOFs. Some examples of further studies that can be conducted following the findings of this study are the exfoliation of layered **$EuI_2(pyz)_2$** and post-synthetic reduction of **$EuI_2(pyz)_{2.5}$**.

Moreover, Archimedean tessellations can also be incorporated in organic materials such as covalent organic frameworks and actinide ions, and based on the findings of this study, real six-fold node MOFs can be introduced in bulk materials.

Chapter 5. Other experiments

In addition to the experiments presented in the previous chapters which involve magnetic Archimedean tessellations in MOFs, the preparation of various MOFs—MOFs with pyrazine radical, an Eu(II)-based MOF with 2-fluoropyrazine, a 1D MOF, and a 2D bimetallic layered MOF—were attempted with unsuccessful results.

5.1 Preparation of a metal-organic framework with pyrazine radical

In chapter 2, we discussed the introduction of bipy radicals into Ln-based MOFs to achieve unique magnetic properties and tessellations, and in chapter 3, we described several magnetic Archimedean tessellations in MOFs with pyz ligands. During the course of this study, we attempted to introduce the pyz radical into Ln-based MOFs.

As previously mentioned, metallic sodium can reduce bipy to generate bipy radicals. The same method was used to introduce pyz radicals into an Ln-based MOF. Metallic sodium was reacted with 2.5 molar equivalents of pyz in MeCN to afford a dark-brown solution, from which a white precipitate was formed after approximately 10 s. This is attributed to the high reactivity and short survival time of the pyz radical. Photographs of the various stages of the reaction process are shown in **Fig. 5.1**. Subsequently, different molar ratios of sodium and pyz, were employed, all of which exhibited similar results. When THF was used as the solvent, the reaction between sodium and pyz solution did not occur. Based on the solubility and reactivity of pyz, MeCN was determined to be the optimum solvent.
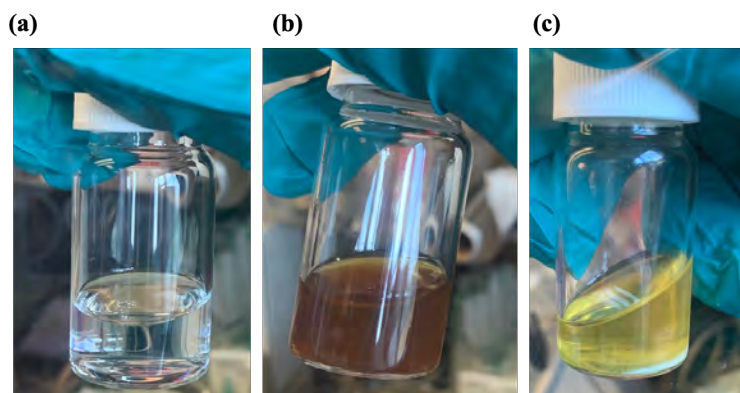
Fig. 5.1 Digital photographs of pyz radical preparation. (a) Colorless solution of pyz in MeCN solution, (b) dark-brown solution of sodium and pyz, and (c) white precipitate formed from the dark-brown solution after 10 s.

Considering the short lifetime of the pyz radical, the synthesis procedure of Ln-MOFs with pyz radicals was modified. Powdered DyI_3 and pyz were dissolved in MeCN, and metallic sodium was added to the mixture, following which it was placed in a refrigerator. However, the single crystals obtained were unsuitable for SCXRD analysis. This is ascribed to the rapid formation and short lifetime of the pyz radical, which makes it extremely difficult to grow a single crystal in such a short time. However, when powdered DyI_3 and pyz were dissolved in MeCN and added to metallic sodium while stirring, a brown precipitate was formed. The brown precipitate of **DyI_3-pyz** was then isolated by suction filtration and washed with MeCN. Digital photographs of **DyI_3-pyz** and isolated **DyI_3-pyz** are shown in **Fig. 5.2**. Moreover, **DyI_3-pyz** burns and produces a fume when exposed to air, which indicates its high reactivity.

The PXRD pattern of isolated **DyI_3-pyz** is shown in **Fig. 5.3**. **DyI_3-pyz** exhibited poor crystallinity, which is attributed to the rapid formation and disordered arrangement of **DyI_3-pyz**. Therefore, the structure of **DyI_3-pyz** and its purity could not be determined.
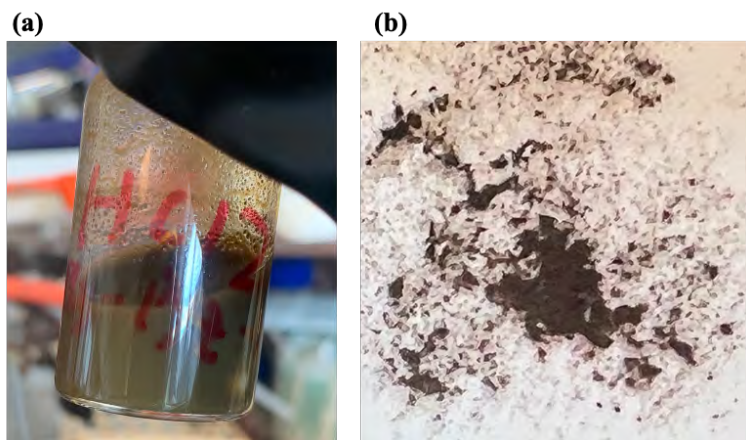
Fig. 5.2 Digital photographs of **DyI₃-pyz**. (a) **DyI₃-pyz** in MeCN solution and (b) isolated **DyI₃-pyz** after washing with MeCN.
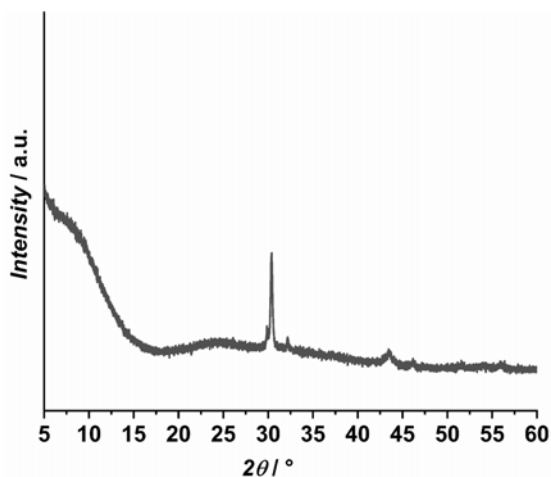
Fig. 5.3 PXRD pattern of **DyI₃-pyz**.

5.2 Preparation of an Eu(II) based metal-organic framework with 2-fluoropyrazine

During the preparation of Eu(II)-based MOFs discussed in chapter 3, an attempt was made to substitute pyz with 2-fluoropyrazine (Fpyz) using the same synthesis

method. Different molar ratios of EuI_2 to Fpyz, were employed at room temperature and at -20 °C; however, no crystals were obtained, which may be ascribed to the steric hindrance of Fpyz, which prevents its coordination with EuI_2.

5.3 Preparation of a 1D metal-organic framework

Numerous studies on 2D MOFs have been reported in the literature. However, the synthesis of magnetic and conductive 1D MOFs has remained largely unexplored. 1D MOFs have low densities, structural and chemical versatility, mild synthesis conditions, and easily exposed active sites. Based on the study by Jiang et al.,[241] a 1D Cr(II)-based MOF (named **Cr-BTA**) has been synthesized in this study using 1,2,4,5-benzentatramine as the ligand and tetramethoxypropane to extend the π-conjugation. The synthesis procedure is shown in **Fig. 5.4**.
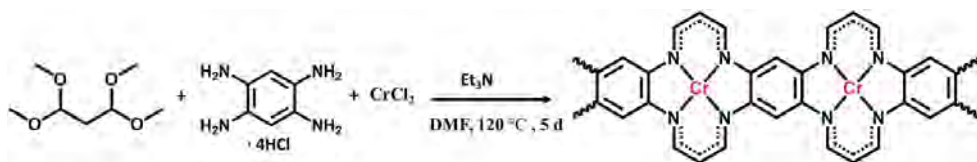
Fig. 5.4 Synthesis procedure of **Cr-BTA**. The reaction was conducted in a sealed ampule, which was heated in a furnace.

The black powder of **Cr-BTA** obtained after the reaction was washed with DMF and THF. Its PXRD pattern (**Fig. 5.5**) indicates poor crystallinity, and the elemental analysis results are in good agreement with the theoretical values. Anal. calcd. (found) for $C_{12}H_8N_4Cr$ (**Cr-BTA**): C, 55.38 (53.72); H, 3.08 (3.28); N, 21.52 (20.47); Cr, 20 (19.23). Even though the reaction time and temperature were changed, the crystallinity of **Cr-BTA** was not improved.
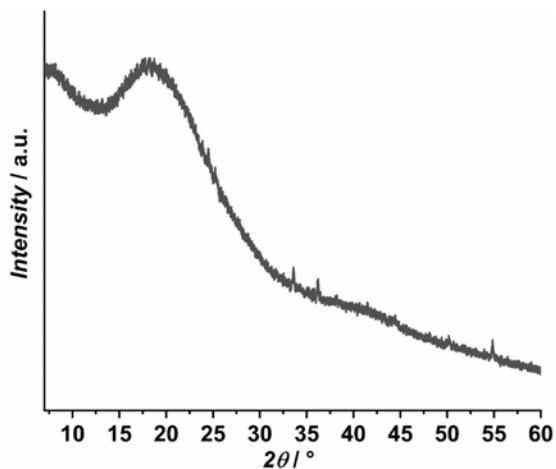
Fig. 5.5 The PXRD pattern of **Cr-BTA**.

The morphology of **Cr-BTA** was characterized by scanning electron microscopy (SEM) and transmission electron microscopy (TEM), as shown in **Fig. 5.6**. **Cr-BTA** has a spherical morphology with a diameter of approximately 3 μm and a smooth particle surface. We expect that XAFS could help in the determination of the local environment of the Cr atoms.

(a) **(b)**
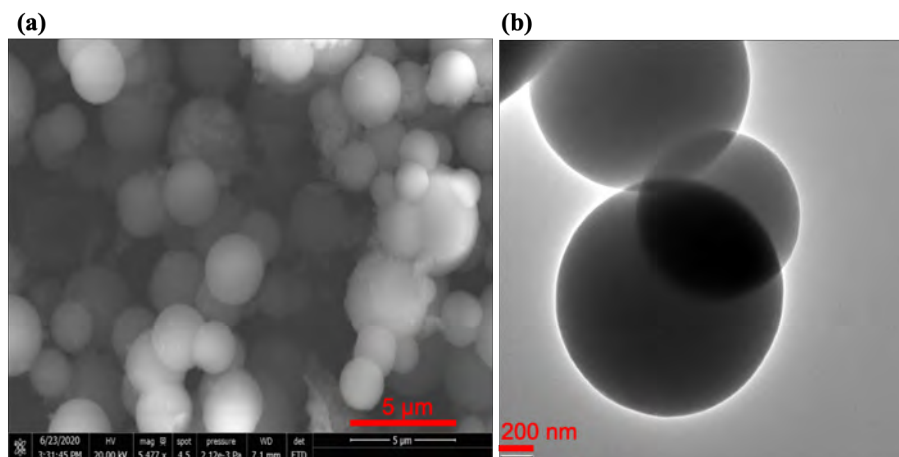
Fig. 5.6 (a) The SEM image of **Cr-BTA**, scale bar 5 μm. (b) The TEM image of **Cr-BTA**, scale bar 200 nm.

5.4 Preparation of 2D bimetallic layered metal-organic frameworks

Conventional MOFs have some drawbacks such as inherent low conductivity and blockage of metal centers by organic ligands.[242] A layered 2D-conjugated MOF will solve these problems. This MOF has in-plane π-delocalization along 2D directions and weak out-of-plane π-π stacking, which results in a higher density of exposed metal centers.[243, 244] 2D-conjugated MOFs have been widely used in electrocatalysis such as the hydrogen evolution reaction[244] and carbon dioxide reduction reaction.[245] However, the application of 2D-conjugated MOFs in heterogeneous catalysis such as biomass transfer is limited. Furthermore, owing to the tunability of MOFs, 2D-conjugated MOFs with bimetallic centers with improved catalytic properties and applicability in numerous reactions can be synthesized. Inspired by Haixia Zhang et al. work published in 2020,[242] three 2D-conjugated bimetallic MOFs (**M-PcCu**, M= Ni, Zn, and Cu) are synthesized. The synthetic procedure is shown in **Fig. 5.7**.
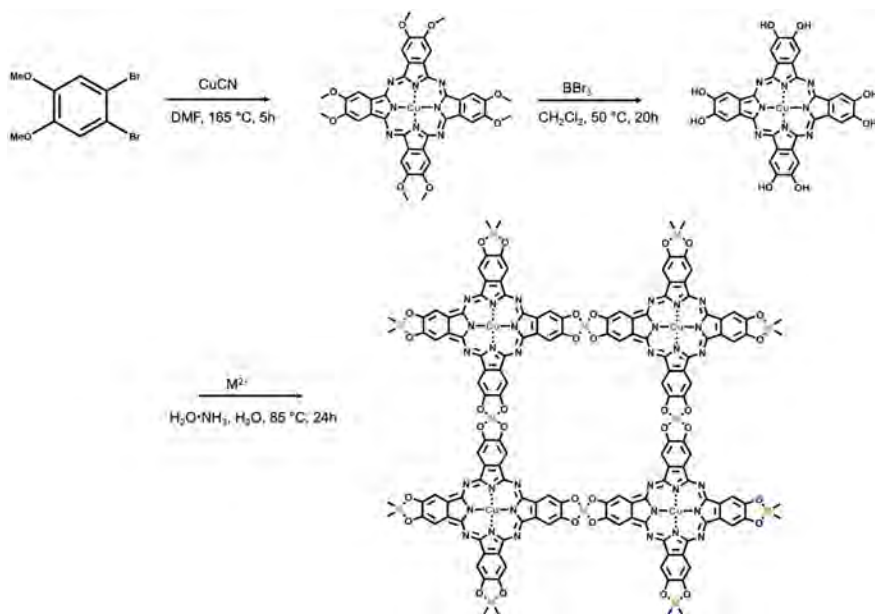
Fig. 5.7 The synthesis procedure of **M-PcCu**. (M^{2+} = Ni^{2+}, Zn^{2+}, Cu^{2+})

The PXRD patterns of **Zn-PcCu**, **Ni-PcCu**, and **Cu-PcCu** shown in **Fig. 5.8** are consistent with the previously reported results,[242, 244] However, the crystallinity of the three compounds must be improved.

Further experiments such as the purification and characterization of the intermediate and final products must be conducted and the applications of the prepared MOFs must be explored.
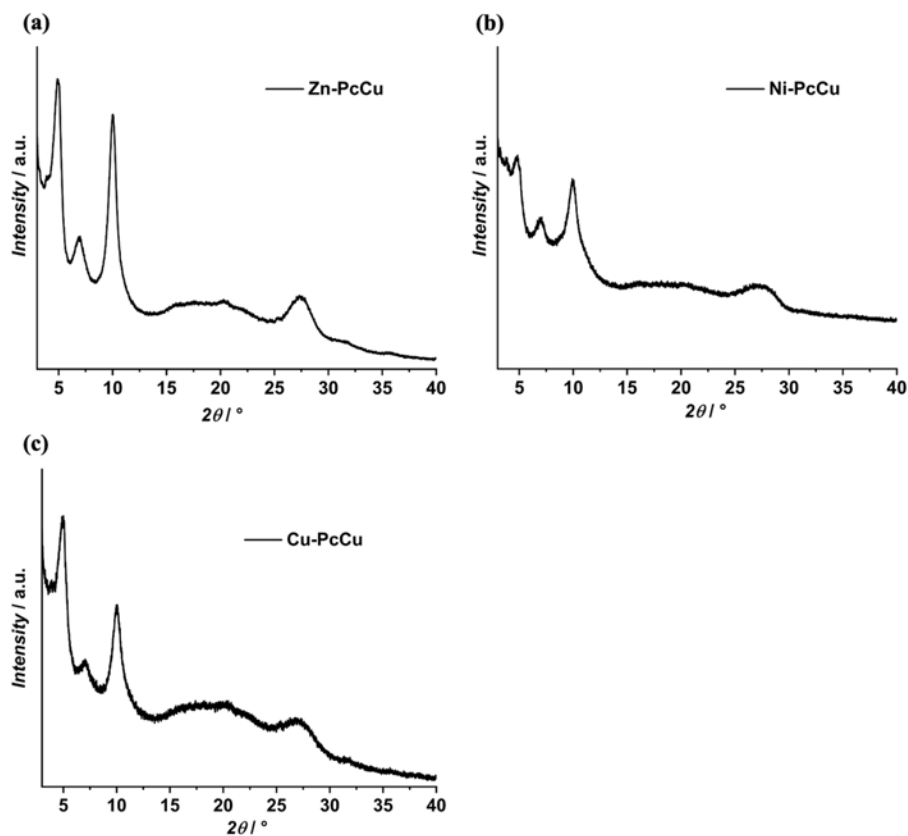
Fig. 5.8 PXRD patterns of (a) **Zn-PcCu**, (b) **Ni-PcCu**, and (c) **Cu-PcCu**.

Chapter 6. Reference

1.   James, S. L., Metal-organic frameworks. *Chemical Society Reviews* **2003,** *32* (5), 276-288.

2.   Rowsell, J. L.; Yaghi, O. M., Metal–organic frameworks: a new class of porous materials. *Microporous and mesoporous materials* **2004,** *73* (1-2), 3-14.

3.   Furukawa, H.; Cordova, K. E.; O'Keeffe, M.; Yaghi, O. M., The chemistry and applications of metal-organic frameworks. *Science* **2013,** *341* (6149), 1230444.

4.   Zhu, Q. L.; Xu, Q., Metal–organic framework composites. *Chemical Society Reviews* **2014,** *43* (16), 5468-5512.

5.   Gangu, K. K.; Maddila, S.; Mukkamala, S. B.; Jonnalagadda, S. B., A review on contemporary metal–organic framework materials. *Inorganica Chimica Acta* **2016,** *446*, 61-74.

6.   Murray, L. J.; Dincă, M.; Long, J. R., Hydrogen storage in metal–organic frameworks. *Chemical Society Reviews* **2009,** *38* (5), 1294-1314.

7.   Suh, M. P.; Park, H. J.; Prasad, T. K.; Lim, D. W., Hydrogen storage in metal–organic frameworks. *Chemical reviews* **2012,** *112* (2), 782-835.

8.   Sumida, K.; Rogow, D. L.; Mason, J. A.; McDonald, T. M.; Bloch, E. D.; Herm, Z. R.; Bae, T. H.; Long, J. R., Carbon dioxide capture in metal–organic frameworks. *Chemical reviews* **2012,** *112* (2), 724-781.

9.   Mason, J. A.; Veenstra, M.; Long, J. R., Evaluating metal–organic frameworks for natural gas storage. *Chemical Science* **2014,** *5* (1), 32-51.

10.   Rowsell, J. L.; Spencer, E. C.; Eckert, J.; Howard, J. A.; Yaghi, O. M., Gas adsorption sites in a large-pore metal-organic framework. *Science* **2005,** *309* (5739), 1350-1354.

11.   Li, J. R.; Kuppler, R. J.; Zhou, H. C., Selective gas adsorption and separation in metal–organic frameworks. *Chemical Society Reviews* **2009,** *38* (5), 1477-1504.

12.   Li, J. R.; Sculley, J.; Zhou, H. C., Metal–organic frameworks for separations. *Chemical reviews* **2012,** *112* (2), 869-932.

13.   Herm, Z. R.; Bloch, E. D.; Long, J. R., Hydrocarbon separations in metal–organic frameworks. *Chemistry of Materials* **2014,** *26* (1), 323-338.

14.   Adil, K.; Belmabkhout, Y.; Pillai, R. S.; Cadiau, A.; Bhatt, P. M.; Assen, A. H.; Maurin, G.; Eddaoudi, M., Gas/vapour separation using ultra-microporous metal–organic frameworks: insights into the structure/separation relationship. *Chemical Society Reviews* **2017,** *46* (11), 3402-3430.

15.   Qiu, S.; Xue, M.; Zhu, G., Metal–organic framework membranes: from synthesis to separation application. *Chemical Society Reviews* **2014,** *43* (16), 6116-6140.

16.   Ma, L.; Abney, C.; Lin, W., Enantioselective catalysis with homochiral metal–organic frameworks. *Chemical Society Reviews* **2009,** *38* (5), 1248-1256.

17.   Lee, J.; Farha, O. K.; Roberts, J.; Scheidt, K. A.; Nguyen, S. T.; Hupp, J. T., Metal–organic framework materials as catalysts. *Chemical Society Reviews* **2009,** *38* (5), 1450-1459.

18.   Corma, A.; Garcia, H.; Llabrés i Xamena, F., Engineering metal organic frameworks for heterogeneous catalysis. *Chemical reviews* **2010,** *110* (8), 4606-4655.

19.   Yang, D.; Gates, B. C., Catalysis by metal–organic frameworks: perspective and suggestions for future research. *Acs Catalysis* **2019,** *9* (3), 1779-1798.

20.   Mahmood, A.; Guo, W.; Tabassum, H.; Zou, R., Meta–organic framework-based nanomaterials for electrocatalysis. *Advanced Energy Materials* **2016,** *6* (17), 1600423.

21.   Sun, L.; Campbell, M. G.; Dincă, M., Electrically conductive porous metal–organic frameworks. *Angewandte Chemie International Edition* **2016,** *55* (11), 3566-3579.

22.   Liu, B.; Shioyama, H.; Akita, T.; Xu, Q., Metal–organic framework as a template for porous carbon synthesis. *Journal of the American Chemical Society* **2008,** *130* (16), 5390-5391.

23.   Chakraborty, G.; Park, I.-H.; Medishetty, R.; Vittal, J. J., Two-dimensional metal–organic framework materials: synthesis, structures, properties and applications. *Chemical Reviews* **2021,** *121* (7), 3751-3891.

24.   Alvaro, M.; Carbonell, E.; Ferrer, B.; Llabrés i Xamena, F. X.; Garcia, H., Semiconductor behavior of a metal–organic framework (MOF). *Chemistry – A European Journal* **2007,** *13* (18), 5106-5112.

25.   Gascon, J.; Kapteijn, F., Metal–organic framework membranes — high potential, bright future? *Angewandte Chemie International Edition* **2010,** *49* (9), 1530-1532.

26.   Carrasco, S., Metal–Organic Frameworks for the Development of Biosensors: A Current Overview. *Biosensors* **2018,** *8* (4), 92.

27.   Aakeröy, C. B.; Champness, N. R.; Janiak, C., Recent advances in crystal engineering. *CrystEngComm* **2010,** *12* (1), 22-43.

28.   Kato, M.; Fujihara, T.; Yano, D.; Nagasawa, A., Anion influence on the coordination polymer structures of silver(I) complexes with 2-methylisothiazol-3(2H)-one. *CrystEngComm* **2008,** *10* (10), 1460-1466.

29.   Sague, J. L.; Meuwly, M.; Fromm, K. M., Counterion effect on the formation of coordination polymer networks between AgNO$_3$ and L (2,2′-oxybis(ethane-2,1-diyl) diisonicotinate). Part 2. *CrystEngComm* **2008,** *10* (11), 1542-1549.

30.   Noro, S. I.; Horike, S.; Tanaka, D.; Kitagawa, S.; Akutagawa, T.; Nakamura, T., Flexible and shape-selective guest binding at Cu^{II} axial sites in 1-dimensional Cu^{II}−1,2-Bis(4-pyridyl)ethane coordination polymers. *Inorganic Chemistry* **2006,** *45* (23), 9290-9300.

31.   Paz, F. A. A.; Klinowski, J.; Vilela, S. M.; Tome, J. P.; Cavaleiro, J. A.; Rocha, J., Ligand design for functional metal–organic frameworks. *Chemical Society Reviews* **2012,** *41* (3), 1088-1110.

32.   Lazarou, K. N.; Psycharis, V.; Terzis, A.; Raptopoulou, C. P., Network diversity and supramolecular isomerism in copper(II)/1,2-bis(4-pyridyl)ethane coordination polymers. *Polyhedron* **2011,** *30* (6), 963-970.

33.   Halder, A.; Bhattacharya, B.; Haque, F.; Ghoshal, D., Structural diversity in six mixed ligand Zn (II) metal–organic frameworks constructed by rigid and flexible dicarboxylates and different N, N′ donor ligands. *Crystal Growth & Design* **2017,** *17* (12), 6613-6624.

34.   Zhao, D.; Timmons, D. J.; Yuan, D.; Zhou, H. C., Tuning the topology and functionality of metal–organic frameworks by ligand design. *Accounts of chemical research* **2011,** *44* (2), 123-133.

35.   He, H.; Collins, D.; Dai, F.; Zhao, X.; Zhang, G.; Ma, H.; Sun, D., Construction of metal−organic frameworks with 1D chain, 2D grid, and 3D porous

framework based on a flexible imidazole ligand and rigid benzenedicarboxylates. *Crystal growth & design* **2010,** *10* (2), 895-902.

36.   Konavarapu, S. K.; Goswami, A.; Kumar, A. G.; Banerjee, S.; Biradha, K., MOFs containing a linear bis-pyridyl-tris-amide and angular carboxylates: exploration of proton conductivity, water vapor and dye sorptions. *Inorganic Chemistry Frontiers* **2019,** *6* (1), 184-191.

37.   Hou, G. G.; Liu, Y.; Liu, Q. K.; Ma, J. P.; Dong, Y. B., NbO lattice MOFs based on octahedral M (II) and ditopic pyridyl substituted diketonate ligands: Structure, encapsulation and guest-driven luminescent property. *Chemical Communications* **2011,** *47* (38), 10731-10733.

38.   Chen, B.; Wang, L.; Xiao, Y.; Fronczek, F. R.; Xue, M.; Cui, Y.; Qian, G., A luminescent metal–organic framework with Lewis basic pyridyl sites for the sensing of metal ions. *Angewandte Chemie* **2009,** *121* (3), 508-511.

39.   Adarsh, N.; Kumar, D. K.; Dastidar, P., Zn(II) metal–organic frameworks (MOFs) derived from a bis-pyridyl-bis-urea ligand: effects of crystallization solvents on the structures and anion binding properties. *CrystEngComm* **2008,** *10* (11), 1565-1573.

40.   Tan, X.; Li, L.; Zhang, J.; Han, X.; Jiang, L.; Li, F.; Su, C. Y., Three-dimensional phosphine metal–organic frameworks assembled from Cu(I) and pyridyl diphosphine. *Chemistry of Materials* **2012,** *24* (3), 480-485.

41.   Liang, R.; Guo, Y.; Wang, Y.; Xuan, X., Ligand geometry-driven formation of Zn(II) MOFs based on 1, 3-bis [2-(4-pyridyl) ethenyl] benzene and aromatic dicarboxylic acids. *Inorganica Chimica Acta* **2018,** *471*, 50-56.

42.   Zhang, S.; Yang, Y.; Xia, Z. Q.; Liu, X. Y.; Yang, Q.; Wei, Q.; Xie, G.; Chen, S. P.; Gao, S. L., Eu-MOFs with 2-(4-carboxyphenyl) imidazo [4, 5-f]-1, 10-phenanthroline and ditopic carboxylates as coligands: synthesis, structure, high thermostability, and luminescence properties. *Inorganic Chemistry* **2014,** *53* (20), 10952-10963.

43.   Yang, D.; Chen, Y.; Su, Z.; Zhang, X.; Zhang, W.; Srinivas, K., Organic carboxylate-based MOFs and derivatives for electrocatalytic water oxidation. *Coordination Chemistry Reviews* **2021,** *428*, 213619.

44.   Andreeva, A. B.; Le, K. N.; Chen, L.; Kellman, M. E.; Hendon, C. H.; Brozek, C. K., Soft mode metal-linker dynamics in carboxylate MOFs evidenced by variable-temperature infrared spectroscopy. *Journal of the American Chemical Society* **2020,** *142* (45), 19291-19299.

45.   Bury, W.; Justyniak, I.; Prochowicz, D.; Wróbel, Z.; Lewiński, J., Oxozinc carboxylates: a predesigned platform for modelling prototypical Zn-MOFs' reactivity toward water and donor solvents. *Chemical Communications* **2012,** *48* (59), 7362-7364.

46.   Xie, X. X.; Yang, Y. C.; Dou, B. H.; Li, Z. F.; Li, G., Proton conductive carboxylate-based metal–organic frameworks. *Coordination Chemistry Reviews* **2020,** *403*, 213100.

47.   Leszczyński, M. K.; Kornowicz, A.; Prochowicz, D.; Justyniak, I.; Noworyta, K.; Lewinski, J., Straightforward synthesis of single-crystalline and redox-active Cr (II)-carboxylate MOFs. *Inorganic chemistry* **2018,** *57* (9), 4803-4806.

48.   Yuan, J. T.; Hou, J. J.; Liu, X. L.; Feng, Y. R.; Zhang, X. M., Optimized trimetallic benzotriazole-5-carboxylate MOFs with coordinately unsaturated active sites as an efficient electrocatalyst for the oxygen evolution reaction. *Dalton Transactions* **2020,** *49* (3), 750-756.

49.   Saghian, M.; Dehghanpour, S.; Sharbatdaran, M., Cyano-bifunctional MOFs as superior catalysts for carbon dioxide fixation under co-catalyst and solvent free conditions. *Applied Catalysis A: General* **2021,** *612*, 117982.

50.   Tella, A.; Eliagwu, S.; Amali, M.; Kola-Mustapha, A.; Olatunji, S.; Ishola, F.; Adimula, V.; Oluwafemi, O., Synthesis and characterization of amino and cyano-functionalized zinc-terephthalate metal–organic frameworks for loading of piroxicam drug. *Chemical Papers* **2020,** *74* (7), 2287-2296.

51.   Mironov, Y. V.; Naumov, N. G.; Brylev, K. A.; Efremova, O. A.; Fedorov, V. E.; Hegetschweiler, K., Rhenium–chalcogenide–cyano clusters, Cu^{2+} Ions, and 1, 2, 3, 4 - tetraaminobutane as molecular building blocks for chiral coordination polymers. *Angewandte Chemie International Edition* **2004,** *43* (10), 1297-1300.

52.   Li, B.; Yan, Q. Q.; Xu, Z. Q.; Xu, Y. B.; Yong, G. P., Tuning the interpenetration of metal–organic frameworks through changing ligand functionality: effect on gas adsorption properties. *CrystEngComm* **2020,** *22* (3), 506-514.

53.   Degaga, G. D.; Pandey, R.; Gupta, C.; Bharadwaj, L., Tailoring of the electronic property of Zn-BTC metal–organic framework via ligand functionalization: An ab initio investigation. *RSC advances* **2019,** *9* (25), 14260-14267.

54. Xia, J.; Shi, W.; Chen, X. Y.; Wang, H. S.; Cheng, P.; Liao, D. Z.; Yan, S. P., A CNT-like coordination tube with cyano-bridges. *Dalton Transactions* **2007,** (23), 2373-2375.

55. Wang, Y.; Xu, P.; Xie, Q.; Ma, Q. Q.; Meng, Y. H.; Wang, Z. W.; Zhang, S.; Zhao, X. J.; Chen, J.; Wang, Z. L., Cadmium (II)–triazole framework as a luminescent probe for Ca^{2+} and cyano complexes. *Chemistry–A European Journal* **2016,** *22* (30), 10459-10474.

56. Peng, Y.; Zhang, X.; Wu, X.; Li, M.; Zhang, Y.; Jiang, T.; Yang, R., A water-stable cyano-functionalized metal-organic framework as an efficient adsorbent of uranyl ion. *Materials Research Express* **2019,** *6* (12), 125505.

57. Wang, Y.; Zhou, Y. N.; Liang, Y.; Cheng, L.; Fang, Y., Chiral fluorescent metal–organic framework with a pentanuclear copper cluster as an efficient luminescent probe for Dy^{3+} ion and cyano compounds. *Inorganic Chemistry* **2021,** *60* (20), 15085-15090.

58. Canossa, S.; Gonzalez-Nelson, A.; Shupletsov, L.; del Carmen Martin, M.; Van der Veen, M. A., Overcoming crystallinity limitations of aluminium metal-organic frameworks by oxalic acid modulated synthesis. *Chemistry–A European Journal* **2020,** *26* (16), 3564-3570.

59. Shi, F. N.; Ananias, D.; Yang, T. H.; Rocha, J., Synthesis and characterization of polymorphs of photoluminescent Eu (III)-(2, 5-furandicarboxylic acid, oxalic acid) MOFs. *Journal of Solid State Chemistry* **2013,** *204*, 321-328.

60. Hou, K. L.; Bai, F. Y.; Xing, Y. H.; Wang, J. L.; Shi, Z., A novel family of 3D photoluminescent lanthanide–bta–flexible MOFs constructed from 1, 2, 4, 5-benzenetetracarboxylic acid and different spanning of dicarboxylate acid ligands. *CrystEngComm* **2011,** *13* (11), 3884-3894.

61. Wei, Y.; Sa, R.; Wu, K., A highly stable and white-light-emitting Eu (III) MOF. *Dalton Transactions* **2016,** *45* (46), 18661-18667.

62. Jin, H. G.; Yan, Y. Z.; Li, J.; Gu, Z. G.; Chen, J. H.; Liu, Y. T.; Zheng, Z. P.; Zhan, Q. G.; Cai, Y. P., 1-D to 3-D lanthanide coordination polymers constructed from 5-aminoisophthalic acid and oxalic acid. *Inorganic Chemistry Communications* **2012,** *23*, 25-30.

63. Hamouda, M. A.; Sheta, S. M.; Sheha, R. R.; Kandil, A.; Ali, O. I.; El-Sheikh, S. M., A novel strontium-based MOF: synthesis, characterization, and promising application in removal of $^{152+154}$Eu from active waste. *RSC advances* **2022,** *12* (21), 13103-13110.

64.   Zhan, Z.; Jia, Y.; Li, D.; Zhang, X.; Hu, M., A water-stable terbium-MOF sensor for the selective, sensitive, and recyclable detection of Al^{3+} and CO_3^{2-} ions. *Dalton Transactions* **2019,** *48* (40), 15255-15262.

65.   Kumar, R. S.; Kumar, S. S.; Kulandainathan, M. A., Highly selective electrochemical reduction of carbon dioxide using Cu based metal organic framework as an electrocatalyst. *Electrochemistry Communications* **2012,** *25*, 70-73.

66.   Gagnon, K. J.;   Perry, H. P.; Clearfield, A., Conventional and unconventional metal–organic frameworks based on phosphonate ligands: MOFs and UMOFs. *Chemical reviews* **2012,** *112* (2), 1034-1054.

67.   Hassanzadeh Fard, Z.; Wong, N. E.; Malliakas, C. D.; Ramaswamy, P.; Taylor, J. M.; Otsubo, K.; Shimizu, G. K., Superprotonic phase change to a robust phosphonate metal–organic framework. *Chemistry of Materials* **2018,** *30* (2), 314-318.

68.   Tholen, P.; Zorlu, Y.; Beckmann, J.; Yücesan, G., Probing isoreticular expansions in phosphonate MOFs and their applications. *European Journal of Inorganic Chemistry* **2020,** *2020* (17), 1542-1554.

69.   Zheng, T.; Yang, Z.; Gui, D.; Liu, Z.; Wang, X.; Dai, X.; Liu, S.; Zhang, L.; Gao, Y.; Chen, L., Overcoming the crystallization and designability issues in the ultrastable zirconium phosphonate framework system. *Nature communications* **2017,** *8* (1), 1-11.

70.   Taddei, M.; Costantino, F.; Ienco, A.; Comotti, A.; Dau, P. V.; Cohen, S. M., Synthesis, breathing, and gas sorption study of the first isoreticular mixed-linker phosphonate based metal–organic frameworks. *Chemical Communications* **2013,** *49* (13), 1315-1317.

71.   Steinke, F.; Javed, A.; Wöhlbrandt, S.; Tiemann, M.; Stock, N., New isoreticular phosphonate MOFs based on a tetratopic linker. *Dalton Transactions* **2021,** *50* (38), 13572-13579.

72.   Lian, X.; Yan, B., Phosphonate MOFs composite as off–on fluorescent sensor for detecting purine metabolite uric acid and diagnosing hyperuricuria. *Inorganic Chemistry* **2017,** *56* (12), 6802-6808.

73.   Bao, S. S.; Shimizu, G. K.; Zheng, L. M., Proton conductive metal phosphonate frameworks. *Coordination Chemistry Reviews* **2019,** *378*, 577-594.

74.   Fard, Z.; Kalinovskyy, Y.; Spasyuk, D.; Blight, B.; Shimizu, G., Alkaline-earth phosphonate MOFs with reversible hydration-dependent fluorescence. *Chemical Communications* **2016,** *52* (87), 12865-12868.

75.   Liu, R.; Wang, D. Y.; Shi, J. R.; Li, G., Proton conductive metal sulfonate frameworks. *Coordination Chemistry Reviews* **2021,** *431*, 213747.

76.   Shimizu, G. K.; Vaidhyanathan, R.; Taylor, J. M., Phosphonate and sulfonate metal organic frameworks. *Chemical Society Reviews* **2009,** *38* (5), 1430-1449.

77.   Zhang, G.; Fei, H., Synthesis and applications of porous organosulfonate-based metal-organic frameworks. *Metal-Organic Framework* **2020**, 203-214.

78.   Zhang, G.; Wei, G.; Liu, Z.; Oliver, S. R.; Fei, H., A robust sulfonate-based metal–organic framework with permanent porosity for efficient CO_2 capture and conversion. *Chemistry of Materials* **2016,** *28* (17), 6276-6281.

79.   Zhang, G.; Fei, H., Missing metal-linker connectivities in a 3-D robust sulfonate-based metal–organic framework for enhanced proton conductivity. *Chemical Communications* **2017,** *53* (29), 4156-4159.

80.   Raptopoulou, C. P., Metal-Organic Frameworks: Synthetic methods and potential applications. *Materials (Basel)* **2021,** *14* (2).

81.   Li, H.; Eddaoudi, M.; O'Keeffe, M.; Yaghi, O. M., Design and synthesis of an exceptionally stable and highly porous metal-organic framework. *Nature* **1999,** *402* (6759), 276-279.

82.   Halper, S. R.; Do, L.; Stork, J. R.; Cohen, S. M., Topological control in heterometallic metal−organic frameworks by anion templating and metalloligand design. *Journal of the American Chemical Society* **2006,** *128* (47), 15255-15268.

83.   Al Amery, N.; Abid, H. R.; Al-Saadi, S.; Wang, S.; Liu, S., Facile directions for synthesis, modification and activation of MOFs. *Materials Today Chemistry* **2020,** *17*, 100343.

84.   Dey, C.; Kundu, T.; Biswal, B. P.; Mallick, A.; Banerjee, R., Crystalline metal-organic frameworks (MOFs): synthesis, structure and function. *Acta Crystallographica Section B: Structural Science, Crystal Engineering and Materials* **2014,** *70* (1), 3-10.

85.   Murugesan, K.; Senthamarai, T.; Sohail, M.; Alshammari, A. S.; Pohl, M.-M.; Beller, M.; Jagadeesh, R. V., Cobalt-based nanoparticles prepared from

MOF–carbon templates as efficient hydrogenation catalysts. *Chemical science* **2018,** *9* (45), 8553-8560.

86.   Yoo, Y.; Varela-Guerrero, V.; Jeong, H.-K., Isoreticular metal− organic frameworks and their membranes with enhanced crack resistance and moisture stability by surfactant-assisted drying. *Langmuir* **2011,** *27* (6), 2652-2657.

87.   Rabenau, A., The role of hydrothermal synthesis in preparative chemistry. *Angewandte Chemie International Edition in English* **1985,** *24* (12), 1026-1040.

88.   Jabbari, V.; Veleta, J.; Zarei-Chaleshtori, M.; Gardea-Torresdey, J.; Villagrán, D., Green synthesis of magnetic MOF@ GO and MOF@ CNT hybrid nanocomposites with high adsorption capacity towards organic pollutants. *Chemical Engineering Journal* **2016,** *304*, 774-783.

89.   Li, J.; Cheng, S.; Zhao, Q.; Long, P.; Dong, J., Synthesis and hydrogen-storage behavior of metal–organic framework MOF-5. *International Journal of Hydrogen Energy* **2009,** *34* (3), 1377-1382.

90.   Yaghi, O. M.; Li, H., Hydrothermal synthesis of a metal-organic framework containing large rectangular channels. *Journal of the American Chemical Society* **1995,** *117* (41), 10401-10402.

91.   Chui, S. S. Y.; Lo, S. M. F.; Charmant, J. P. H.; Orpen, A. G.; Williams, I. D., A chemically functionalizable nanoporous material. *Science* **1999,** *283* (5405), 1148-1150.

92.   Stock, N.; Biswas, S., Synthesis of metal-organic frameworks (mofs): routes to various mof topologies, morphologies, and composites. *Chemical Reviews* **2012,** *112* (2), 933-969.

93.   Dybtsev, D. N.; Nuzhdin, A. L.; Chun, H.; Bryliakov, K. P.; Talsi, E. P.; Fedin, V. P.; Kim, K., A homochiral metal–organic material with permanent porosity, enantioselective sorption properties, and catalytic activity. *Angewandte Chemie International Edition* **2006,** *45* (6), 916-920.

94.   Bhattacharjee, S.; Choi, J.-S.; Yang, S.-T.; Choi, S. B.; Kim, J.; Ahn, W. S., Solvothermal synthesis of Fe-MOF-74 and its catalytic properties in phenol hydroxylation. *Journal of nanoscience and nanotechnology* **2010,** *10* (1), 135-141.

95.   Remya, V.; Kurian, M., Synthesis and catalytic applications of metal–organic frameworks: a review on recent literature. *International Nano Letters* **2019,** *9* (1), 17-29.

96.   Mehmandoust, M. R.; Motakef-Kazemi, N.; Ashouri, F., Nitrate adsorption from aqueous solution by metal–organic framework MOF-5. *Iranian journal of science and technology, Transactions a: science* **2019,** *43* (2), 443-449.

97.   Biemmi, E.; Christian, S.; Stock, N.; Bein, T., High-throughput screening of synthesis parameters in the formation of the metal-organic frameworks MOF-5 and HKUST-1. *Microporous and Mesoporous Materials* **2009,** *117* (1), 111-117.

98.   Millange, F.; El Osta, R.; Medina, M. E.; Walton, R. I., A time-resolved diffraction study of a window of stability in the synthesis of a copper carboxylate metal–organic framework. *CrystEngComm* **2011,** *13* (1), 103-108.

99.   Zhao, Z.; Li, Z.; Lin, Y., Adsorption and diffusion of carbon dioxide on metal−organic framework (MOF-5). *Industrial & Engineering Chemistry Research* **2009,** *48* (22), 10015-10020.

100.   Martinez Joaristi, A.; Juan-Alcañiz, J.; Serra-Crespo, P.; Kapteijn, F.; Gascon, J., Electrochemical synthesis of some archetypical Zn^{2+}, Cu^{2+}, and Al^{3+} metal−organic frameworks. *Crystal Growth & Design* **2012,** *12* (7), 3489-3498.

101.   Li, W. J.; Tu, M.; Cao, R.; Fischer, R. A., Metal–organic framework thin films: electrochemical fabrication techniques and corresponding applications & perspectives. *Journal of Materials Chemistry A* **2016,** *4* (32), 12356-12369.

102.   Zhang, X.; Wan, K.; Subramanian, P.; Xu, M.; Luo, J.; Fransaer, J., Electrochemical deposition of metal–organic framework films and their applications. *Journal of Materials Chemistry A* **2020,** *8* (16), 7569-7587.

103.   Yang, H.; Song, X.; Yang, T.; Liang, Z.; Fan, C.; Hao, X., Electrochemical synthesis of flower shaped morphology MOFs in an ionic liquid system and their electrocatalytic application to the hydrogen evolution reaction. *RSC Advances* **2014,** *4* (30), 15720-15726.

104.   Campagnol, N.; Van Assche, T.; Boudewijns, T.; Denayer, J.; Binnemans, K.; De Vos, D.; Fransaer, J., High pressure, high temperature electrochemical synthesis of metal–organic frameworks: films of MIL-100 (Fe) and HKUST-1 in different morphologies. *Journal of Materials Chemistry A* **2013,** *1* (19), 5827-5830.

105.   Lu, C.; Ben, T.; Xu, S.; Qiu, S., Electrochemical synthesis of a microporous conductive polymer based on a metal–organic framework thin film. *Angewandte Chemie* **2014,** *126* (25), 6572-6576.

106.   Wang, X.; She, P.; Zhang, Q., Recent advances on electrochemical methods in fabricating two‑dimensional organic‑ligand‑containing frameworks. *SmartMat* **2021,** *2* (3), 299-325.

107.   Aslani, A.; Morsali, A., Sonochemical synthesis of nano-sized metal-organic lead(II) polymer: A precursor for the preparation of nano-structured lead(II) iodide and lead(II) oxide. *Inorganica Chimica Acta* **2009,** *362* (14), 5012-5016.

108.   Carson, C. G.; Brown, A. J.; Sholl, D. S.; Nair, S., Sonochemical synthesis and characterization of submicrometer crystals of the metal–organic framework $Cu[(hfipbb)(H_2hfipbb)_{0.5}]$. *Crystal Growth & Design* **2011,** *11* (10), 4505-4510.

109.   Kim, J.; Yang, S.-T.; Choi, S. B.; Sim, J.; Kim, J.; Ahn, W.-S., Control of catenation in CuTATB-n metal–organic frameworks by sonochemical synthesis and its effect on CO_2 adsorption. *Journal of Materials Chemistry* **2011,** *21* (9), 3070-3076.

110.   Son, W.-J.; Kim, J.; Kim, J.; Ahn, W. S., Sonochemical synthesis of MOF-5. *Chemical Communications* **2008,** (47), 6336-6338.

111.   Jung, D. W.; Yang, D. A.; Kim, J.; Kim, J.; Ahn, W. S., Facile synthesis of MOF-177 by a sonochemical method using 1-methyl-2-pyrrolidinone as a solvent. *Dalton Transactions* **2010,** *39* (11), 2883-2887.

112.   Tanhaei, M.; Mahjoub, A. R.; Safarifard, V., Energy-efficient sonochemical approach for the preparation of nanohybrid composites from graphene oxide and metal-organic framework. *Inorganic Chemistry Communications* **2019,** *102*, 185-191.

113.   Yu, K.; Lee, Y. R.; Seo, J. Y.; Baek, K. Y.; Chung, Y.-M.; Ahn, W.-S., Sonochemical synthesis of Zr-based porphyrinic MOF-525 and MOF-545: Enhancement in catalytic and adsorption properties. *Microporous and Mesoporous Materials* **2021,** *316*, 110985.

114.   Abbasloo, F.; Khosravani, S. A.; Ghaedi, M.; Dashtian, K.; Hosseini, E.; Manzouri, L.; Khorramrooz, S. S.; Sharifi, A.; Jannesar, R.; Sadri, F., Sonochemical-solvothermal synthesis of guanine embedded copper based metal-organic framework (MOF) and its effect on oprD gene expression in clinical and standard strains of Pseudomonas aeruginosa. *Ultrasonics sonochemistry* **2018,** *42*, 237-243.

115.   Abuzalat, O.; Wong, D.; Elsayed, M.; Park, S.; Kim, S., Sonochemical fabrication of Cu (II) and Zn (II) metal-organic framework films on metal substrates. *Ultrasonics Sonochemistry* **2018,** *45*, 180-188.

116.   Hu, Y.; Liu, C.; Zhang, Y.; Ren, N.; Tang, Y., Microwave-assisted hydrothermal synthesis of nanozeolites with controllable size. *Microporous and Mesoporous Materials* **2009,** *119* (1), 306-314.

117.   Zhang, S. H.; Song, Y.; Liang, H.; Zeng, M. H., Microwave-assisted synthesis, crystal structure and properties of a disc-like heptanuclear Co(II) cluster and a heterometallic cubanic Co(II) cluster. *CrystEngComm* **2009,** *11* (5), 865-872.

118.   Klinowski, J.; Almeida Paz, F. A.; Silva, P.; Rocha, J., Microwave-assisted synthesis of metal–organic frameworks. *Dalton Transactions* **2011,** *40* (2), 321-330.

119.   Lin, Z. J.; Yang, Z.; Liu, T. F.; Huang, Y. B.; Cao, R., Microwave-assisted synthesis of a series of lanthanide metal–organic frameworks and gas sorption properties. *Inorganic Chemistry* **2012,** *51* (3), 1813-1820.

120.   Xiang, Z.; Cao, D.; Shao, X.; Wang, W.; Zhang, J.; Wu, W., Facile preparation of high-capacity hydrogen storage metal-organic frameworks: A combination of microwave-assisted solvothermal synthesis and supercritical activation. *Chemical engineering science* **2010,** *65* (10), 3140-3146.

121.   Babu, R.; Roshan, R.; Kathalikkattil, A. C.; Kim, D. W.; Park, D. W., Rapid, microwave-assisted synthesis of cubic, three-dimensional, highly porous MOF-205 for room temperature CO_2 fixation via cyclic carbonate synthesis. *ACS Applied Materials & Interfaces* **2016,** *8* (49), 33723-33731.

122.   Chen, Y.; Ni, D.; Yang, X.; Liu, C.; Yin, J.; Cai, K., Microwave-assisted synthesis of honeycomblike hierarchical spherical Zn-doped Ni-MOF as a high-performance battery-type supercapacitor electrode material. *Electrochimica Acta* **2018,** *278*, 114-123.

123.   Jiang, Y.; Zhang, X.; Dai, X.; Zhang, W.; Sheng, Q.; Zhuo, H.; Xiao, Y.; Wang, H., Microwave-assisted synthesis of ultrafine Au nanoparticles immobilized on MOF-199 in high loading as efficient catalysts for a three-component coupling reaction. *Nano Research* **2017,** *10* (3), 876-889.

124.   Chen, C.; Feng, X.; Zhu, Q.; Dong, R.; Yang, R.; Cheng, Y.; He, C., Microwave-assisted rapid synthesis of well-shaped MOF-74 (Ni) for CO_2 efficient capture. *Inorganic Chemistry* **2019,** *58* (4), 2717-2728.

125.   Albuquerque, G. H.; Fitzmorris, R. C.; Ahmadi, M.; Wannenmacher, N.; Thallapally, P. K.; McGrail, B. P.; Herman, G. S., Gas–liquid segmented flow microwave-assisted synthesis of MOF-74 (Ni) under moderate pressures. *CrystEngComm* **2015,** *17* (29), 5502-5510.

126.   Seo, Y. K.; Hundal, G.; Jang, I. T.; Hwang, Y. K.; Jun, C. H.; Chang, J. S., Microwave synthesis of hybrid inorganic–organic materials including porous $Cu_3(BTC)_2$ from Cu(II)-trimesate mixture. *Microporous and Mesoporous Materials* **2009,** *119* (1), 331-337.

127.   Cohen, S. M., Postsynthetic methods for the functionalization of metal–organic frameworks. *Chemical Reviews* **2012,** *112* (2), 970-1000.

128.   Tanabe, K. K.; Cohen, S. M., Postsynthetic modification of metal–organic frameworks—a progress report. *Chemical Society Reviews* **2011,** *40* (2), 498-519.

129.   Song, Y. F.; Cronin, L., Postsynthetic covalent modification of metal–organic framework (MOF) materials. *Angewandte Chemie International Edition* **2008,** *47* (25), 4635-4637.

130.   Karagiaridi, O.; Bury, W.; Mondloch, J. E.; Hupp, J. T.; Farha, O. K., Solvent-assisted linker exchange: an alternative to the de novo synthesis of unattainable metal–organic frameworks. *Angewandte Chemie International Edition* **2014,** *53* (18), 4530-4540.

131.   Young, C.; Wang, J.; Kim, J.; Sugahara, Y.; Henzie, J.; Yamauchi, Y., Controlled chemical vapor deposition for synthesis of nanowire arrays of metal–organic frameworks and their thermal conversion to carbon/metal oxide hybrid materials. *Chemistry of Materials* **2018,** *30* (10), 3379-3386.

132.   Zhang, M.; Guan, J.; Zhang, B.; Su, D.; Williams, C. T.; Liang, C., Chemical vapor deposition of $Pd(C_3H_5)(C_5H_5)$ to synthesize Pd@MOF-5 catalysts for Suzuki coupling reaction. *Catalysis Letters* **2012,** *142* (3), 313-318.

133.   Hermes, S.; Schröter, M. K.; Schmid, R.; Khodeir, L.; Muhler, M.; Tissler, A.; Fischer, R. W.; Fischer, R. A., Metal@MOF: loading of highly porous coordination polymers host lattices by metal organic chemical vapor deposition. *Angewandte Chemie International Edition* **2005,** *44* (38), 6237-6241.

134.   Decoste, J. B.; Peterson, G. W.; Smith, M. W.; Stone, C. A.; Willis, C. R., Enhanced stability of Cu-BTC MOF via perfluorohexane plasma-enhanced chemical vapor deposition. *Journal of the American Chemical Society* **2012,** *134* (3), 1486-1489.

135.   Gatteschi, D., Molecular magnetism: a basis for new materials. *Advanced Materials* **1994,** *6* (9), 635-645.

136.   Bain, G. A.; Berry, J. F., Diamagnetic corrections and pascal's constants. *Journal of Chemical Education* **2008,** *85* (4), 532.

137.   Thorarinsdottir, A. E.; Harris, T. D., Metal–organic framework magnets. *Chemical reviews* **2020,** *120* (16), 8716-8789.

138.   Fagan-Endres, M. Fundamental studies of heap leaching hydrology using magnetic resonance imaging. **2013**.

139.   Espallargas, G. M.; Coronado, E., Magnetic functionalities in MOFs: from the framework to the pore. *Chemical Society Reviews* **2018,** *47* (2), 533-557.

140.   Luzon, J.; Sessoli, R., Lanthanides in molecular magnetism: so fascinating, so challenging. *Dalton Transactions* **2012,** *41* (44), 13556-13567.

141.   Jia, H.; Yao, Y.; Zhao, J.; Gao, Y.; Luo, Z.; Du, P., A novel two-dimensional nickel phthalocyanine-based metal–organic framework for highly efficient water oxidation catalysis. *Journal of Materials Chemistry A* **2018,** *6* (3), 1188-1195.

142.   Nagatomi, H.; Yanai, N.; Yamada, T.; Shiraishi, K.; Kimizuka, N., Synthesis and electric properties of a two-dimensional metal-organic framework based on phthalocyanine. *Chemistry–A European Journal* **2018,** *24* (8), 1806-1810.

143.   Yang, C.; Dong, R.; Wang, M.; Petkov, P. S.; Zhang, Z.; Wang, M.; Han, P.; Ballabio, M.; Bräuninger, S. A.; Liao, Z., A semiconducting layered metal-organic framework magnet. *Nature communications* **2019,** *10* (1), 1-9.

144.   Meng, Z.; Aykanat, A.; Mirica, K. A., Welding metallophthalocyanines into bimetallic molecular meshes for ultrasensitive, low-power chemiresistive detection of gases. *Journal of the American Chemical Society* **2018,** *141* (5), 2046-2053.

145.   Faust, T. B.; D'Alessandro, D. M., Radicals in metal–organic frameworks. *Rsc Advances* **2014,** *4* (34), 17498-17512.

146.   Perlepe, P.; Oyarzabal, I.; Mailman, A.; Yquel, M.; Platunov, M.; Dovgaliuk, I.; Rouzières, M.; Négrier, P.; Mondieig, D.; Suturina, E. A., Metal-organic magnets with large coercivity and ordering temperatures up to 242°C. *Science* **2020,** *370* (6516), 587-592.

147.   Feltham, H. L.; Brooker, S., Review of purely 4f and mixed-metal nd-4f single-molecule magnets containing only one lanthanide ion. *Coordination Chemistry Reviews* **2014,** *276*, 1-33.

148.   Craig, G. A.; Murrie, M., 3d single-ion magnets. *Chemical Society Reviews* **2015,** *44* (8), 2135-2147.

149.   Cervetti, C.; Heintze, E.; Bogani, L., Interweaving spins with their environment: novel inorganic nanohybrids with controllable magnetic properties. *Dalton transactions* **2014,** *43* (11), 4220-4232.

150.   Aromí, G.; Aguila, D.; Gamez, P.; Luis, F.; Roubeau, O., Design of magnetic coordination complexes for quantum computing. *Chemical Society Reviews* **2012,** *41* (2), 537-546.

151. Bagai, R.; Christou, G., The drosophila of single-molecule magnetism:[$Mn_{12}O_{12}(O_2CR)_{16}(H_2O)_4$]. *Chemical Society Reviews* **2009,** *38* (4), 1011-1026.

152. Wang, X. Y.; Avendaño, C.; Dunbar, K. R., Molecular magnetic materials based on 4d and 5d transition metals. *Chemical Society Reviews* **2011,** *40* (6), 3213-3238.

153. Sanvito, S., Filtering spins with molecules. *Nature materials* **2011,** *10* (7), 484-485.

154. Sessoli, R.; Tsai, H. L.; Schake, A. R.; Wang, S.; Vincent, J. B.; Folting, K.; Gatteschi, D.; Christou, G.; Hendrickson, D. N., High-spin molecules: [$Mn_{12}O_{12}(O_2CR)_{16}(H_2O)_4$]. *Journal of the American Chemical Society* **1993,** *115* (5), 1804-1816.

155. Weinland, R.; Fischer, G., Über manganiacetate und‐benzoate. *Zeitschrift für anorganische und allgemeine Chemie* **1921,** *120* (1), 161-180.

156. Gatteschi, D.; Sessoli, R., Quantum tunneling of magnetization and related phenomena in molecular materials. *Angewandte Chemie International Edition* **2003,** *42* (3), 268-297.

157. Zadrozny, J. M.; Xiao, D. J.; Atanasov, M.; Long, G. J.; Grandjean, F.; Neese, F.; Long, J. R., Magnetic blocking in a linear iron (I) complex. *Nature chemistry* **2013,** *5* (7), 577-581.

158. Yao, X.-N.; Du, J. Z.; Zhang, Y. Q.; Leng, X. B.; Yang, M. W.; Jiang, S. D.; Wang, Z. X.; Ouyang, Z. W.; Deng, L.; Wang, B. W., Two-coordinate Co (II) imido complexes as outstanding single-molecule magnets. *Journal of the American Chemical Society* **2017,** *139* (1), 373-380.

159. Liddle, S. T.; van Slageren, J., Improving f-element single molecule magnets. *Chemical Society Reviews* **2015,** *44* (19), 6655-6669.

160. Habib, F.; Brunet, G.; Vieru, V.; Korobkov, I.; Chibotaru, L. F.; Murugesu, M., Significant enhancement of energy barriers in dinuclear dysprosium single-molecule magnets through electron-withdrawing effects. *Journal of the American Chemical Society* **2013,** *135* (36), 13242-13245.

161. Demir, S.; Jeon, I.-R.; Long, J. R.; Harris, T. D., Radical ligand-containing single-molecule magnets. *Coordination Chemistry Reviews* **2015,** *289*, 149-176.

162.   Liddle, S. T.; van Slageren, J., Improving f-element single molecule magnets. *Chem Soc Rev* **2015,** *44* (19), 6655-69.

163.   Feltham, H. L. C.; Brooker, S., Review of purely 4f and mixed-metal nd-4f single-molecule magnets containing only one lanthanide ion. *Coordination Chemistry Reviews* **2014,** *276*, 1-33.

164.   Xie, T.; Nikitin, S.; Kolesnikov, A.; Mamontov, E.; Anovitz, L.; Ehlers, G.; Huskić, I.; Friščić, T.; Podlesnyak, A., Direct determination of the zero-field splitting for Fe^{3+} ion in a synthetic polymorph of the oxalate mineral stepanovite $NaMgFe (C_2O_4)_3 9H_2O$: a natural MOF. *Angewandte Chemie International Edition* **2022,** *134* (6), 268-297.

165.   Khan, S. Zero-Field Splitting in Gd (III) complexes: Towards a molecular understanding of paramagnetic relaxation. Department of Physics, Stockholm University, 2015.

166.   Sessoli, R.; Powell, A. K., Strategies towards single molecule magnets based on lanthanide ions. *Coordination Chemistry Reviews* **2009,** *253* (19), 2328-2341.

167.   Gao, S.; Affronte, M., *Molecular nanomagnets and related phenomena*. Springer: 2015.

168.   Christou, G.; Gatteschi, D.; Hendrickson, D. N.; Sessoli, R., Single-molecule magnets. *MRS Bulletin* **2000,** *25* (11), 66-71.

169.   Russell, H. N.; Saunders, F. A., New regularities in the spectra of the alkaline earths. *The Astrophysical Journal* **1925,** *61*, 38.

170.   Rinehart, J. D.; Long, J. R., Exploiting single-ion anisotropy in the design of f-element single-molecule magnets. *Chemical Science* **2011,** *2* (11), 2078-2085.

171.   Sørensen, M. A.; Weihe, H.; Vinum, M. G.; Mortensen, J. S.; Doerrer, L. H.; Bendix, J., Imposing high-symmetry and tuneable geometry on lanthanide centres with chelating Pt and Pd metalloligands. *Chemical science* **2017,** *8* (5), 3566-3575.

172.   Chen, Y. C.; Liu, J. L.; Ungur, L.; Liu, J.; Li, Q. W.; Wang, L. F.; Ni, Z. P.; Chibotaru, L. F.; Chen, X. M.; Tong, M. L., Symmetry-supported magnetic blocking at 20 K in pentagonal bipyramidal Dy (III) single-ion magnets. *Journal of the American Chemical Society* **2016,** *138* (8), 2829-2837.

173.   Perfetti, M.; Gysler, M.; Rechkemmer-Patalen, Y.; Zhang, P.; Taştan, H.; Fischer, F.; Netz, J.; Frey, W.; Zimmermann, L. W.; Schleid, T., Determination of

the electronic structure of a dinuclear dysprosium single molecule magnet without symmetry idealization. *Chemical science* **2019,** *10* (7), 2101-2110.

174.   McGlynn, E., Electron paramagnetic resonance of transition ions, oxford classic texts in the physical sciences, by A. Abragam and B. Bleaney: Scope: textbook, monograph. Level: advanced undergraduate, postgraduate, early career researcher, researcher, specialist, scientist, engineers. Taylor & Francis: 2013.

175.   Blagg, R. J.; Ungur, L.; Tuna, F.; Speak, J.; Comar, P.; Collison, D.; Wernsdorfer, W.; McInnes, E. J.; Chibotaru, L. F.; Winpenny, R. E., Magnetic relaxation pathways in lanthanide single-molecule magnets. *Nature chemistry* **2013,** *5* (8), 673-678.

176.   Finn, C.; Orbach, R.; Wolf, W., Spin-lattice relaxation in cerium magnesium nitrate at liquid helium temperature: a new process. *Proceedings of the Physical Society (1958-1967)* **1961,** *77* (2), 261.

177.   Lucaccini, E.; Sorace, L.; Perfetti, M.; Costes, J.-P.; Sessoli, R., Beyond the anisotropy barrier: slow relaxation of the magnetization in both easy-axis and easy-plane Ln (trensal) complexes. *Chemical Communications* **2014,** *50* (14), 1648-1651.

178.   Wang, H.;   Liu, T.;   Wang, K.;   Duan, C.; Jiang, J., Tetrakis (phthalocyaninato) rare-earth-cadmium-rare-earth quadruple-decker sandwich smms: suppression of QTM by long-distance f – f interactions. *Chemistry – A European Journal* **2012,** *18* (25), 7691-7694.

179.   Frost, J. M.; Harriman, K. L. M.; Murugesu, M., The rise of 3-d single-ion magnets in molecular magnetism: towards materials from molecules? *Chemical Science* **2016,** *7* (4), 2470-2491.

180.   Escher, M. C.; Schattschneider, D., *Visions of symmetry*. Thames & Hudson: 2004.

181.   Grünbaum, B.; Shephard, G. C., *Tilings and patterns*. Courier Dover Publications: 1987.

182.   Écija, D.; Urgel, J. I.; Papageorgiou, A. C.; Joshi, S.; Auwärter, W.; Seitsonen, A. P.; Klyatskaya, S.; Ruben, M.; Fischer, S.; Vijayaraghavan, S., Five-vertex Archimedean surface tessellation by lanthanide-directed molecular self-assembly. *Proceedings of the National Academy of Sciences* **2013,** *110* (17), 6678-6681.

183.   Écija, D.; Urgel, J. I.; Papageorgiou, A. C.; Joshi, S.; Auwärter, W.; Seitsonen, A. P.; Klyatskaya, S.; Ruben, M.; Fischer, S.; Vijayaraghavan, S.; Reichert, J.; Barth, J. V., Five-vertex Archimedean surface tessellation by lanthanide-directed molecular self-assembly. *Proceedings of the National Academy of Sciences* **2013,** *110* (17), 6678-6681.

184.   Barth, J. V., Molecular architectonic on metal surfaces. *Annual Review of Physical Chemistry* **2007,** *58* (1), 375-407.

185.   Voigt, L.; Kubus, M.; Pedersen, K. S., Chemical engineering of quasicrystal approximants in lanthanide-based coordination solids. *Nature Communications* **2020,** *11* (1), 4705.

186.   Barth, J. V.; Costantini, G.; Kern, K., Engineering atomic and molecular nanostructures at surfaces. In *nanoscience and technology: a collection of reviews from Nature journals*, World Scientific: 2010; pp 67-75.

187.   Barth, J. V., Molecular architectonic on metal surfaces. *Annu. Rev. Phys. Chem.* **2007,** *58*, 375-407.

188.   Bartels, L., Tailoring molecular layers at metal surfaces. *Nature chemistry* **2010,** *2* (2), 87-95.

189.   Barth, J. V., Fresh perspectives for surface coordination chemistry. *Surface Science* **2009,** *603* (10-12), 1533-1541.

190.   Lin, N.; Stepanow, S.; Ruben, M.; Barth, J. V., Surface-confined supramolecular coordination chemistry. *Templates in Chemistry III* **2008**, 1-44.

191.   Schlickum, U.; Decker, R.; Klappenberger, F.; Zoppellaro, G.; Klyatskaya, S.; Ruben, M.; Silanes, I.; Arnau, A.; Kern, K.; Brune, H., Metal−organic honeycomb nanomeshes with tunable cavity size. *Nano letters* **2007,** *7* (12), 3813-3817.

192.   Marschall, M.; Reichert, J.; Weber-Bargioni, A.; Seufert, K.; Auwärter, W.; Klyatskaya, S.; Zoppellaro, G.; Ruben, M.; Barth, J. V., Random two-dimensional string networks based on divergent coordination assembly. *Nature Chemistry* **2010,** *2* (2), 131-137.

193.   Schlickum, U.; Klappenberger, F.; Decker, R.; Zoppellaro, G.; Klyatskaya, S.; Ruben, M.; Kern, K.; Brune, H.; Barth, J., Surface-confined metal−organic nanostructures from Co-directed assembly of linear terphenyl-dicarbonitrile linkers on Ag (111). *The Journal of Physical Chemistry C* **2010,** *114* (37), 15602-15606.

194.	Heim, D.; Seufert, K.; Auwärter, W.; Aurisicchio, C.; Fabbro, C.; Bonifazi, D.; Barth, J. V., Surface-assisted assembly of discrete porphyrin-based cyclic supramolecules. *Nano letters* **2010,** *10* (1), 122-128.

195.	Heim, D.; Ecija, D.; Seufert, K.; Auwarter, W.; Aurisicchio, C.; Fabbro, C.; Bonifazi, D.; Barth, J. V., Self-assembly of flexible one-dimensional coordination polymers on metal surfaces. *Journal of the American Chemical Society* **2010,** *132* (19), 6783-6790.

196.	Liu, J.; Lin, T.; Shi, Z.; Xia, F.; Dong, L.; Liu, P. N.; Lin, N., Structural transformation of two-dimensional metal–organic coordination networks driven by intrinsic in-plane compression. *Journal of the American Chemical Society* **2011,** *133* (46), 18760-18766.

197.	Lin, N.; Dmitriev, A.; Weckesser, J.; Barth, J. V.; Kern, K., Real-time single-molecule imaging of the formation and dynamics of coordination compounds. *Angewandte Chemie International Edition* **2002,** *41* (24), 4779-4783.

198.	Dmitriev, A.; Spillmann, H.; Lin, N.; Barth, J. V.; Kern, K., Modular assembly of two-dimensional metal–organic coordination networks at a metal surface. *Angewandte Chemie* **2003,** *115* (23), 2774-2777.

199.	Stepanow, S.; Lingenfelder, M.; Dmitriev, A.; Spillmann, H.; Delvigne, E.; Lin, N.; Deng, X.; Cai, C.; Barth, J. V.; Kern, K., Steering molecular organization and host–guest interactions using two-dimensional nanoporous coordination systems. *Nature materials* **2004,** *3* (4), 229-233.

200.	Urgel, J. I.; Ecija, D.; Auwärter, W.; Papageorgiou, A. C.; Seitsonen, A. P.; Vijayaraghavan, S.; Joshi, S.; Fischer, S.; Reichert, J.; Barth, J. V., Five-vertex lanthanide coordination on surfaces: a route to sophisticated nanoarchitectures and tessellations. *The Journal of Physical Chemistry C* **2014,** *118* (24), 12908-12915.

201.	Urgel, J. I.; Écija, D.; Lyu, G.; Zhang, R.; Palma, C.-A.; Auwärter, W.; Lin, N.; Barth, J. V., Quasicrystallinity expressed in two-dimensional coordination networks. *Nature Chemistry* **2016,** *8* (7), 657-662.

202.	Oppenheim, J. J.; Skorupskii, G.; Dincă, M., Aperiodic metal–organic frameworks. *Chemical Science* **2020,** *11* (41), 11094-11103.

203.	Deguchi, K.; Matsukawa, S.; Sato, N. K.; Hattori, T.; Ishida, K.; Takakura, H.; Ishimasa, T., Quantum critical state in a magnetic quasicrystal. *Nature Materials* **2012,** *11* (12), 1013-1016.

204.   Vardeny, Z. V.; Nahata, A.; Agrawal, A., Optics of photonic quasicrystals. *Nature Photonics* **2013,** *7* (3), 177-187.

205.   Harrison, A., First catch your hare: the design and synthesis of frustrated magnets. *Journal of Physics: Condensed Matter* **2004,** *16* (11), S553-S572.

206.   Ueda, K.; Dotera, T.; Gemma, T., Photonic band structure calculations of two-dimensional Archimedean tiling patterns. *Physical Review B* **2007,** *75* (19), 195122.

207.   Brian Moulton, J. L., Ranko Hajndl,Srikanth Hariharan, and Michael J. Zaworotko, Crystal engineering of a nanoscale kagom lattice. *Angew. Chem* **2002,** *114* (15), 2945.

208.   Chen, Q.; Bae, S. C.; Granick, S., Directed self-assembly of a colloidal kagome lattice. *Nature* **2011,** *469* (7330), 381-384.

209.   Tahara, K.; Furukawa, S.; Uji-i, H.; Uchino, T.; Ichikawa, T.; Zhang, J.; Mamdouh, W.; Sonoda, M.; De Schryver, F. C.; De Feyter, S.; Tobe, Y., Two-dimensional porous molecular networks of dehydrobenzo[12]annulene derivatives via alkyl chain interdigitation. *Journal of the American Chemical Society* **2006,** *128* (51), 16613-16625.

210.   Schlickum, U.; Decker, R.; Klappenberger, F.; Zoppellaro, G.; Klyatskaya, S.; Auwärter, W.; Neppl, S.; Kern, K.; Brune, H.; Ruben, M.; Barth, J. V., Chiral kagomé lattice from simple ditopic molecular bricks. *Journal of the American Chemical Society* **2008,** *130* (35), 11778-11782.

211.   Shi, Z.; Lin, N., Porphyrin-based two-dimensional coordination kagome lattice self-assembled on a Au(111) surface. *Journal of the American Chemical Society* **2009,** *131* (15), 5376-5377.

212.   Klappenberger, F.; Kühne, D.; Krenner, W.; Silanes, I.; Arnau, A.; García de Abajo, F. J.; Klyatskaya, S.; Ruben, M.; Barth, J. V., Dichotomous array of chiral quantum corrals by a self-assembled nanoporous kagomé network. *Nano Letters* **2009,** *9* (10), 3509-3514.

213.   Shi, Z.; Lin, N., Structural and chemical control in assembly of multicomponent metal−organic coordination networks on a surface. *Journal of the American Chemical Society* **2010,** *132* (31), 10756-10761.

214.   Lee, S.; Bluemle, M. J.; Bates, F. S., Discovery of a frank-kasper phase in sphere-forming block copolymer melts. *Science* **2010,** *330* (6002), 349-353.

215.   Carrington, A.; dos Santos-Veiga, J., Electron spin resonance spectra of nitrogen heterocyclic radical ions. *Molecular Physics* **1962,** *5* (1), 21-29.

216.   Denning, M. S.; Irwin, M.; Goicoechea, J. M., Synthesis and characterization of the 4,4′-bipyridyl dianion and radical monoanion. a structural study. *Inorganic Chemistry* **2008,** *47* (14), 6118-6120.

217.   Izod, K.; Liddle, S. T.; Clegg, W., A Convenient route to lanthanide triiodide thf solvates. crystal structures of $LnI_3(THF)_4$ [Ln = Pr] and $LnI_3(THF)_{3.5}$ [Ln = Nd, Gd, Y]. *Inorganic Chemistry* **2004,** *43* (1), 214-218.

218.   Heckmann, G.; Niemeyer, M., Synthesis and first structural characterization of lanthanide(ii) aryls: observation of a schlenk equilibrium in europium(ii) and ytterbium(ii) chemistry. *Journal of the American Chemical Society* **2000,** *122* (17), 4227-4228.

219.   Dabsamut, K.; Thienprasert, J.; Jungthawan, S.; Boonchun, A., Stacking stability of C_2N bilayer nanosheet. *Scientific Reports* **2019,** *9* (1), 6861.

220.   Heath, G. A.; Yellowlees, L. J.; Braterman, P. S., Ligand-ligand inter-valence charge-transfer absorption in reduced ruthenium(II) bipyridine complexes. *Chemical Physics Letters* **1982,** *92* (6), 646-648.

221.   Woodruff, D. N.; Winpenny, R. E.; Layfield, R. A., Lanthanide single-molecule magnets. *Chemical reviews* **2013,** *113* (7), 5110-5148.

222.   Huang, X. C.; Vieru, V.; Chibotaru, L. F.; Wernsdorfer, W.; Jiang, S. D.; Wang, X. Y., Determination of magnetic anisotropy in a multinuclear Tb^{III}-based single-molecule magnet. *Chemical Communications* **2015,** *51* (52), 10373-10376.

223.   Piquer, L. R.; Sañudo, E. C., Heterometallic 3d–4f single-molecule magnets. *Dalton Transactions* **2015,** *44* (19), 8771-8780.

224.   Jia, K.; Meng, X.; Wang, M.; Gou, X.; Wang, Y. X.; Xu, N.; Shi, W.; Cheng, P., Enhancing the energy barrier and hysteresis temperature in two benchtop-stable Ho(III) single-ion magnets. *Chemical Communications* **2021,** *57* (29), 3607-3610.

225.   Yamashita, A.; Watanabe, A.; Akine, S.; Nabeshima, T.; Nakano, M.; Yamamura, T.; Kajiwara, T., Wheel-shaped $Er^{III}Zn^{II}_3$ single-molecule magnet: a macrocyclic approach to designing magnetic anisotropy. *Angewandte Chemie* **2011,** *123* (17), 4102-4105.

226.	Ge, J. Y.; Qiu, Y. R.; Wang, H. Y.; Su, J.; Wang, P.; Chen, Z., Magnetic relaxation dynamics of a binuclear diluted Er(III)/Y(III) compound influenced by lattice solvent. *Chemistry–An Asian Journal* **2020,** *15* (19), 3013-3019.

227.	Singh, S. K.; Gupta, T.; Rajaraman, G., Magnetic anisotropy and mechanism of magnetic relaxation in Er(III) single-ion magnets. *Inorganic chemistry* **2014,** *53* (20), 10835-10845.

228.	Zhang, P.; Zhang, L.; Wang, C.; Xue, S.; Lin, S. Y.; Tang, J., Equatorially coordinated lanthanide single ion magnets. *Journal of the American Chemical Society* **2014,** *136* (12), 4484-4487.

229.	Petrosyants, S. P.; Babeshkin, K. A.; Gavrikov, A. V.; Ilyukhin, A. B.; Belova, E. V.; Efimov, N. N., Towards comparative investigation of Er- and Yb-based SMMs: The effect of the coordination environment configuration on the magnetic relaxation in the series of heteroleptic thiocyanate complexes. *Dalton Transactions* **2019,** *48* (33), 12644-12655.

230.	Ghosh, S.; Datta, S.; Friend, L.; Cardona-Serra, S.; Gaita-Ariño, A.; Coronado, E.; Hill, S., Multi-frequency EPR studies of a mononuclear holmium single-molecule magnet based on the polyoxometalate $[Ho^{III}(W_5O_{18})_2]^{9-}$. *Dalton Transactions* **2012,** *41* (44), 13697-13704.

231.	Norre, M. S.; Gao, C.; Dey, S.; Gupta, S. K.; Borah, A.; Murugavel, R.; Rajaraman, G.; Overgaard, J., High-pressure crystallographic and magnetic studies of pseudo-D_{5h} symmetric Dy(III) and Ho(III) single-molecule magnets. *Inorganic Chemistry* **2019,** *59* (1), 717-729.

232.	Forrester, P. R.; Patthey, F.; Fernandes, E.; Sblendorio, D. P.; Brune, H.; Natterer, F. D., Quantum state manipulation of single atom magnets using the hyperfine interaction. *Physical Review B* **2019,** *100* (18), 180405.

233.	Y. Ho, J.; Matsuura, T.; P. Santerre, J., The effect of fluorinated surface modifying macromolecules on the surface morphology of polyethersulfone membranes. *Journal of Biomaterials Science, Polymer Edition* **2000,** *11* (10), 1085-1104.

234.	Visinescu, D.; Jeon, I.-R.; Madalan, A. M.; Alexandru, M.-G.; Jurca, B.; Mathonière, C.; Clérac, R.; Andruh, M., Self-assembly of $[Cu^{II}Tb^{III}]^{3+}$ and $[W(CN)_8]^{3-}$ tectons: a case study of a mixture containing two complexes showing slow-relaxation of the magnetization. *Dalton Transactions* **2012,** *41* (44), 13578-13581.

235.   Katoh, K.;   Breedlove, B. K.; Yamashita, M., Symmetry of octa-coordination environment has a substantial influence on dinuclear Tb[III] triple-decker single-molecule magnets. *Chemical science* **2016,** *7* (7), 4329-4340.

236.   Pedersen, K. S.; Perlepe, P.; Aubrey, M. L.; Woodruff, D. N.; Reyes-Lillo, S. E.; Reinholdt, A.; Voigt, L.; Li, Z.; Borup, K.; Rouzières, M.; Samohvalov, D.; Wilhelm, F.; Rogalev, A.; Neaton, J. B.; Long, J. R.; Clérac, R., Formation of the layered conductive magnet $CrCl_2(pyrazine)_2$ through redox-active coordination chemistry. *Nature Chemistry* **2018,** *10* (10), 1056-1061.

237.   Kubus, M.; Voigt, L.; Pedersen, K. S., Pentagonal-bipyramidal acetonitrile complexes of the lanthanide(II) iodides. *Inorganic Chemistry Communications* **2020,** *114*, 107819.

238.   Newville, M.; Ravel, B.; Haskel, D.; Rehr, J.; Stern, E.; Yacoby, Y., Analysis of multiple-scattering XAFS data using theoretical standards. *Physica B: Condensed Matter* **1995,** *208*, 154-156.

239.   Koningsberger, D.; Mojet, B.; Van Dorssen, G.; Ramaker, D., XAFS spectroscopy; fundamental principles and data analysis. *Topics in catalysis* **2000,** *10* (3), 143-155.

240.   Berg, D. J.; Boncella, J. M.; Andersen, R. A., Preparation of coordination compounds of Cp*₂Yb with heterocyclic nitrogen bases: Examples of antiferromagnetic exchange coupling across bridging ligands. *Organometallics* **2002,** *21* (22), 4622-4631.

241.   Jiang, Y.; Oh, I.; Joo, S. H.; Buyukcakir, O.; Chen, X.; Lee, S. H.; Huang, M.; Seong, W. K.; Kwak, S. K.; Yoo, J.-W., Partial oxidation-induced electrical conductivity and paramagnetism in a Ni(II) tetraaza[14] annulene-linked metal organic framework. *Journal of the American Chemical Society* **2019,** *141* (42), 16884-16893.

242.   Zhong, H.; Ghorbani-Asl, M.; Ly, K. H.; Zhang, J.; Ge, J.; Wang, M.; Liao, Z.; Makarov, D.; Zschech, E.; Brunner, E., Synergistic electroreduction of carbon dioxide to carbon monoxide on bimetallic layered conjugated metal-organic frameworks. *Nature communications* **2020,** *11* (1), 1-10.

243.   Liu, Y.; Li, S.; Dai, L.; Li, J.; Lv, J.; Zhu, Z.; Yin, A.; Li, P.; Wang, B., The synthesis of hexaazatrinaphthylene‐based 2D conjugated copper metal‐organic framework for highly selective and stable electroreduction of CO_2 to methane. *Angewandte Chemie* **2021,** *133* (30), 16545-16551.

244.   Zhong, H.; Ly, K. H.; Wang, M.; Krupskaya, Y.; Han, X.; Zhang, J.; Zhang, J.; Kataev, V.; Büchner, B.; Weidinger, I. M., A phthalocyanine-based layered two-dimensional conjugated metal–organic framework as a highly efficient electrocatalyst for the oxygen reduction reaction. *Angewandte Chemie International Edition* **2019,** *58* (31), 10677-10682.

245.   Wu, Y.; Jiang, J.; Weng, Z.; Wang, M.; Broere, D. L.; Zhong, Y.; Brudvig, G. W.; Feng, Z.; Wang, H., Electroreduction of CO_2 catalyzed by a heterogenized Zn–porphyrin complex with a redox-innocent metal center. *ACS central science* **2017,** *3* (8), 847-852.

Paper 1

Magnetic Archimedean Tessellations in Metal−Organic Frameworks

Hua Chen, Laura Voigt, Mariusz Kubus, Dmytro Mihrin, Susanne Mossin, René W. Larsen, Søren Kegnæs, Stergios Piligkos, and Kasper S. Pedersen*, *Journal of the American Chemical Society*, **2021**, 143, 14041−14045.

Communication

Magnetic Archimedean Tessellations in Metal−Organic Frameworks

Hua Chen, Laura Voigt, Mariusz Kubus, Dmytro Mihrin, Susanne Mossin, René W. Larsen,
Søren Kegnæs, Stergios Piligkos, and Kasper S. Pedersen*

Cite This: *J. Am. Chem. Soc.* 2021, 143, 14041−14045

Read Online

ACCESS | ⬛ Metrics & More | ⬛ Article Recommendations | ⬛ Supporting Information

ABSTRACT: The self-assembly of lanthanide ions with ditopic organic spacers results in the formation of complex tiling patterns that mimic the structural motifs of quasi-periodic 2D materials. The linking of $trans$-$\{LnI_2\}^+$ nodes (Ln = Gd, Dy) by both closed-shell and anion radicals of 4,4′-bipyridine affords rare examples of Archimedean tessellations in a metal−organic framework. We furthermore demonstrate the occurrence of sizable magnetic exchange interactions and slow relaxation of magnetization behavior in a complex tessellation pattern. The implementation of Archimedean tessellations in lanthanide(III) coordination solids couriers a strategy to design elusive quasi-periodic metal−organic frameworks with inimitable magnetic properties.

The design of complex and aperiodic two-dimensional tessellations in molecule-based materials constitutes a novel route to harvest physical properties, for instance, photonic, electronic, magnetic, and phononic characteristics, which are expected to be unparalleled compared to their periodic counterparts.[1−3] However, applications are elusive due to the severe scarcity of materials exhibiting the desired structural motifs. The two-dimensional dodecagonal quasicrystalline phase (Figure 1a, ddQC) is well-known in both hard

Figure 1. (a) An example of a random tiling of a ddQC, (b) the semiregular elongated triangular tiling, and (c) the semiregular snub square tiling.
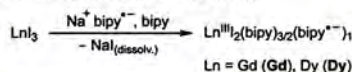
and soft materials as well as in supramolecular networks.[4−6] In these system, the tessellation of triangles and squares, at a ratio of $4/\sqrt{3} \approx 2.3$, leads to the disappearance of periodicity and the formation of local 12-fold rotational symmetry. Generally, quasicrystals are found in the vicinity of structurally related, periodic structures, and the ddQCs often co-occur with the periodic Archimedean tessellations (ATs, Figure 1b,c), which are termed quasicrystal approximants.[7] The sole example of a quasicrystal phase found in a metal−organic network structure

was realized as single-atom layers by coevaporating Eu atoms and organic linkers.[8] The construction of 5- and 6-fold nodes is critical for the realization of such structures and necessitates confining five or six chemical bonds to the plane. This requirement precludes the use of most transition metal ions as nodes but may be met by larger metal ions as those found in the f-block. In these fragile materials, the exact chemical nature, such as the oxidation state of the 4f ion nodes, remains unknown. In the more robust, bulk coordination networks and metal−organic frameworks (MOFs), quasicrystals are elusive.[8] This may partly be related to the complications in their crystallographic identification and partly due to the lack of structures that bear the potential to express quasicrystallinity. The elongated triangular and snub square ATs (Figure 1b,c) each possess a triangle-to-square ratio of 2 and are desired structures in the quest for ddQCs, but are almost nonexistent in MOFs.

Taking advantage of the common pentagonal-bipyramidal coordination motif of the uranyl ion, $trans$-$\{UO_2\}^{2+}$, Smetana et al. reported the first example of a snub square tiling in a metal−organic bulk material.[9] We recently reported the utilization of $trans$-$\{Yb^{II}I_2\}$ nodes as five-vertex building units to form the triangular elongated tiling in $Yb^{II}I_2(bipy)_{5/2}$ (bipy = 4,4′-bipyridine).[10] The lanthanide ions are particularly relevant for the realization of both ATs and ddQC phases as the coordinative plasticity allows for their incorporation in a variety of local coordination geometries. Furthermore, their weak interactions with ligands are commensurate with the weak interactions typically intrinsic to aperiodic structures.[8] The construction of the $YbI_2(bipy)_{5/2}$ framework necessitated the introduction of divalent lanthanide units, whose prepon-

derance in chemistry is dwarfed by the trivalent ones. To circumvent this problem, we herein demonstrate a novel strategy to realize magnetic ATs incorporating trivalent lanthanide ions.
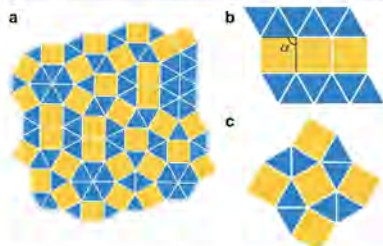
The reaction of metallic sodium with bipy is known to generate the anion radical bipy$^{\bullet-}$;[11] however, only a single crystalline compound is known to incorporate this chemical species, Na$^+$(ethane-1,2-diamine)(bipy$^{\bullet-}$).[12] The reaction of sodium with a 2.5-fold mol equiv of bipy in CH$_3$CN affords a dark-blue solution. The X-band EPR spectrum of the frozen solution yields a single narrow resonance at g = 2.00 (Figure S1), compatible with the formation of an organic radical.[12] The addition of solid GdI$_3$ to the bipy$^{\bullet-}$/bipy solution (Scheme 1)

Scheme 1. Synthetic Route to Gd and Dy

$$LnI_3 \xrightarrow[- NaI_{(dissolv.)}]{Na^+ \; bipy^{\bullet-}, \; bipy} Ln^{III}I_2(bipy)_{3/2}(bipy^{\bullet-})_1$$

Ln = Gd (**Gd**), Dy (**Dy**)

results in an immediate formation of a dark-blue powder which exhibits a broad EPR signal (Figure S2). The elemental analyses of C, H, N, Gd, I, and Na indicate a formulation of GdI$_2$(bipy)$_{5/2}$·CH$_3$CN and no presence of Na$^+$ (cf. the Supporting Information). Layering of the bipy$^{\bullet-}$/bipy solution onto CH$_3$CN-covered GdI$_3$ affords block-like, dark-blue crystals of **Gd** suitable for single-crystal X-ray diffraction. **Gd** crystallizes in the tetragonal $I4_122$ space group and features an ideal snub square tessellation of GdI$_2$(bipy)$_{5/2}$·xCH$_3$CN (Figures 1c and 2a). The coordination geometries of the two crystallographically independent Gd centers are almost identical. The Gd–I bond lengths of 3.0429(6)–3.055(2) Å are slightly longer than those found in *trans*-[Gd^{III}I$_2$(thf)$_5$]$^+$ of 3.00 Å,[13] albeit significantly shorter than the Eu–I bonds found in *trans*-[Eu^{II}I$_2$(thf)$_5$] of 3.22–3.24 Å,[14] corroborating the presence of Gd(III) and not the extremely rare Gd(II), in **Gd**.[15] The N–Gd–N angles are in the range 67.9(2)°–75.5(3)° and together with the I–Gd–I linearity (179.25(3)°, 177.86(4)°) reflect the close proximity of the local coordination environment to D_{5h} symmetry. The presence of Gd(III) necessitates one bipy$^{\bullet-}$ radical ligand per GdI$_3$(bipy)$_{5/2}$ formula unit. Goicoechea and co-workers have shown that the interpyridinic bond in bipy shortens by ∼4% upon one-electron reduction.[12] In **Gd**, the two crystallographically independent Gd centers are each surrounded by three bipy$^{0/\bullet-}$ ligands with longer C–C bond lengths of 1.48(2)–1.51(2) Å and two bipy$^{0/\bullet-}$ ligands with short C–C bond lengths of 1.45(2) Å corresponding to a reduction of ∼4%. Interestingly, the anticipated localized bipy$^{\bullet-}$ ligands span the edges of the triangles in only one direction of the plane, which leads to the formation of {Gd^{III}$_4$(bipy$^{\bullet-}$)$_4$} rhombi (Figure S3). The presence of mixed valency in the bipy$^{0/\bullet-}$ scaffold could be expected to lead to strong intervalence charge transfer (IVCT) transitions in the mid- or near-infrared spectrum as, for example, observed in transition metal complexes of mixed-valent 2,2′-bipyridine$^{0/\bullet-}$.[16] However, no IVCT bands could be observed in **Gd** (Figure S6) which may be attributed to the weakly covalent nature of metal–ligand bonds and the localization of the unpaired electron. Notably, in each crystallization vial, a few needle-shaped dark-blue crystals of **Gd′** were systematically obtained. The structural analysis of **Gd′** revealed an
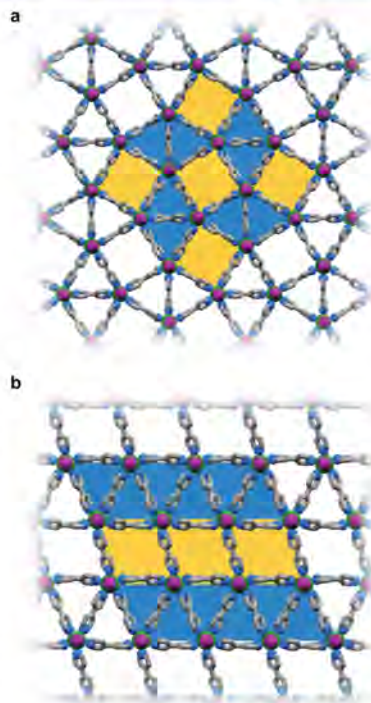
Figure 2. (a) Single-crystal X-ray structure of **Gd**. (b) Single-crystal structure of the trace impurity phase **Gd′**. Color codes: Gd, green; I, purple; N, blue; C, gray. H atoms and cocrystallized CH$_3$CN molecules have been omitted.

identical chemical composition of GdI$_2$(bipy)$_{5/2}$·xCH$_3$CN, but **Gd′** crystallizes in the triclinic P$\bar{1}$ space group and resembles an elongated triangular tiling (Figure 2b) similar to the previously reported YbI$_2$(bipy)$_{5/2}$ structure. However, contrary to YbI$_2$(bipy)$_{5/2}$, the tilting angle, α (Figure 1b), departs significantly from 90° and amounts to 101°. Thus, the **Gd′** could be considered as approaching defect 6-fold nodes, corresponding to α = 120°. Similarly to **Gd**, two-fifths and three-fifths of the bipy display short (1.44(2) Å) and long (1.51(1)–1.53(2) Å) interpyridinic C–C bonds, respectively, echoing the existence of Gd(III) and both bipy and bipy$^{\bullet-}$. Use of DyI$_3$ reveals an identical behavior and yields DyI$_2$(bipy)$_{5/2}$·xCH$_3$CN (**Dy**), which is isostructural to **Gd**. Notably, no traces of an elongated triangular tessellation phase could be observed for **Dy**.

111

The room temperature value of the magnetic susceptibility–temperature product, χT, of **Gd** amounts to 8.6 cm^3 K mol^{-1}, close to the value expected for an uncorrelated pair of a Gd(III) ion (4f^7) and an organic radical of 8.3 cm^3 mol^{-1}. The magnetic characterization was performed on polycrystalline specimens for which the presence of any traces of **Gd′** was unobserved (Figure S5) and thus will not be detectable by bulk magnetometry. The χT product decreases only slightly by cooling, reflecting the relatively weak Gd^{III}–bipy$^{\bullet-}$ superexchange interactions. Similarly, the field dependence of the magnetization, M vs $\mu_0 H$, reveals that M saturates at low temperature at 8.0 μ_B at 9 T, as expected for one Gd^{III} and one bipy$^{\bullet-}$ per formula unit. The structural analyses revealed the presence of {Gd$^{III}_4$(bipy$^{\bullet-}$)$_4$} rhombi. Thus, the magnetization data were modeled by using the spin-Hamiltonian (eq 1) for an eight-membered ring of alternating Gd(III) ions and bipy$^{\bullet-}$ radicals:

$$\hat{H} = g\mu_B\mu_0 H \sum_i \hat{S}_i + J(\hat{S}_{Gd1}\hat{S}_{rad1} + \hat{S}_{Gd2}\hat{S}_{rad1} + \hat{S}_{Gd2}\hat{S}_{rad2}$$
$$+ \hat{S}_{Gd3}\hat{S}_{rad2} + \hat{S}_{Gd3}\hat{S}_{rad3} + \hat{S}_{Gd4}\hat{S}_{rad3} + \hat{S}_{Gd4}\hat{S}_{rad4}$$
$$+ \hat{S}_{Gd1}\hat{S}_{rad4}) \tag{1}$$

where $g = 2$ is the isotropic g factor for both Gd^{III} and the radical spins, μ_B is the Bohr magneton, $\mu_0 H$ is the magnetic field, S is a spin operator indexed for each Gd^{III} and bipy$^{\bullet-}$, and J is the coupling constant. The dimension of the matrix representation of eq 1 for **Gd** is 65536, which is impractical with respect to standard numerical full matric diagonalization approaches. Thus, for the quantitative interpretation of the magnetic properties of **Gd**, we used home-written software (ITO-MAGFIT)[17] that makes use of irreducible tensor operator algebra[18] to block-diagonalize the spin-Hamiltonian and the Levenberg–Marquardt algorithm[17] to fit the magnetization data. The χT product and the M vs $\mu_0 H$ data of **Gd** were simultaneously fitted to the spin-Hamiltonian (eq 1). This resulted to the best-fit $J/hc = 0.073(4)$ cm^{-1} (Figure 3 and Figure S7). Under these conditions, the spin ground state is an $S \simeq 12$ (Figure S8), separated from the first excited state, a degenerate doublet of $S = 11$ states, by only 0.16 cm^{-1} at zero magnetic field. This vanishing value of J is noteworthy
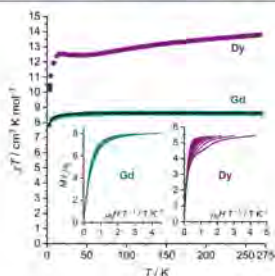
although not uncommon for Gd(III)–radical complexes.[20] For **Dy**, the room temperature χT product leans at 13.8 cm^3 K mol^{-1}, which is slightly lower than the expected value for a Dy^{3+} ion ($C = 14.2$ cm^3 K mol^{-1}) and a bipy$^{\bullet-}$ ligand. The χT product decreases slightly at lower temperatures due to depopulation of excited ligand field states. Below ca. 15 K, the χT product drops abruptly, which may be ascribed to the concerted effects of magnetic superexchange interactions, dipolar interactions, and the ligand field. The M vs $\mu_0 HH$ data (Figure 3 (inset) and Figure 4) reveal a clear step at ca. 3
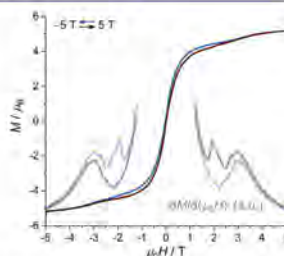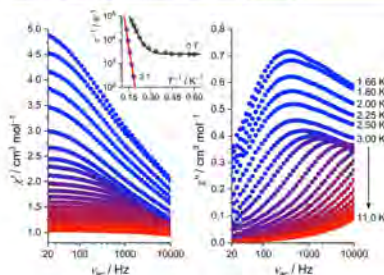

Figure 4. M vs $\mu_0 H$ data obtained at $T = 2.1$ K (sweeping rate of 200 Oe s^{-1}) and the first derivative, dM/d($\mu_0 H$).

T. Notably, a similar step feature was previously observed in a Dy(III)–radical chain system but absent in the isostructural Gd(III) system and attributed to the presence of significant exchange interactions in the Dy(III) system.[21,22] At fields smaller than ~3 T, the M vs $\mu_0 H$ data show the opening of a small hysteresis gap that collapses again when zero field is approached (Figure 4 and Figure S9). Several Dy^{3+} single-molecule magnets (SMMs) with approximately local D_{5h} symmetry have been shown to exhibit exceedingly large energy barriers to magnetization reversal exceeding 1000 cm^{-1}, and Dy(III)–radical complexes commonly display wide magnetization hysteresis loops.[23-29] Alternating current (ac) susceptibility measurements of **Dy** reveal the existence of slow relaxation of magnetization (Figure 5). The temperature dependence of the spin–lattice relaxation rate (Figure 5) was modeled a sum of terms governing the temperature-independent quantum tunneling of the magnetization (QTM) and the two-phonon Orbach process:

$$\tau(T)^{-1} = \tau_{QTM}^{-1} + \tau_0^{-1}e^{-\Delta/k_B T} \tag{2}$$

The τ vs T data are well described by $\tau_{QTM} = 0.4$ μs and $\Delta/hc = 22$ cm^{-1} ($\tau_0^{-1} = 1.2 \times 10^{-7}$ s; Figure 5). The application of a sizable, static dc magnetic field of 3 T breaks the tunneling pathway (Figures S10–S12), and the τ vs T data can be modeled by the inclusion of the Orbach process only ($\Delta/hc = 63$ cm^{-1} and $\tau_0 = 3.5 \times 10^{-10}$ s; Figure 5, red trace). This Δ is dwarfed by those of other D_{5h} symmetric SMMs, but otherwise typical of lanthanide-based SMMs.[23-25] The high-performance systems all display the presence of strongly donating ligands in the axial positions, which contrast the weak-field iodide ligands in **Dy** but provide an attractive pathway to analogous tessellations with improved SMM characteristics.

Figure 3. Temperature dependence of the χT product for polycrystalline **Gd** and **Dy** ($\mu_0 H = 1000$ Oe). The black line is the best fit as described in the main text. The insets show the magnetization, M, plotted against $\mu_0 HT^{-1}$.

112

Figure 5. In-phase (χ', left) and out-of-phase (χ'', right) ac susceptibility data for polycrystalline **Dy** obtained at selected temperatures and in the absence of a static (dc) magnetic field. Inset: temperature dependence of the paramagnetic relaxation rate, τ^{-1}, vs temperature. The solid lines are simulations as described in the main text.

The isolation of ddQCs and Archimedean tessellations of lanthanide metal–organic networks on metallic surfaces was attributed to significant interactions with the substrate that enforce planarization of the material.[8] Indeed, the equatorial linking of the kinetically labile trans-$\{LnI_2\}^+$ units may be considered as an analogue of the theoretical scenario of soft, isotropic particles moving in 2D that has been utilized to explain the formation of ddQCs.[30,31] Herein, we have demonstrated the possibility to construct chemically well-defined Archimedean tessellations of the trivalent lanthanide ions in MOF structures as exemplified by **Gd**, **Gd′**, and **Dy**. The tweaking of these systems toward their quasicrystalline variants necessitates the inclusion of local 6-fold (D_{6h} symmetric) nodes (Figure 1a), which, despite the large ionic radii, are uncommon for lanthanide ions.[32] The structure of **Gd′**, although not yet isolable as a pure bulk material, is remarkable as it gives a prospect on how to introduce the triangle-rich regular triangular motif without the highly uncommon coordination of six donor atoms in the equatorial plane, necessary to form ddQCs. While previous reports have shown the viability of lanthanide atoms to act as nodes in 2D ATs and ddQCs on surfaces,[8,33,34] the strategy presented herein constitutes the first generalizable approach to bulk MOF materials possessing periodic, aperiodic, and fractal geometries.

■ ASSOCIATED CONTENT

◉ Supporting Information

The Supporting Information is available free of charge at https://pubs.acs.org/doi/10.1021/jacs.1c05057.

> Materials and methods, experimental procedures, EPR spectroscopy, X-ray single-crystal and powder diffraction data and parameters, mid-IR/near-IR spectroscopy, and magnetometry (PDF)

Accession Codes

CCDC 2064814–2064816 contain the supplementary crystallographic data for this paper. These data can be obtained free of charge via www.ccdc.cam.ac.uk/data_request/cif, or by emailing data_request@ccdc.cam.ac.uk, or by contacting The Cambridge Crystallographic Data Centre, 12 Union Road, Cambridge CB2 1EZ, UK; fax: +44 1223 336033.

■ AUTHOR INFORMATION

Corresponding Author

Kasper S. Pedersen — *Department of Chemistry, Technical University of Denmark, DK-2800 Kgs. Lyngby, Denmark;* ◉ orcid.org/0000-0002-4381-4544; Email: kastp@kemi.dtu.dk

Authors

Hua Chen — *Department of Chemistry, Technical University of Denmark, DK-2800 Kgs. Lyngby, Denmark*
Laura Voigt — *Department of Chemistry, Technical University of Denmark, DK-2800 Kgs. Lyngby, Denmark*
Mariusz Kubus — *Department of Chemistry, Technical University of Denmark, DK-2800 Kgs. Lyngby, Denmark*
Dmytro Mihrin — *Department of Chemistry, Technical University of Denmark, DK-2800 Kgs. Lyngby, Denmark*
Susanne Mossin — *Department of Chemistry, Technical University of Denmark, DK-2800 Kgs. Lyngby, Denmark;* ◉ orcid.org/0000-0001-7763-9660
René W. Larsen — *Department of Chemistry, Technical University of Denmark, DK-2800 Kgs. Lyngby, Denmark;* ◉ orcid.org/0000-0003-2983-6795
Søren Kegnæs — *Department of Chemistry, Technical University of Denmark, DK-2800 Kgs. Lyngby, Denmark;* ◉ orcid.org/0000-0002-6933-6931
Stergios Piligkos — *Department of Chemistry, University of Copenhagen, DK-2100 Copenhagen, Denmark;* ◉ orcid.org/0000-0002-4011-6476

Complete contact information is available at:
https://pubs.acs.org/10.1021/jacs.1c05057

Notes

The authors declare no competing financial interest.

■ REFERENCES

(1) Oppenheim, J. J.; Skorupskii, G.; Dincă, M. Aperiodic metal-organic frameworks. *Chem. Sci.* **2020**, *11*, 11094–11103.
(2) Deguchi, K.; Matsukawa, S.; Sato, N. K.; Hattori, T.; Ishida, K.; Takakura, H.; Ishimasa, T. Quantum critical state in a magnetic quasicrystal. *Nat. Mater.* **2012**, *11*, 1013–1016.
(3) Vardeny, Z. V.; Nahata, A.; Agrawal, A. Optics of photonic quasicrystals. *Nat. Photonics* **2013**, *7*, 177–184.
(4) Kormoš, L.; Procházka, P.; Makoveev, A. O.; Čechal, J. Complex k-uniform tilings by a simple bitopic precursor self-assembled on Ag(001) surface. *Nat. Commun.* **2020**, *11*, 1856.
(5) Zeng, X.; Ungar, G.; Liu, Y.; Percec, V.; Dulcey, A. E.; Hobbs, J. K. Supramolecular dendritic liquid quasicrystals. *Nature* **2004**, *428*, 157–160.

113

(6) Lee, S.; Bluemle, M. J.; Bates, F. S. Discovery of a Frank-Kasper σ phase in sphere-forming block copolymer melts. *Science* 2010, 330, 349−353.

(7) Dotera, T. Toward the discovery of new soft quasicrystals: From a numerical study viewpoint. *J. Polym. Sci., Part B: Polym. Phys.* 2012, 50, 155−167.

(8) Urgel, J. I.; Écija, D.; Lyu, G.; Zhang, R.; Palma, C. A.; Auwärter, W.; Lin, N.; Barth, J. V. Quasicrystallinity expressed in two-dimensional coordination networks. *Nat. Chem.* 2016, 8, 657−662.

(9) Smetana, V.; Kelley, S. P.; Mudring, A.; Rogers, R. D. A fivefold UO2²⁺ node is a path to dodecagonal quasicrystal approximants in coordination polymers. *Sci. Adv.* 2020, 6, No. eaay7685.

(10) Voigt, L.; Kubus, M.; Pedersen, K. S. Chemical engineering of quasicrystal approximants in lanthanide-based coordination solids. *Nat. Commun.* 2020, 11, 4705.

(11) Cartington, A.; dos Santos-Veiga, J. Electron spin resonance spectra of nitrogen heterocyclic radical ions. *Mol. Phys.* 1962, 5, 21−29.

(12) Denning, M. S.; Irwin, M.; Goicoechea, J. M. Synthesis and characterization of the 4,4′-bipyridyl dianion and radical monoanion. A structural study. *Inorg. Chem.* 2008, 47, 6118−6120.

(13) Izod, K.; Liddle, S. T.; Clegg, W. A Convenient Route to Lanthanide Triiodide THF Solvates. Crystal Structures of LnI₃(THF)₄ [Ln = Pr] and LnI₃(THF)₃.₅ [Ln = Nd, Gd, Y]. *Inorg. Chem.* 2004, 43, 214−218.

(14) Heckmann, G.; Niemeyer, M. Synthesis and first structural characterization of lanthanide(II) aryls: Observation of a Schlenk equilibrium in europium(II) and ytterbium(II) chemistry. *J. Am. Chem. Soc.* 2000, 122, 4227−4228.

(15) Macdonald, M. R.; Bates, J. E.; Ziller, J. W.; Furche, F.; Evans, W. J. Completing the series of + 2 ions for the lanthanide elements: Synthesis of molecular complexes of Pr²⁺, Gd²⁺, Tb²⁺, and La²⁺. *J. Am. Chem. Soc.* 2013, 135, 9857−9868.

(16) Heath, G. A.; Yellowlees, L. J.; Braterman, P. S. Ligand-ligand inter-valence charge-transfer absorption in reduced ruthenium(II) bipyridine complexes. *Chem. Phys. Lett.* 1982, 92, 646−648.

(17) Hooper, T. N.; Schnack, J.; Piligkos, S.; Evangelisti, M.; Brechin, E. K. The importance of being exchanged: [Gd⁽ᴵᴵᴵ⁾₄M⁽ᴵᴵ⁾₆(OH)₈(1.)₄(O₂CR)₆]⁴⁺ clusters for magnetic refrigeration. *Angew. Chem., Int. Ed.* 2012, 51, 4633−4636.

(18) Bencini, A.; Gatteschi, D. *Electron Paramagnetic Resonance of Exchange Coupled Systems*; Springer: Berlin, 1990; pp 86−91.

(19) Press, W. H.; Teukolsky, S. A.; Vetterling, W. T.; Flannery, B. P. *Numerical Recipes in C: The Art of Scientific Computing*, 2nd ed.; Cambridge University Press: Cambridge, 1992; pp 683−688.

(20) Demir, S.; Jeon, I.-R.; Long, J. R.; Harris, T. D. Radical ligand-containing single-molecule magnets. *Coord. Chem. Rev.* 2015, 289−290, 149−176.

(21) Bogani, L.; Sangregorio, C.; Sessoli, R.; Gatteschi, D. Molecular engineering for single-chain-magnet behavior in a one-dimensional dysprosium-nitronyl nitroxide compound. *Angew. Chem., Int. Ed.* 2005, 44, 5817−5821.

(22) Bernot, K.; Bogani, L.; Caneschi, A.; Gatteschi, D.; Sessoli, R. A family of rare-earth-based single chain magnets: Playing with anisotropy. *J. Am. Chem. Soc.* 2006, 128, 7947−7956.

(23) Ding, Y. S.; Chilton, N. F.; Winpenny, R. E. P.; Zheng, Y. Z. On Approaching the Limit of Molecular Magnetic Anisotropy: A Near-Perfect Pentagonal Bipyramidal Dysprosium(III) Single-Molecule Magnet. *Angew. Chem., Int. Ed.* 2016, 55, 16071−16074.

(24) Ding, Y. S.; Yu, K. X.; Reta, D.; Ortu, F.; Winpenny, R. E. P.; Zheng, Y. Z.; Chilton, N. F. Field- and temperature-dependent quantum tunnelling of the magnetisation in a large barrier single-molecule magnet. *Nat. Commun.* 2018, 9, 3134.

(25) Yu, K. X.; Kragskow, J. G. C.; Ding, Y. S.; Zhai, Y. Q.; Reta, D.; Chilton, N. F.; Zheng, Y. Z. Enhancing Magnetic Hysteresis in Single-Molecule Magnets by Ligand Functionalization. *Chem.* 2020, 6, 1777−1793.

(26) Demir, S.; Gonzalez, M. I.; Darago, L. E.; Evans, W. J.; Long, J. R. Giant coercivity and high magnetic blocking temperatures for N₂³⁻

radical-bridged dilanthanide complexes upon ligand dissociation. *Nat. Commun.* 2017, 8, 1−9.

(27) Rinehart, J. D.; Fang, M.; Evans, W. J.; Long, J. R. Strong exchange and magnetic blocking in N₂³⁻ radical-bridged lanthanide complexes. *Nat. Chem.* 2011, 3, 538−542.

(28) Rinehart, J. D.; Fang, M.; Evans, W. J.; Long, J. R. A N₂³⁻ radical-bridged terbium complex exhibiting magnetic hysteresis at 14 K. *J. Am. Chem. Soc.* 2011, 133, 14236−14239.

(29) Gould, C. A.; Darago, L. E.; Gonzalez, M. I.; Demir, S.; Long, J. R. A Trinuclear Radical-Bridged Lanthanide Single-Molecule Magnet. *Angew. Chem., Int. Ed.* 2017, 56, 10103−10107.

(30) Barkan, K.; Engel, M.; Lifshitz, R. Controlled self-assembly of periodic and aperiodic cluster crystals. *Phys. Rev. Lett.* 2014, 113, 1−5.

(31) Keys, A. S.; Glotzer, S. C. How do quasicrystals grow? *Phys. Rev. Lett.* 2007, 99, 1−4.

(32) Canaj, A. B.; Dey, S.; Martí, E. R.; Wilson, C.; Rajaraman, G.; Murrie, M. Insight into D₆ₕ Symmetry: Targeting Strong Axiality in Stable Dysprosium(III) Hexagonal Bipyramidal Single-Ion Magnets. *Angew. Chem.* 2019, 131, 14284−14289.

(33) Écija, D.; Urgel, J. I.; Papageorgiou, A. C.; Joshi, S.; Auwärter, W.; Seitsonen, A. P.; Klyatskaya, S.; Ruben, M.; Fischer, S.; Vijayaraghavan, S.; Reichert, J.; Barth, J. V. Five-vertex Archimedean surface tessellation by lanthanide-directed molecular self-assembly. *Proc. Natl. Acad. Sci. U. S. A.* 2013, 110, 6678−6681.

(34) Urgel, J. I.; Écija, D.; Auwärter, W.; Papageorgiou, A. C.; Seitsonen, A. P.; Vijayaraghavan, S.; Joshi, S.; Fischer, S.; Reichert, J.; Barth, J. V. Five-vertex Lanthanide coordination on surfaces: A route to sophisticated nanoarchitectures and tessellations. *J. Phys. Chem. C* 2014, 118, 12908−12915.

114

Supporting Information

Magnetic Archimedean Tessellations in Metal-Organic Frameworks

Hua Chen,[†] Laura Voigt,[†] Mariusz Kubus,[†] Dmytro Mihrin,[†] Susanne Mossin,[†] René Wugt Larsen,[†] Søren Kegnæs,[†] Stergios Piligkos,[‡] Kasper S. Pedersen[†]

[†] Department of Chemistry, Technical University of Denmark, Kemitorvet, Building 207, DK-2800 Kgs. Lyngby, Denmark

[‡] Department of Chemistry, University of Copenhagen, DK-2100 Copenhagen, Denmark

Materials and Methods

All procedures were carried out in an InertLab glovebox under a dry Ar atmosphere. Elemental analysis was performed by the Mikroanalytisches Laboratorium Kolbe (Oberhausen, Germany). GdI_3 (99.99%) and DyI_3 (99.99%) were supplied by Alfa Aesar, and sodium and 4,4′-bipyridine (bipy; 98%) were supplied by Sigma-Aldrich. All reagents were used as received. Dry and oxygen-free solvents were obtained from a Puresolv MD 7 solvent purification system.

Synthesis

Gd: Powdered GdI_3 (135 mg, 250 µmol) and acetonitrile (14 mL) were stirred vigorously for 30 min. An acetonitrile solution (7 mL) of 4,4′-bipyridine (195 mg, 1.25 mmol) and sodium metal (5.8 mg, 250 µmol) was added dropwise to the GdI_3 suspension with stirring. A dark blue microcrystalline powder formed immediately. The mixture was left stirring for 10 min. The solid material isolated by suction filtration and washed with cold acetonitrile (–20 °C; 2 ×10 mL). Yield: 90 mg (45%). Anal. calcd. (found) for $C_{27}H_{23}GdI_2N_6$ (corresponding to $GdI_2(bipy)_{5/2}·CH_3CN$): C, 38.5 (38.2); H, 2.73 (2.81); N, 9.98 (9.91); I, 30.2 (29.7); Gd, 18.7 (18.3). Dark-blue single-crystals suitable for single-crystal X-ray diffractometry were obtained by slow diffusion. Powdered GdI_3 (135 mg, 250 µmol) was placed at the bottom of a glass test tube (160 ×16 mm) and carefully covered by acetonitrile (14 mL). The $Na^+(bipy^{•-})$/bipy solution (prepared as above) was gently layered on the top and the covered test tube was kept in the fridge (–20 °C) for 14 days. **Gd′** formed as a trace byproduct phase. **Dy**: The synthesis of **Dy** is identical to that of **Gd** but employs DyI_3. Single-crystals of **Dy** are grown similarly to **Gd**. Yield: 86 mg (43%). Anal. calcd. (found) for $C_{27}H_{23}DyI_2N_6$ (corresponding to $DyI_2(bipy)_{5/2}·CH_3CN$): C, 38.2 (38.1); H, 2.73 (2.76); N, 9.91 (9.87); I, 29.9 (29.9); Dy, 19.2 (19.3).

EPR spectroscopy

EPR spectra of both solid samples and frozen solutions were obtained at 77 K on a Bruker EMX X-band EPR spectrometer (rectangular cavity ST4102) fitted with a small Dewar for liquid nitrogen. The experimental parameters for the frozen solution of a freshly made solution of $Na^+(bipy^{•-})$ were: Microwave frequency 9.52 GHz, power 0.42 mW, time constant 20 ms, field interval 338.5–340.5 mT, modulation frequency 100 kHz, amplitude 1.0 G. The observed line is very intense (Fig. S1) and narrow and can be simulated with a g-value of 2.0045 and a Lorentzian line shape (line width 0.15 mT). The EPR signal of **Gd** (Fig. S2) is very broad and spans the field

interval from 0–0.65 T. The parameters used for the solid sample were microwave frequency 9.52 GHz, power 6.6 mW, time constant 20 ms, field interval 42–642 mT, modulation frequency 100 kHz, amplitude 5 G.

X-ray diffraction

Single-crystals of **Gd**, **Gd′**, and **Dy** were immersed in polybutene oil (Aldrich, >90%) and mounted on a nylon loop, which was attached to a SuperNova Dual Source CCD-diffractometer. Data were collected using Cu Kα (λ = 1.5406 Å) radiation at 100(1) or 120(1) K. The structures were solved in Olex2[1] using the structure solution program olex2.solve 1.3[2] for **Gd**, **Dy**, and SHELXT 2018/2[3] for **Gd′** and subsequently refined with the SHELXL[4] refinement package using least squares minimization. All non-hydrogen atoms were refined anisotropically. For both **Gd** and **Dy**, the structure was refined as an inversion twin with a BASF parameter of 0.501(7) and 0.44(1) respectively. In the **Dy** structure due to bipy disorder, the DFIX command was used to restrain distances in the aromatic ring with the N6 atom, and the SIMU and DELU commands were used to restraint the thermal parameters. Additionally, it was necessary to enforce ISOR restraints on the ADPs for the C25 atom and the equality constraints EADP on the ADPs of C24, C24A atom pair in the ring. Furthermore, the AFIX 66 command was used to maintain the geometry of the aromatic ring with the N4 atom. The restraint command SIMU was applied to the disordered C25, C24, and C24A atoms of the bipy molecule in the **Gd** structure. The geometry of the acetonitrile molecules in **Gd** and **Dy** was restrained using the DFIX, SIMU, and RIGU instruction (molecules imported from FragmentDB[5,6]). Additionally, ADPs of atoms in the acetonitrile molecules with N8, N10, N12, N13, N15 in the Dy structure and N11, N13, and N14 in the Gd structure were restrained to behave isotropically (ISOR).

The powder X-ray diffraction patterns were collected using Cu Kα (λ = 1.54056 Å) radiation in the range 6° < 2θ < 32°, with a 2θ step size of 0.01° using the SuperNova Dual Source CCD diffractometer. The diffraction pattern of **Dy** was collected at 296 K with an exposure time of 10 minutes. The XRD pattern of **Gd** was collected at 295 K with an exposure time of 30 minutes. The samples were loaded in a capillary glass tube with a 0.3 mm outer diameter and a 0.01 mm wall thickness, and rotated during the measurements.

3

Table S1. Crystallographic data and refinement parameters.

Compound	Gd	Gd′	Dy
CCDC number	2064815	2064816	2064814
Temperature / K	120	100	120
Crystal system	Tetragonal	Triclinic	Tetragonal
Space group	$I4_122$	$P\bar{1}$	$I4_122$
a / Å	23.2431(4)	9.1899(4)	23.1474(5)
b / Å	23.2431(4)	12.0151(5)	23.1474(5)
c / Å	33.3715(7)	14.4033(4)	33.2433(8)
α / °	90	97.498(3)	90
β / °	90	93.432(3)	90
γ / °	90	95.807(4)	90
Volume / Å³	18028.7(7)	1564.4(1)	17811.8(8)
Z	16	2	16
ρ_{calc} / g cm⁻³	1.447	1.702	1.473
μ / mm⁻¹	20.52	29.34	20.11
Radiation	Cu Kα (λ = 1.54184 Å)	Cu Kα (λ = 1.54184 Å)	Cu Kα (λ = 1.54184 Å)
2θ range for data collection / °	7.55–151.57	7.47–127.37	7.58–127.37
Index ranges	$-29 \leq h \leq 27$	$-10 \leq h \leq 10$	$-16 \leq h \leq 26$
	$-25 \leq k \leq 19$	$-13 \leq k \leq 13$	$-26 \leq k \leq 23$
	$-41 \leq l \leq 41$	$-15 \leq l \leq 16$	$-36 \leq l \leq 38$
Reflections collected	34231	13903	25778
Independent reflections	9226 [R_{int} = 0.073]	5130 [R_{int} = 0.141]	7335 [R_{int} = 0.058]
Data/restraints/parameters	9226/275/555	5130/0/298	7335/360/537
Goodness-of-fit on F^2	1.03	1.05	1.04
Final R_1 index [$F^2 \geq 2\sigma(F^2)$]	0.051	0.10	0.049
Final wR_2 index [F^2]	0.15	0.27	0.14
Largest diff. peak/hole / e Å⁻³	1.00/−1.65	3.68/−3.53	1.01/−1.94

118

Magnetometry

Direct current (dc) magnetization measurements were performed using the VSM option of a QuantumDesign Dynacool Physical Property Measurement System (PPMS) equipped with a 9 T superconducting magnet in between 1.7 K and 273 K. The polycrystalline samples were loaded into standard QuantumDesign powder capsules inside an Ar-filled glovebox, sealed with wax, and mounted in a standard brass sample holder. The sample holder was transferred air-tight to the PPMS chamber and the sample space was immediately evacuated and purged with He. The experimental magnetization data were corrected for diamagnetic contributions from the sample holder and the intrinsic sample diamagnetism. Alternating current (ac) magnetization data were acquired using the ACMS-II option (10–10,000 Hz, $H_{ac} \leq 16$ Oe) and on polycrystalline samples immobilized in polycarbonate capsules mounted in plastic drinking straws and handled as above. The paramagnetic relaxation times were extracted from the maxima of the $\chi''(\nu_{ac})$ data as $\tau^{-1} = 2\pi \nu_{ac}$.

Modelling of the magnetic properties of **Gd** was performed within the framework of the phenomenological spin-Hamiltonian formalism. Given that **Gd** can be considered as an eight-member ring made by alternating Gd(III) and bipy$^{\bullet-}$ and since both these species are relatively magnetically isotropic the simplest general form of spin-Hamiltonian ($\hat{H}$, Eq. 1, main text) appropriate for the phenomenological description of the magnetic properties of **Gd** should only contain terms expressing the isotropic magnetic exchange interaction between the constitutive centers and the isotropic response of the system to an external magnetic field according to the Zeeman interaction. The dimension, N, of the square matrix corresponding to the matrix representation of $\hat{H}$ for **Gd** is:

$$N = \prod_i^n (2S_i + 1) \qquad \text{Eq. S1}$$

resulting in $N = 8^4\ 2^4 = 65536$ for **Gd**. The magnitude of N precludes numerical diagonalization of the full spin-Hamiltonian matrix by conventional approaches[1] because of unrealistic computer memory and processor time requirements. Within the Irreducible Tensor Operator (ITO) formalism,[7] the isotropic exchange parameter, J_{ij}, is associated to a tensor operator $\hat{O}_q^K$ of order $K = 0$ and thus, necessarily of projection $q = 0$ ($-K \leq q \leq K$, with K and q integers), since it is associated to the scalar product, $\hat{S}_i \cdot \hat{S}_j$, of the Cartesian spin-operators. The matrix elements of a tensor operator $\hat{O}_q^K$ within the coupled total spin, S, basis $|s, S, M_S\rangle$ is given by:

$$\langle s, S, M_S | \hat{O}(k, K, q) | s', S', M_S' \rangle = (-1)^{S-M_S} \begin{pmatrix} S & K & S' \\ -M_S & q & M_S' \end{pmatrix} \langle s, S \| k, K \| s', S' \rangle \qquad \text{Eq. S2}$$

where s, s' and k are all necessary additional quantum numbers to fully define the problem, M_S is the projection of S along the quantization axis, the first term of the right-hand side is a phase, the second one is a 3-j symbol and the third is a reduced matrix element, independent of M_S. For the 3-j symbol to be non-zero a) the triangle relation has to hold for S, K and S', from where $S = S'$, since $K = 0$; and b) $M_S' - M_S = q$, has to hold. Thus, the isotropic exchange interaction has non-zero matrix elements only between basis-function of the same total spin S. Furthermore, since for the isotropic exchange associated tensor operator $\hat{O}_q^K$, $q = 0$, the matrix element of Eq. S2 is independent of M_S, to a phase factor of ± 1 which is irrelevant for the computation of eigenvalues. Thus, only one of the $2S+1$ projections of each total S multiplet is necessary to be included into this block-diagonal form of $\hat{H}_{iso}$, since the information contained in the $2S$ others is redundant. Finally, since $\hat{S}^2$ commutes with $\hat{S}_z$, $\hat{S}^2$ and $\hat{S}_z$ have a simultaneous eigenbasis specified by their respective eigenvalues S and M_S. This allows to transform the matrix representation of $\hat{H}$ for **Gd** into block-diagonal form, where each block corresponds to basis-functions of the same total spin S and projection M_S. Use of this methodology allows to transform the matrix representation of $\hat{H}$ for **Gd**, into block-diagonal form made up from seventeen blocks each corresponding to a total spin value S, ranging from 0 to 16, the dimensions of which are given below in Table S2.

Table S2. Total spin, S, and associated dimension, N_S, of the corresponding block in the block-diagonal form of the matrix representation of $\hat{H}$ for **Gd**.

S	N_S
16	1
15	7
14	24
13	56
12	104
11	168
10	248
9	344
8	452
7	556
6	632
5	664
4	648
3	584
2	472
1	312
0	110
sum	**5382**

6

120

The dimensions of the block-diagonal form of the matrix representation of $\hat{H}$ for **Gd** (Table S2) are compatible with standard numerical diagonalization approaches.[8] The number of independent isotropic magnetic exchange parameters that can, in principle, be included in $\hat{H}$ is determined by the number of different super-exchange paths between the Gd(III) and and bipy$^{\bullet-}$ in **Gd**. Herein we assume a unique isotropic exchange parameter, J, since all superexchange paths are symmetry related. Additional exchange interactions originating from magnetic dipole interactions are neglected because they are usually much smaller in magnitude than the exchange interactions via bridging ligands, as they depend inversely to the cube of the intermetallic distance. Using J as a unique fit parameter allowed the temperature dependence of the χT product and the M vs H data of **Gd** to be simultaneously numerically fitted, by use of the Levenberg-Marquardt algorithm,[9] to the isotropic spin-Hamiltonian $\hat{H}$. This resulted in the best fit parameters $J = 0.073(4)$ cm^{-1}. Under these conditions, the spin ground state of **Gd** is an $S = 12$ (Fig. S8), separated by the first excited state, a degenerate doublet of $S = 11$ states, by only 0.16 cm^{-1} at zero magnetic field.

NIR and MIR spectroscopy

The mid-IR and near-IR direct absorption spectra were collected by a VERTEX80v Fourier transform vacuum spectrometer from Bruker Optics GmbH. Highly air-sensitive samples of polycrystalline **Gd** were sandwiched between pairs of optically transparent KBr and CaF$_2$ windows for the mid-IR and near-IR recordings, respectively, and subsequently sealed effectively with silicone oil at the window edges in an argon-filled glove box. The FTIR apparatus was configured with a Ge on KBr beam splitter, a liquid N$_2$ cooled HgCdTe detector and a thermal globar radiation source for the mid-IR single-beam measurements collected with a spectral resolution of 2 cm^{-1}. The combination of a CaF$_2$ beam splitter, a liquid N$_2$ cooled InSb detector, and a thermal tungsten lamp source was employed for the near-IR single-beam measurements collected at a spectral resolution of 3 cm^{-1}. The resulting absorbance spectra were subsequently baseline-corrected slightly and minor traces of residual water vapor absorption were subtracted.

7
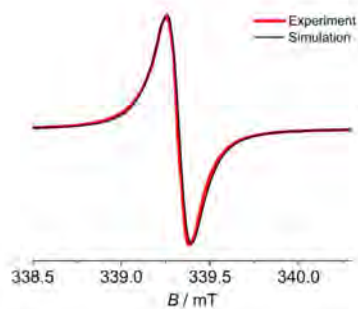
Fig. S1. Frozen-solution (CH₃CN) X-band (9.52 GHz) EPR spectrum at 77 K of the reaction product between one equivalent of Na metal and 2.5 mol equivalent of bipy, as described in the main text.
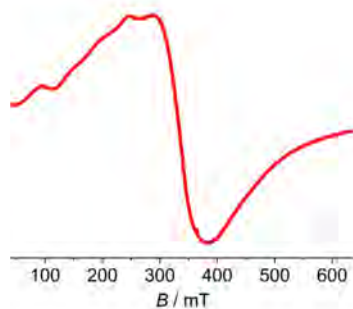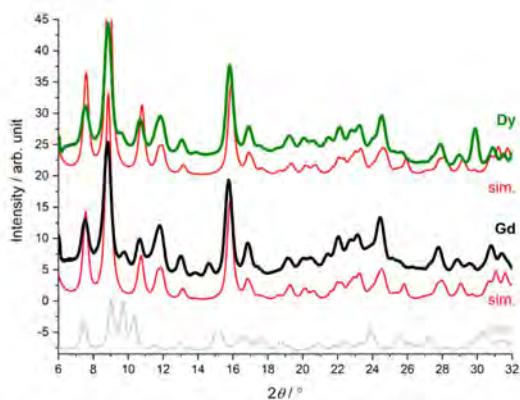

**Fig. S2.** X-band (9.52 GHz) EPR spectrum at 77 K of polycrystalline **Gd** obtained at 77 K.

8

122
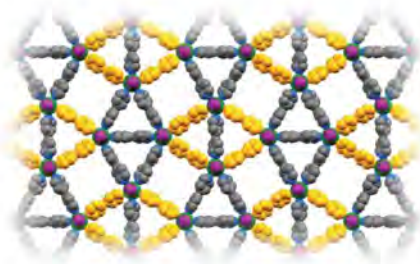
Fig. S3. Formation of {M$^{III}_4$(bipy^{-})$_4$} rhombi in **Gd** and **Dy** as suggested by single-crystal X-ray diffraction analysis. Color code: bipy^{-}, yellow; bipy^0, grey.
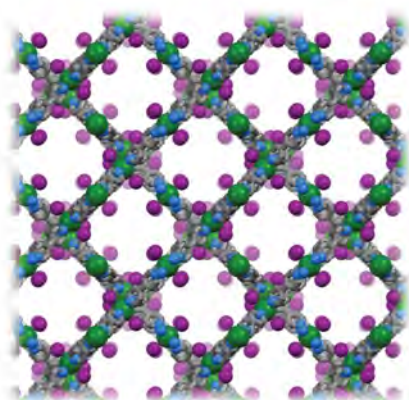
Fig. S4. Crystal structure of **Gd** shown along the crystallographic *c* axis showing the presence of interpenetrating 2D layers.

Fig. S5. Powder X-ray diffractograms of **Gd** and **Dy** and corresponding simulations from the 120-K single-crystal X-ray structures. The grey trace is a simulation of the powder diffractogram of **Gd′** (100 K).
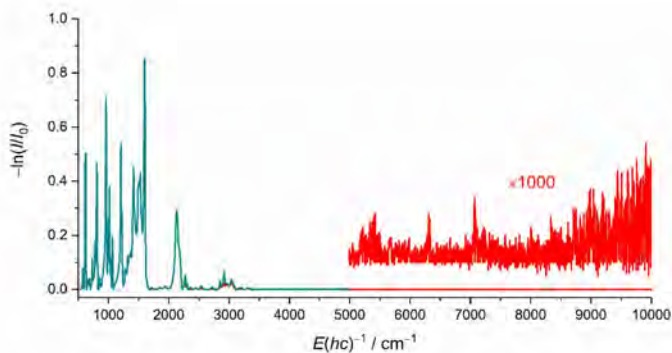
Fig. S6. Mid-IR/near-IR absorbance spectrum of polycrystalline **Gd** obtained at RT. The weak traces of gas-phase absorption lines around 5300–5400 cm^{-1} (combination of OH stretching fundamental + OH bending fundamental) and 7100-7200 cm^{-1} (first overtone of the OH stretching fundamental) comes from uncompensated water vapor absorption.

11

125
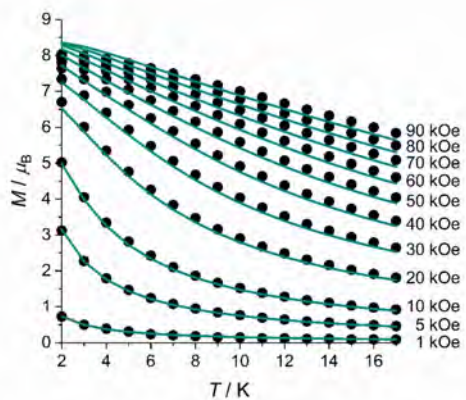
Fig. S7. Temperature dependence of the magnetization at selected magnetic field strengths for polycrystalline **Gd**. The turquoise solid lines are the best fit as described in the main text.
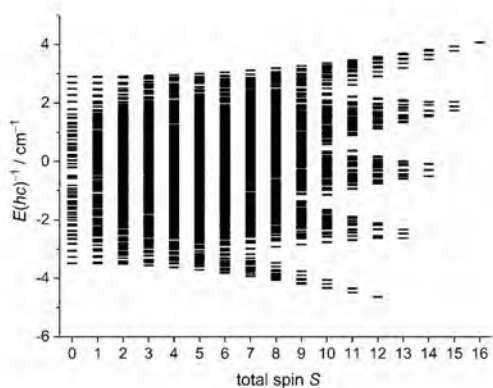
Fig. S8. Energy level spectrum of **Gd** determined as described in the main text.
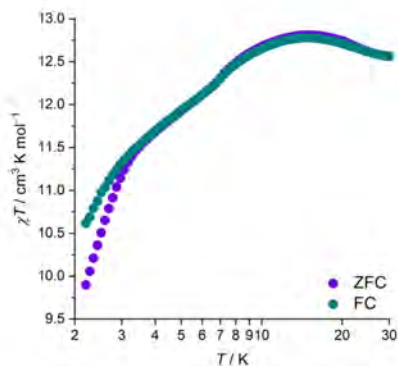
Fig. S9. Field-cooled (FC, 1000 Oe) and zero-field-cooled (ZFC) magnetization data plotted as χT vs T and obtained in heating mode with a magnetic field of $\mu_0 H$ = 1000 Oe.
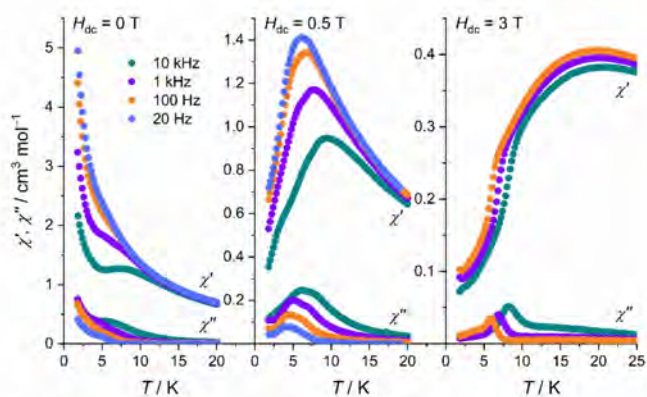
Fig. S10. Temperature dependence of the in-phase (χ') and out-of-phase (χ'') components of the ac susceptibility for polycrystalline **Dy** obtained with selected ac driving frequencies and in static (dc) fields of 0 T, 0.5 T, and 3 T.
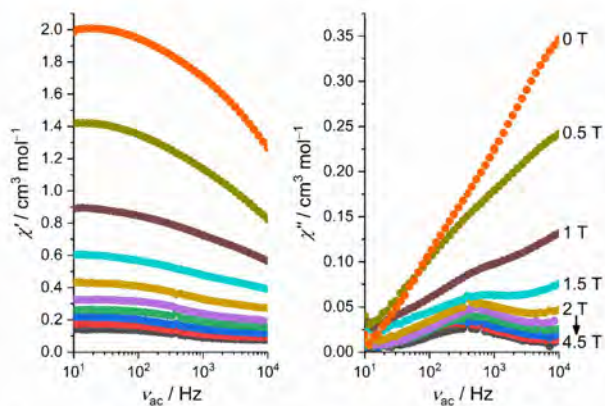
Fig. S11. Frequency dependence of the in-phase (χ', left) and out-of-phase (χ'', right) components of the ac susceptibility for polycrystalline **Dy** obtained in selected static (dc) fields at $T = 6.5$ K.
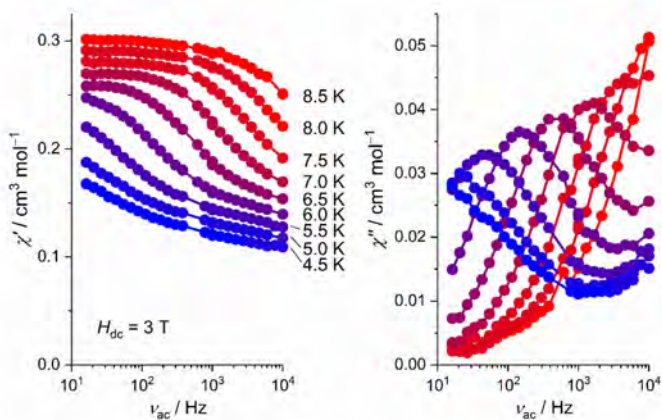
Fig. S12. Frequency dependence of the in-phase (χ', left) and out-of-phase (χ'', right) components of the ac susceptibility for polycrystalline **Dy** obtained at selected temperatures and in a static (dc) field of 3 T.

14

128

References

[1] O. V. Dolomanov, L. J. Bourhis, R. J. Gildea, J. A. K. Howard, H. Puschmann, *J. Appl. Cryst.* **2009**, *42*, 339-341.

[2] L. J. Bourhis, O. V. Dolomanov, R. J. Gildea, J. A. K. Howard, H. Puschmann, *Acta Cryst.* **2015**, *A71*, 59-75.

[3] G. M. Sheldrick, SHELXT-2018/2, Göttingen, Germany 2018.

[4] G.M. Sheldrick, *Acta Cryst.* **2015**, *C71*, 3-8.

[5] D. Kratzert, I. Krossing, *J. Appl. Cryst.* **2018**, *51*, 928-934.

[6] D. Kratzert, J. J. Holstein, I. Krossing, *J. Appl. Cryst.* **2015**, *48*, 933-938.

[7] B. L. Silver, Irreducible tensor methods: an introduction for chemists; Academic: New York, 36 **1976**.

[8] E. Anderson, LAPACK Users's Guide; 2nd ed.; Society for Industrial and Applied Mathematics: Philadelphia **1995**.

[9] W. H. Press, *et al.* Numerical recipes: the art of scientific computing; Cambridge University Press: Cambridge **1992**.

Paper 2

Towards Frustrated Magnetism in Europium(II) Archimedean Tessellations

<u>Hua Chen</u>,[†] Anna S. Manvell,[†] Mariusz Kubus, Giulia Lorusso, Mike S. B. Jørgensen, Søren Kegnæs, Susanne Mossin, Fabrice Wilhelm, Stergios Piligkos, Andrei Rogalev, Kasper S. Pedersen*, manuscript to be submitted to *Angewandte Chemie International Edition.*

Towards Frustrated Magnetism in Europium(II) Archimedean Tessellations

Hua Chen,[†] Anna S. Manvell,[†] Mariusz Kubus, Giulia Lorusso, Mike S. B. Jørgensen, Søren Kegnæs, Susanne Mossin, Fabrice Wilhelm, Stergios Piligkos, Andrei Rogalev, Kasper S. Pedersen*

Abstract: The self-assembly of EuI_2 and ditopic pyrazine or 4,4'-bipyridine leads to isoreticular, layered frameworks obeying the elongated triangular Archimedean tessellation pattern. The unique topology and the presence of intra-layer Eu(II)-Eu(II) antiferromagnetic interactions will lead to geometrical spin frustration, which constitutes the ingredient for the exploration of exotic magnetic phenomena in molecular lanthanide-based materials such as enhanced magnetic refrigeration.

Geometrically frustrated spins are found in materials where the symmetry of the crystal lattice precludes the simultaneous minimization of all magnetic exchange interactions. In extended networks, geometrical frustration of spins is at the foundation of exotic magnetic properties and phenomena such as spin-liquids[1] and -ices.[2] Herein, the most well-studied examples are those of the triangular, kagomé, and pyrochlore lattices.[3] Odd numbered rings, as triangles or pentagons, of metal ions with half-integer spins and with nearest-neighbor antiferromagnetic interactions are bona fide examples of systems showing competing exchange interactions and spin frustration. In molecular, i.e., 0D systems, such rings are realized in a multitude of coordination compounds,[4–7] which have led to promising perspectives for applications in e.g. spintronics and magnetocalorics.[7–10] In 2D, the triangular and kagomé lattices are examples of regular and semiregular (Archimedean) tessellations (Figure 1), respectively, and feature triangular motifs, which in analogy to the molecular systems, provide for competing antiferromagnetic interactions. Triangular networks are found in other tessellations, such as the elongated triangular tiling (cf. Figure 1e), that can be thought of as two-dimensionally arranged arrays of edge-sharing triangle

strands. Indeed, the majority of the 2D Archimedean tessellations are expected to display geometrical frustration when populated with antiferromagnetic interactions (cf. examples in Figure 1b-e), but materials with such topologies are exceedingly rare and geometrical frustration remains only observed for the kagomé lattice.[11]
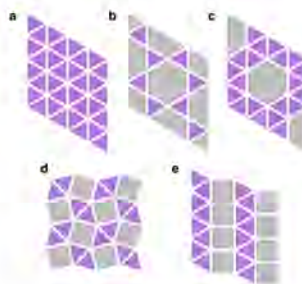
Figure 1. Examples of triangle-based 2D nets: triangular tessellation (3^6, a), and the kagomé (($3,6$)^2, b), snub hexagonal ($3^4.6$, c), elongated triangular ($3^3.4^2$, e), and snub square ($3^2.4,3,4$, e) Archimedean tilings.

Pioneering work on lanthanide-directed self-assembly by Écija, Barth, and coworkers led to the observation of Archimedean tessellation structures and dodecagonal quasicrystalline phases of lanthanide atoms linked by ditopic nitrile ligands.[12–14] Such molecular strategies to frustrated lanthanide-based materials is desirable due to the versatility and tunability offered by coordination and reticular chemistry. Despite the great potential, chemical control of the spatial and electronic structure in bulk lanthanide-based coordination solids is rare and difficult to acquire, due to the intrinsic absence of directionality in the coordination chemistry of the lanthanide ions. We recently reported that the self-assembly of YbI_2 with 4,4'-bipyridine (bipy) results in the formation of a two-dimensional coordination solid, $YbI_2(bipy)_{5/2}$, which contains pentagonal bipyramidal Yb(II) nodes enforced by the presence of spacious *trans*-positioned iodide ligands.[15] The structure of the layer conforms to the elongated triangular (in vertex notation: $3^3.4^2$) Archimedean tessellation (Figure 1e). Similarly, the reaction of LnI_3 (Ln = Gd, Dy) with bipy and elemental Na led to the related $LnI_2(bipy)_{5/2}$ coordination solids, which, however, contain Ln(III) nodes and a "redox non-innocent", mixed-valency bipy•−/bipy^0 ligand scaffold.[16] The possibility to tailor the materials' electronic ground state by the choice of lanthanide ion and the apparent structure directing {*trans*-LnI_2}$^{+/0}$ nodes provides a unique possibility for designing

[*] H. Chen, A. Manvell, Dr. M. Kubus, Dr. M. S. B. Jørgensen, Prof. Dr. S. Kegnæs, Prof. Dr. S. Mossin, Prof. Dr. K. S. Pedersen
Department of Chemistry, Technical University of Denmark, DK-2800 Kongens Lyngby, Denmark
E-mail: kastp@kemi.dtu.dk

Dr. G. Lorusso
CNR Institute for Microelectronics and Microsystems, 40129 Bologna, Italy

Dr. A. Rogalev, Dr. F. Wilhelm
European Synchrotron Radiation Facility, BP 220, 38043 Grenoble Cedex 9 (France).

Prof. Dr. S. Piligkos
Department of Chemistry, University of Copenhagen, DK-2300 Copenhagen, Denmark

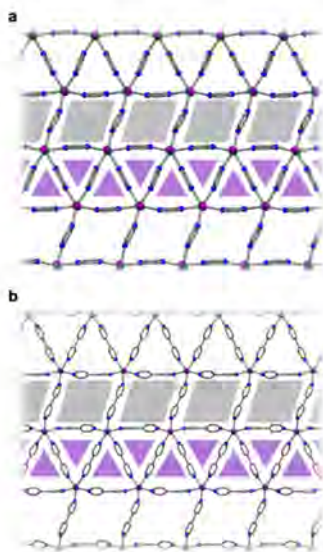[†] These authors contributed equally to this work.

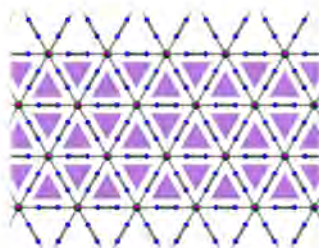Supporting information and the ORCID identification number(s) for the author(s) of this article can be found under: https://doi.org/10.1002/anie.xxxxxx.

and controlling novel lanthanide-based coordination solids in 2D. Herein, we report two isoreticular {trans-Eu^{II}I$_2$}-based coordination solids, differing in the ditopic linker units, but with fully conserved pentagonal bipyramidal coordination around the constituent Eu(II) ions, which fulfill all requirements for the observation of geometrical frustration in a non-kagomé Archimedean tessellation.

The self-assembly reaction of EuI$_2$ and pyrazine (pyz), or bipy, in acetonitrile at –20 °C yielded over several days orange single-crystals of **EuI$_2$(pyz)$_{5/2}$** and **EuI$_2$(bipy)$_{5/2}$**, respectively, suitable for single-crystal X-ray diffractometry. **EuI$_2$(pyz)$_{5/2}$** crystallizes in the triclinic space group $P\bar{1}$ as EuI$_2$(pyz)$_{5/2}$ without any co-crystallized solvent molecules and with the local coordination environment of Eu slightly distorted from an D_{5h}-symmetric {EuI$_2$N$_5$} pentagonal bipyramid (I—Eu—I = 178.3°, Eu—N = 2.72–2.75(8) Å; Figures 2a, S1-2, S7, Table S1 Supporting Information). The Eu—I bond lengths (3.19 Å) are slightly shorter than those found in structurally related Eu(II) complexes such as [EuI$_2$(CH$_3$CN)$_5$] (3.22–3.24 Å),[17] although significantly longer than found in related {trans-Eu^{III}I$_2$}$^+$ complexes (3.03–3.09 Å).[18] The tessellation pattern of **EuI$_2$(pyz)$_{5/2}$** can be described as distorted elongated triangular pattern with a tilting angle, α, of 72.5°. The departure of α from 90° is significantly

larger than those found in both of the previously obtained coordination solids with distorted elongated triangular tessellations (LnI$_2$(bipy)$_{5/2}$, Ln = Gd (α = 78.7°),[16] Yb (α = 89.9°)[15]) and the coordination geometry of Eu may, alternatively, be described as approaching a defect hexagonal bipyramid. Importantly, the triangular motifs are close to perfect equilateral triangles with Eu···Eu distances (8.1887(9) Å, 8.271(1) Å, 8.226(1) Å) and Eu···Eu···Eu angles (60.51(1)°, 59.52°, 59.96(1)°) departing by less than 1% from ideality. The absence of hexagonal equatorial coordination in **EuI$_2$(pyz)$_{5/2}$** contrasts the observation in the on-surface reaction of Eu atoms and ditopic nitrile ligands,[12] which is likely rooted in the presence of different Eu oxidation states in the two materials. The large Eu^{2+} ion (ionic radius = 1.4 Å for 8-coordination) is only surpassed by the largest metal ions such as Ba^{2+} (ionic radius = 1.6 Å for 8-coordination).[19] Indeed, the reaction of anhydrous BaI$_2$ with pyz in acetonitrile yielded colorless, hexagonal crystals. Crystallographic analysis showed the compound to be **BaI$_2$(pyz)$_{6/2}$**, which crystallizes in the rhombohedral space group $R\bar{3}m$ (Figures 3, S3-4, S8, Table S1, Supporting Information). The Ba center possesses crystallographic six-fold rotational symmetry with I—Ba—N angles of 90°. The Ba—N bond lengths of 2.95 Å are significantly longer (7%) than those found in **EuI$_2$(pyz)$_{5/2}$** reflecting the increase in ionic radius of the metal ion node. Previously, only few molecular materials have been shown to comply with the triangular tessellations, all of which are relying on cluster-based secondary building units.[20,21] Thus, **BaI$_2$(pyz)$_{6/2}$** constitutes the first example of a triangular tessellation pattern in a simple, bulk coordination solid.

Figure 2. Truncated tessellation structures of **EuI$_2$(pyz)$_{5/2}$** (a) and **EuI$_2$(bipy)$_{5/2}$** (b) as determined from single-crystal X-ray diffraction analysis at T = 120(1) K. Color codes: Eu, green; I, purple; N, blue. The C skeleton is shown as capped sticks and H atoms have been omitted for clarity. The tessellations are stacked in an ABC fashion with a separation of 7.5 Å between the Eu layers (Figures S2, S6, Supporting Information).
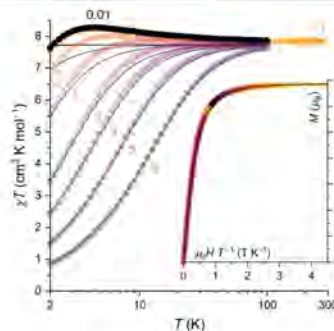

Figure 3. Truncated tessellation structure of **BaI$_2$(pyz)$_{6/2}$** as determined from single-crystal X-ray diffraction analysis at T = 120(1) K. Color codes: Ba, pale green; I, purple; N, blue. The C skeleton is shown as capped sticks and H atoms have been omitted for clarity.

The **EuI$_2$(bipy)$_{5/2}$**, which features the longer bipy linker, crystallizes in the triclinic space group $P\bar{1}$ with one co-crystallized acetonitrile molecule per formula unit (Figures 2b, S5-6, S9 Supporting Information), is structurally similar, but not isomorphous, to the previously reported triclinic phases of (LnI$_2$(bipy)$_{5/2}$, Ln = Gd, Yb). The local coordination geometry metrics are strikingly similar to that of **EuI$_2$(pyz)$_{5/2}$** (I—Eu—I = 175.77(1)°, Eu—I = 3.2250(6) Å, 3.2356(6) Å, Eu—N = 2.676(5)–2.736(5) Å). Similarly, **EuI$_2$(bipy)$_{5/2}$** forms a distorted elongated triangular tiling (α = 75.4°) without any indications of concomitant formation of other phases (Figure S9, Supporting Information).
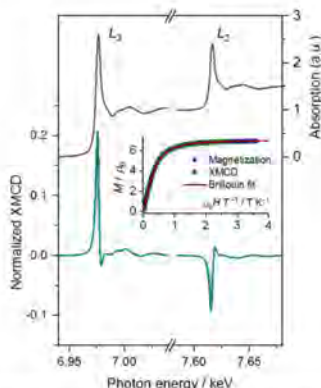
Figure 4. XANES and XMCD spectra of **EuI₂(pyz)₅/₂** at the Eu L_2 and L_3 edges recorded at 6.3 K. The inset shows the superposition of the field dependence of the XMCD recorded at the photon energy corresponding to the maximum dichroism at the L_3 edge.

Figure 5. Temperature dependence of the χT product at selected magnetic field strengths (indicated in units of Tesla) for polycrystalline **EuI₂(pyz)₅/₂**. Black lines show the corresponding, calculated χT products for an isolated $S = 7/2$ ion with $g = 1.98$. Eu(II) Inset: Magnetic field-dependence of the magnetization of **EuI₂(pyz)₅/₂** at temperatures between 2 K and 15 K and between 0 T and 9 T. The solid black line represents the Brillouin function for $S = 7/2$ with $g = 1.98$.

Recently, some of us reported the coordination solid CrCl₂(pyz)₂ to incorporate Cr(III) and a partially reduced pyz scaffold, owing to the significant reducing powder of Cr(II) that constitutes the starting material ($E°_{Cr(III)/Cr(II)} = -0.41$ V).[22] In the lanthanide series, the least reducing divalent ion is Eu(II), whose electrochemical potential compares well to that of Cr(II) ($E°_{Eu(III)/Eu(II)} = -0.35$ V) and thus could be anticipated to be subject to oxidation when coordinated to ligands with well-known redox reactivity towards Cr(II), such as pyz and bipy.[23,24] For **EuI₂(pyz)₅/₂**, the oxidation state assignment by the structural analysis was corroborated by X-ray absorption spectroscopy (XAS) around the Eu L_1, L_2, and L_3 absorption edges (Figure 10, Supporting Information). The room-temperature spectra reveal intense "white lines" at energies and shape similar to those of EuI₂, which are present at ~8 eV lower photon energy than the same transitions in EuCl₃ (note that EuI₃ does not exist). The X-ray magnetic circular dichroism (XMCD) was determined at 6.3 K at the $L_{2,3}$ edges as the difference between subsequent XANES spectra obtained with opposite photon helicity or magnetic field direction (±17 T; Figure 4). Whilst XMCD spectra of the isoelectronic Gd(III) are well-described in the literature, there are only few XMCD studies on Eu(II) compounds, and none on molecule-based materials. The $L_{2,3}$-edge XMCD, predominantly probing the 2p → 5d electric dipole-allowed transitions, reflects the magnetic polarization of the unoccupied 5d levels in Eu(II). The L_2 and L_3 XMCD signals are opposite in sign and with line shapes in good agreement with those previously reported for both metallic and insulating compounds of the isoelectronic Gd(III). The magnetic field-dependence of the maximum dichroism intensity at the L_3 edge can be superposed to the bulk magnetization data demonstrating the paramagnetic nature of the measured XMCD response (Figure 4, inset).

The room-temperature value of the dc magnetic susceptibility-temperature product, χT ($\chi = M/\mu_0 H$), amounts to 7.8, and 7.7 cm³ K mol⁻¹, for **EuI₂(pyz)₅/₂** and **EuI₂(bipy)₅/₂**, respectively (Figures 5, S11). These values are in good agreement with the Curie constant for the orbitally nondegenerate Eu²⁺ (7.9 cm³ K mol⁻¹, $g = 2$) and corroborate the aforementioned oxidation state assignment and excludes the possibility for a relevance of Eu(III)-radical valence tautomers. For **EuI₂(pyz)₅/₂**, the χT product (0.1 T; Figure 5) stays constant on lowering temperature before increasing slightly below ca. 20 K, suggesting the presence of weak ferromagnetic interactions between Eu(II) ions. This behavior is qualitatively identical to that found in [EuI₂(CH₃CN)₅] that exhibits ferromagnetic interactions between isolated molecules.[17] The χT product maximizes at 4 K before dropping, indicative of the presence of antiferromagnetic interactions, zero-field splitting (zfs), magnetic field-saturation, or a combination of contributions. However, the analogous data, obtained at 0.01 T (Figure 5), virtually coincide with the 0.1 T-data, ruling out the relevance of saturation effects. Secondly, the zfs splitting of 4f⁷ systems is exceedingly small, with projected vanishing influence of the χT product at 4 K,[25] suggesting the relevance of antiferromagnetic Eu(II)-Eu(II) interactions in addition to the ferromagnetic ones. A Curie-Weiss law ($\chi^{-1} \propto T - \theta_{CW}$) fit to the χ^{-1} vs T data (0.1 T, 15–300 K) provides a vanishing Weiss constant of $\theta_{CW} = -0.07(3)$ K (Figure S12, Supporting Information). The absence of any sizable magnetic exchange interactions in **EuI₂(pyz)₅/₂** is evident from the magnetic field-dependence of the magnetization (Figure 5, inset, and Fig. S11, Supporting Information). The coincidence of the data onto a Brillouin function calculated for $S = 7/2$ ($g = 1.98$) further confirms the magnetically isotropic nature of both compounds. No anomalies were observed in the alternating current (ac) susceptibility measurements (Figure S12) confirming the absence of any long-range magnetic order above 1.8 K in **EuI₂(pyz)₅/₂**. The magnetic properties are

COMMUNICATION
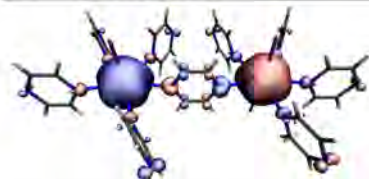
Figure 6. DFT-calculated spin density plot (isosurface value = ±0.001 a.u.) for the (7,7)-broken symmetry state of a dinuclear fragment of $EuI_2(pyz)_{5/2}$

remarkably similar between $EuI_2(pyz)_{5/2}$ and $EuI_2(pyz)_{5/2}$ (Figure S11, Supporting Information), although the room-temperature EPR spectra reveal entirely different spectral behavior (Figure S14, Supporting Information). Broken-symmetry DFT calculations on dinuclear $[Eu_2I_4(pyz)_8(\mu\text{-pyz})]$ fragments representing the four crystallographically different pyrazine bridges were performed at the B3LYP/ZORA-def2-TZVP level. The integrated Mulliken spin populations of the Eu sites amount to 6.98, in agreement with the expected 7.0 for a fully ionic Eu(II) (cf. Figures 6, S15, Supporting Information), and with zero net spin density on the bridging pyz ligands. The broken-symmetry (7,7) state is stabilized by 14.9–16.4 cm^{-1} to the high-spin state, which, using the approach by Yamaguchi, can be projected onto Eu–Eu super-exchange coupling constants ranging between −0.30 and −0.34 cm^{-1} (using the $-2J\,\hat{S}_{Eu1}\hat{S}_{Eu2}$ Hamiltonian definition). As discussed in the previous, the inter-layer interactions could be mediated by closest spaced Eu···Eu magnetic coupling. BS-DFT calculations suggest weak ferromagnetic interactions (Figure S16, Supporting Information), albeit with a vanishing stabilization (0.2 cm^{-1}) which, however, is close to the value estimated for the maximum energy of the dipolar coupling, μ^2/r^3, of ~0.03 cm^{-1}.

In summary, we have reported two rare examples of coordination solids based on divalent Eu(II) ions. The structural analysis demonstrated that $EuI_2(pyz)_{5/2}$ and $EuI_2(bipy)_{5/2}$ feature isoreticular, distorted elongated triangular tessellations with similar magnetic properties. Frustrated coordination networks remain exceedingly rare and are limited to the kagomé lattices.[26] Albeit weak, the presence of both ferro- and antiferromagnetic interactions is measurable in $EuI_2(pyz)_{5/2}$ and $EuI_2(bipy)_{5/2}$ which provide the basis for observation of phenomena derived from the geometric frustration. The new materials may serve as test beds for the exploration, and eventual amplification, of the unique properties tied to frustrated magnetism in molecular lanthanide clusters. For instance, the magnetocaloric effect may increase tremendously if the entropy experiences a drastical dependence of the magnetic field. Previous results have demonstrated the importance of antiferromagnetic interactions to supply the large entropy associated to the degenerate ground state, while limiting the magnitude of the interaction to facilitate full availability of the magnetic entropy upon demagnetization.[27] Thus, materials with tunable interactions and frustrated ground states may have interesting applications in ultra-low temperature refrigeration.

[1] L. Balents, *Nature* **2010**, *464*, 199–208.
[2] S. T. Bramwell, M. J. P Gingras, *Science (1979)* **2000**, *294*, 1495–1501.
[3] A. Harrison, *J. Phys. Condens. Matter* **2004**, *16*.
[4] B. Cage, F. A. Cotton, N. S. Dalal, E. A. Hilliard, B. Rakvin, C. M. Ramsey, *J. Am. Chem. Soc.* **2003**, *125*, 5270–5271.
[5] N. Hoshino, M. Nakano, H. Nojiri, W. Wernsdorfer, H. Oshio, *J. Am. Chem. Soc.* **2009**, *131*, 15100–15101.
[6] O. Cador, D. Gatteschi, R. Sessoli, F. K. Larsen, J. Overgaard, A. L. Barra, S. J. Teat, G. A. Timco, R. E. P. Winpenny, *Angew. Chem. Int. Ed.* **2004**, *43*, 5196–5200.
[7] M. L. Baker, G. A. Timco, S. Piligkos, J. S. Mathieson, H. Mutka, F. Tuna, P. Kozłowski, M. Antkowiak, T. Guidi, T. Gupta, H. Rath, R. J. Woolfson, G. Kamieniarz, R. G. Pritchard, H. Weihe, L. Cronin, G. Rajaraman, D. Collison, E. J. L. McInnes, R. E. P. Winpenny, *Proc Natl Acad Sci U S A* **2012**, *109*, 19113–19118.
[8] J. Schnack, *Dalton Trans.* **2010**, *39*, 4677–4686.
[9] J. W. Sharples, D. Collison, E. J. L. McInnes, J. Schnack, E. Palacios, M. Evangelisti, *Nat. Commun.* **2014**, *5*, 1–6.
[10] Y. Wu, M. D. Krzyaniak, J. F. Stoddart, M. R. Wasielewski, *J. Am. Chem. Soc.* **2017**, *139*, 2948–2951.
[11] D. J. J. Farnell, O. Götze, J. Schulenburg, R. Zinke, R. F. Bishop, P. H. Y. Li, *Phys J Rev. B* **2018**, *98*, 224402.
[12] J. I. Urgel, D. Écija, G. Lyu, R. Zhang, C. A. Palma, W. Auwärter, N. Lin, J. v. Barth, *Nat. Chem.* **2016**, *8*, 657–662.
[13] D. Écija, J. I. Urgel, A. P. Seitsonen, W. Auwärter, J. v. Barth, *Acc. Chem. Res.* **2018**, *51*, 365–375.
[14] D. Écija, J. I. Urgel, A. C. Papageorgiou, S. Joshi, W. Auwärter, A. P. Seitsonen, S. Klyatskaya, M. Ruben, S. Fischer, S. Vijayaraghavan, J. Reichert, J. v. Barth, *Proc Natl Acad Sci U S A* **2013**, *110*, 6678–6681.
[15] L. Voigt, M. Kubus, K. S. Pedersen, *Nat. Commun.* **2020**, *11*, 1–6.
[16] H. Chen, L. Voigt, M. Kubus, D. Mihrin, S. Mossin, R. W. Larsen, S. Kegnæs, S. Piligkos, K. S. Pedersen, *J. Am. Chem. Soc.* **2021**, *143*, 14041–14045.
[17] M. Kubus, L. Voigt, K. S. Pedersen, *Inorg. Chem. Commun.* **2020**, *114*, 107819–107821.
[18] R. D. Bannister, W. Levason, M. E. Light, G. Reid, *Polyhedron* **2018**, *154*, 259–262.
[19] R. D. Shannon, *Acta Crystallogr.* **1976**, *32*, 752–767.
[20] D. M. Chen, X. P. Zhang, W. Shi, P. Cheng, *Inorg. Chem.* **2015**, *54*, 5512–5518.
[21] A. L. Cheng, Y. Ma, Q. Sun, E. Q. Gao, *CrystEngComm* **2011**, *13*, 2721–2726.

WILEY-VCH

[22] K. S. Pedersen, P. Perlepe, M. L. Aubrey, D. N. Woodruff, S. E. Reyes-Lillo, A. Reinholdt, L. Voigt, Z. Li, K. Borup, M. Rouzières, D. Samohvalov, F. Wilhelm, A. Rogalev, J. B. Neaton, J. R. Long, R. Clérac, *Nat. Chem.* **2018**, *10*, 1056–1061.

[23] A. J. Miralles, A. Haim, *Inorg. Chem.* **1980**, *19*, 1158–1160.

[24] T. G. Dunne, J. K. Hurst, *Inorg. Chem.* **1980**, *19*, 1152–1157.

[25] J. A. Clayton, K. Keller, M. Qi, J. Wegner, V. Koch, H. Hintz, A. Godt, S. Han, G. Jeschke, M. S. Sherwin, M. Yulikov, *Phy. Chem. Chem. Phy.* **2018**, *20*, 10470–10492.

[26] Z. Meng, C. G. Jones, S. Farid, I. U. Khan, H. M. Nelson, K. A. Mirica, *Angew. Chem. Int. Ed.* **2022**, *61*, DOI 10.1002/anie.202113569.

[27] E. M. Pineda, G. Lorusso, K. H. Zangana, E. Palacios, J. Schnack, M. Evangelisti, R. E. P. Winpenny, E. J. L. McInnes, *Chem. Sci.* **2016**, *7*, 4891–4895.

135

Towards Frustrated Magnetism in Eu(II) Archimedean Tessellations

Hua Chen, Anna Manvell, Mariusz Kubus, Mike S. B. Jørgensen, Giulia Lorusso, Søren Kegnæs, Susanne Mossin, Fabrice Wilhelm, Stergios Piligkos, Andrei Rogalev, Kasper S. Pedersen

Angewandte Chemie International Edition

136

Synthesis

All procedures were carried out in an InertLab glovebox under a dry Ar atmosphere. Elemental analysis was performed by the Mikroanalytisches Laboratorium Kolbe (Oberhausen, Germany). EuI_2 (99.99%), BaI_2 (99.995%), pyrazine (>99%), and 4,4'-bipyridine were supplied by Sigma-Aldrich and were used as received. Dry and oxygen-free solvents were obtained from a Puresolv MD 7 solvent purification system.

Synthesis of EuI₂(pyz)₅/₂: EuI_2 (101.3 mg, 250 μmol) and pyz (500 mg, 6.25 mmol) were dissolved in 4 mL of MeCN separately. The two solutions were then mixed by stirring for 1 h at room temperature. A reddish crystalline powder was formed. The solid material was isolated using suction filtration. Yield: 38.3 mg (25.3%). Anal. calcd. (found) for $C_{10}H_{10}I_2N_5Eu$ (**EuI₂(pyz)₅/₂**): C, 19.91 (19.80); H, 1.67 (1.65); N, 11.53 (11.55); I, 41.51 (41.91); Eu, 24.79 (25.08).

Reddish single crystals suitable for SCXRD were obtained via slow diffusion. EuI_2 powder (101.3 mg, 250 μmol) was placed in a standard test tube (160 mm × 16 mm, soda glass). An acetonitrile solution (8 mL) of pyz (800 mg, 10 mmol) was slowly layered on top of it, and the reaction mixture was left undisturbed in a refrigerator at −20 °C for 11 days to afford dark-reddish crystals.

Synthesis of EuI₂(bipy)₅/₂: EuI_2 (101.3 mg, 250 μmol) and bipy (195 mg, 1.25 mmol) were dissolved in 7 mL of MeCN separately. The two solutions were then mixed by stirring for 2 h at room temperature. A reddish crystalline powder was formed. The solid material was isolated using suction filtration. Yield: 134.6 mg (64.34%). Anal. calcd. (found) for $C_{27}H_{23}I_2N_6Eu$ (**EuI₂(bipy)₅/₂·C₂H₃N**): C, 38.71 (38.44); H, 2.75 (2.65); N, 10.04 (9.92); I, 30.35 (30.14); Eu, 18.16 (18.04).

Single crystals suitable for SCXRD were obtained via slow diffusion. EuI_2 powder (10.1 mg, 25μmol) was placed in an NMR test tube (tube diam. 5 mm, size 7 in.). An acetonitrile solution (bipy (19.5 mg, 125 μmol) dissolved in 2 mL MeCN) was slowly layered on top of it, and the reaction mixture was left undisturbed in a refrigerator at −20 °C for 14 days.

Synthesis of BaI₂(pyz)₆/₂: To a solution of 97.3 mg BaI_2 (0.248 mmol) in 2 mL acetonitrile a solution of 500 mg (6.23 mmol) pyrazine in 2 mL acetonitrile was added. After a few minutes a white powder precipitated, and the solution was left stirring for 1 h before the white powder was isolated. Crystals suitable for single crystal x-ray diffraction was obtained by adding a solution of 500 mg pyrazine (6.23 mmol) in 4 mL acetonitrile to a solution of 97.3 mg BaI_2

(0.248 mmol) in 4 mL acetonitrile. The solution was slowly evaporated under a dynamic vaccum and within 3-5 h colorless crystals formed.

Crystallography

Single crystals of **EuI$_2$(pyz)$_{2.5}$** and **EuI$_2$(bipy)$_{2.5}$** were covered in polybutene oil (Aldrich, >90%) in glovebox. Under microscope, the single crystals were subsequently mounted on a nylon loop which was attached to a SuperNova Dual Source CCD-diffractometer. The data were obtained at T = 120 K by using Cu Kα (λ = 1.5406 Å) radiation. The structures were solved by using olex2.solve[1] structure solution program of Olex2[2] and refined by least squares using SHELXL.[3] All non-hydrogen atoms were refined anisotropically. The powder X-ray diffraction patterns of **EuI$_2$(pyz)$_{2.5}$** and **EuI$_2$(bipy)$_{2.5}$** were measured at room temperature in sealed holders with a Huber G670 powder diffractometer using Cu Kα (λ = 1.5406 Å, quartz monochromator) radiation in transmission mode. The sample preparation was conducted under an inert atmosphere. The PXRD patterns of **EuI$_2$(pyz)$_{2.5}$** and **EuI$_2$(bipy)$_{2.5}$** were exposed in radiation for 10 mins and 60 mins, respectively.

X-ray spectroscopy

X-ray absorption (XANES) and dichroism (XMCD) spectra at the Eu $L_{1,2,3}$-edges were obtained at the ID12 beamline of the ESRF – The European Synchrotron facility in Grenoble, France, which is a dedicated to polarization dependent X-ray spectroscopy utilizing 2–15 keV incident photon energies.[4] The circular polarized photon beam was generated by a HELIOS-II undulator and monochromatized by a Si <111> double-crystal monochromator. The low-temperature XANES and XMCD spectra of **EuI$_2$(pyz)$_{5/2}$** were obtained using the total fluorescence yield detection mode, while the room-temperature XANES spectra of **EuI$_2$(pyz)$_{5/2}$**, EuI$_2$, and EuCl$_3$ were obtained from transmission.

Magnetization Measurements and Analysis

The direct-current (dc) magnetization measurements were performed with the vibrating sample magnetometer (VSM) option using a QuantumDesign Dynacool Physical Property Measurement System (PPMS) in the temperature range from 2 K to 270 K and in magnetic fields between $\mu_0 H$ = ±9 T. Polycrystalline samples were loaded and sealed in standard QuantumDesign powder capsules and sealed with Teflon tape inside an Ar-filled glovebox. The magnetization data were corrected for diamagnetic contributions of both the sample and the sample container. Alternating current (ac) susceptibility measurements on **EuI$_2$(pyz)$_{5/2}$** were performed on the same instrument by using the ACMS-II option. The polycrystalline samples were loaded and sealed in polycarbonate capsules which subsequently were immobilized in a drinking straw. The data were acquired between 1.8 K and 20 K using ac frequencies from 10 Hz to 10 kHz. The model calculations of the dc magnetization

138

data were performed using the MagProp programme which is included in the DAVE programme suite.[5] The calculations utilized matrix-diagonalization of the spin-Hamiltonian matrix and were based on the isotropic Zeeman Hamiltonian $\mathscr{H} = g\mu_B\mu_0 H\hat{S}$.

DFT Calculations

The DFT calculations were performed using the ORCA programme suite,[6] employing scalar relativistic effects through the 0th-order regular approximation (ZORA).[7] The experimentally determined atomic coordinates of **EuI$_2$(pyz)$_{5/2}$** and **EuI$_2$(bipy)$_{5/2}$** were used to generated dieuropium fragments as input without any subsequent geometry optimization. For all calculations, the B3LYP functional was combined with the scalar-relativistically recontracted (SARC) version of the ZORA-def2-TZVP basis set[8] together with the corresponding auxiliary basis.[9] For both systems a high-spin (HS) $S = 7$ calculation and a $S_{Eu1} = 7/2 - S_{Eu2} = 7/2$ broken symmetry calculation (BS(7,7)) were performed. The calculated energy difference between the BS and HS states were utilized to evaluate the superexchange coupling constant, J, obtained as suggested by Yamaguchi.[10] Spin density plots and Kohn-Sham frontier orbital plots were rendered using the VMD program.[11]

Electron Paramagnetic Resonance (EPR) spectroscopy

The EPR spectra was obtained on a Bruker EMX X-band EPR spectrometer. The samples were loaded and sealed in Suprasil quartz tubes in a glovebox. Afterwards placed the tubes in a ER4102ST rectangular cavity. Magnetic field was scanned from 50 to 6050 mT, modulation frequency 100 kHz, amplitude 5 G, microwPave frequency 9.48 GHz, power 0.42 mW, time constant 20 ms.

Compound	EuI$_2$(pyz)$_{5/2}$	EuI$_2$(bipy)$_{5/2}$	BaI$_2$(pyz)$_{6/2}$
Temperature / K	120	120	120
Crystal system	Triclinic	Triclinic	Trigonal
Space group	$P\bar{1}$	$P\bar{1}$	$R\bar{3}m$
a / Å	8.1887(6)	9.0674(3)	8.6925(2)
b / Å	8.9713(8)	10.0549(4)	8.6925(2)
c / Å	12.6250(10)	19.0923(8)	22.4417(6)
α / °	93.074(7)	88.771(3)	90
β / °	95.675(6)	82.801(3)	90
γ / °	92.674(7)	79.883(3)	120
Volume / Å^3	920.34(13)	1700.11(11)	1468.51(8)
Z	2	2	3
ρ_{calc} / g cm^{-1}	2.187	1.636	2.142
Radiation	Cu Kα (λ = 1.54184 Å)	Mo Kα (λ = 0.71073 Å)	Mo Kα (λ = 0.71073 Å)
2θ range for data collection / °	7.048 to 133.972	6.674 to 52.744	6.518 to 59.358
Index ranges	$-7 \leq h \leq 9$ $-10 \leq k \leq 10$ $-13 \leq l \leq 15$	$-11 \leq h \leq 11$ $-12 \leq k \leq 12$ $-23 \leq l \leq 23$	$-11 \leq h \leq 11$ $-12 \leq k \leq 12$ $-30 \leq l \leq 31$
Reflections collected	6976	34986	21844
Independent reflections	3275 [R_{int} = 0.0595]	6952 [R_{int} = 0.0915]	550 [R_{int} = 0.0390]
Data/restraints/parameters	3275/0/163	6952/48/314	550/0/20
Goodness-of-fit on F^2	1.004	1.054	1.223
Final R_1 index of [$F^2 \geq 2\sigma(F^2)$]	0.0484	0.0411	0.0136
Final wR_1 index of [F^2]	0.0629	0.0967	0.0157
Largest diff. peak/hole/ e Å^{-3}	1.97/−1.92	1.41/−1.08	0.46/-0.55

5

140

Figure S1. Thermal ellipsoid (50% probability level) plot of the asymmetric unit of **EuI₂(pyz)₅/₂**. Colour code: Eu, green; I, purple; N, blue; C, grey. Hydrogen atoms have been omitted.
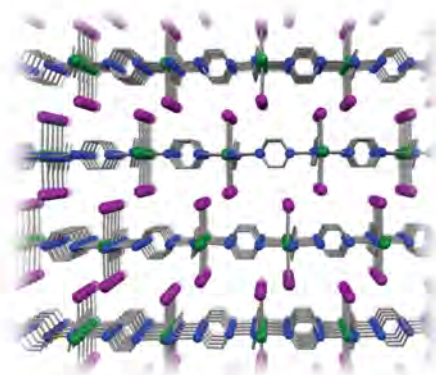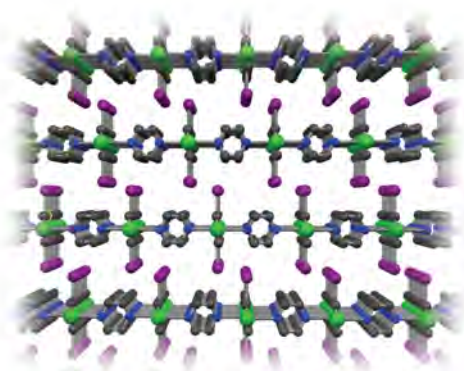

Figure S2. Perspective view of the layer structure in **EuI₂(pyz)₅/₂**. Colour code: Eu, green; I, purple; N, blue; C, grey. Hydrogen atoms have been omitted.

Figure S3. Thermal ellipsoid (50% probability level) plot of the asymmetric unit of **BaI₂(pyz)₆/₂**. Colour code: Eu, pale green; I, purple; N, blue; C, grey. The hydrogen atom has been omitted.

Figure S4. Perspective view of the layer structure in **BaI₂(pyz)₆/₂**. Colour code: Ba, pale green; I, purple; N, blue; C, grey. Hydrogen atoms have been omitted.

Figure S5. Thermal ellipsoid (50% probability level) plot of the asymmetric unit of **EuI₂(bipy)₅/₂**. Colour code: Eu, green; I, purple; N, blue; C, grey. Hydrogen atoms have been omitted.
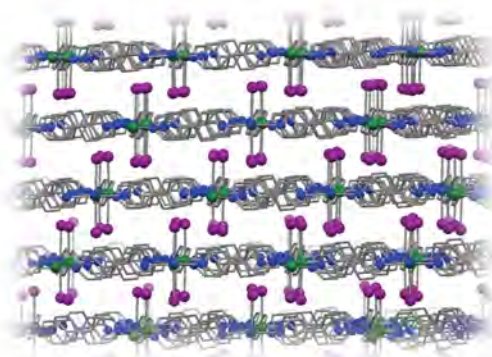
Figure S6. Perspective view of the layer structure in **EuI₂(bipy)₅/₂**. Colour code: Eu, green; I, purple; N, blue; C, grey. Hydrogen atoms have been omitted.

143
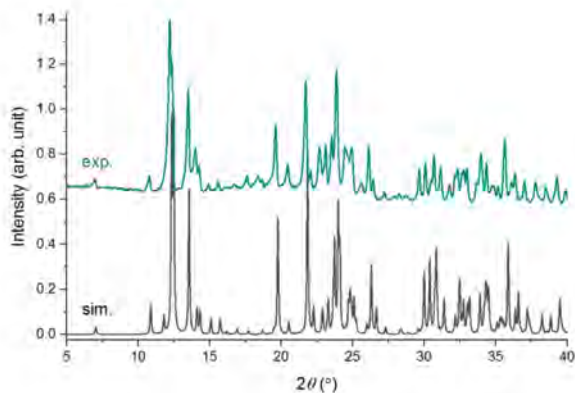
Figure S7. Powder X-ray diffractogram of **EuI₂(pyz)₅/₂** recorded at room temperature (turquoise trace). The grey trace represents the calculated diffraction pattern from the 120-K single-crystal X-ray structure.
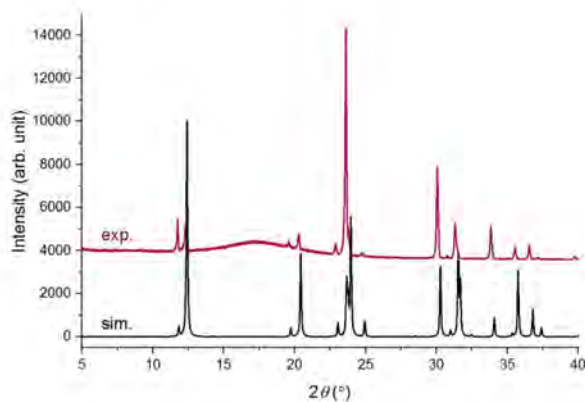
Figure S8. Powder X-ray diffractogram of **BaI₂(pyz)₆/₂** recorded at room temperature (purple trace). The black trace represents the calculated diffraction pattern from the 120-K single-crystal X-ray structure.
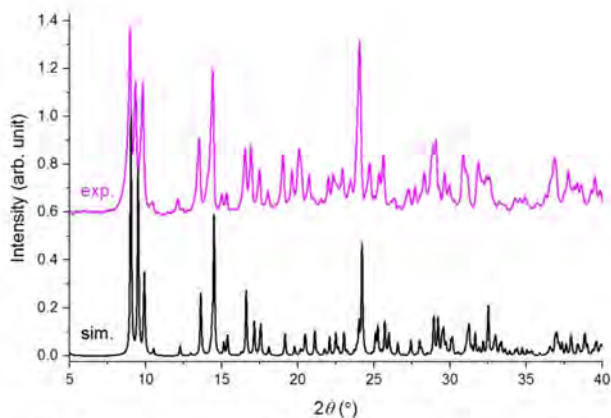
Figure S9. Powder X-ray diffractogram of **EuI₂(bipy)₅/₂** recorded at room temperature (pink trace). The black trace represents the calculated diffraction pattern from the 120-K single-crystal X-ray structure.
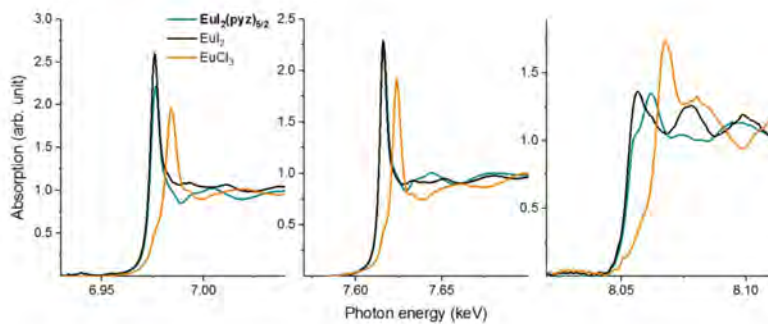
Figure S10. Room-temperature XANES spectra of **EuI₂(pyz)₅/₂** together with the reference samples EuI₂ and EuCl₃ at the Eu L_3, L_2, and L_1 edges.
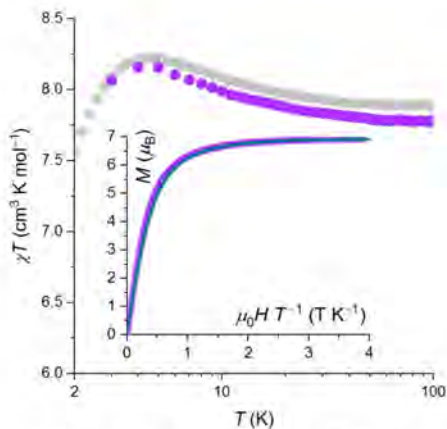
Figure S11. Temperature dependence of the χT ($\mu_0 H = 0.1$ T) product for **EuI$_2$(bipy)$_{5/2}$**. Inset: Field-dependence of the magnetization plotted against $\mu_0 H$ T^{-1}. The solid, turquoise line represents the Brillouin function for $S = 7/2$ with $g = 1.98$.
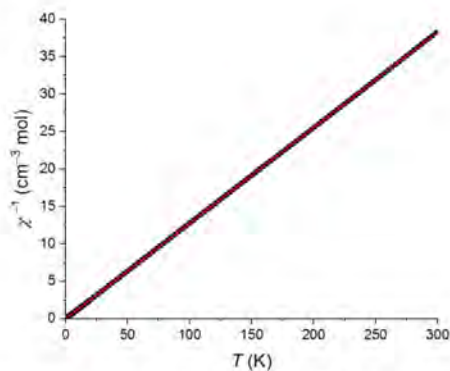

Figure S12. Inverse magnetic susceptibility ($\mu_0 H = 0.1$ T) vs. temperature plot for **EuI$_2$(pyz)$_{5/2}$**. The solid red line is the fit to the Curie-Weiss law (15–300 K) as described in the main text.

11

146
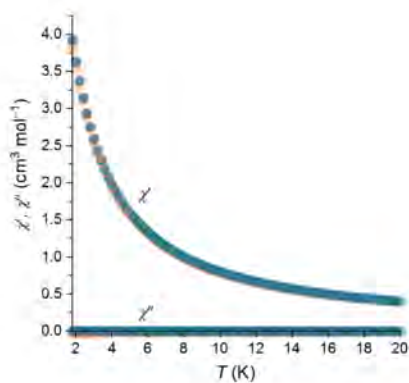
Figure S12. Temperature dependence of the in-phase (χ') and out-of-phase (χ'') component of the ac susceptibility for **EuI$_2$(pyz)$_{5/2}$** obtained with ac frequencies 10 Hz, 100 Hz, 1 kHz, and 10 kHz, and in the absence of a dc magnetic field.
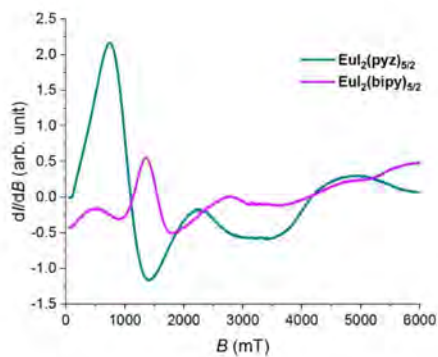
Figure S14. Room-temperature continuous-wave EPR spectra of polycrystalline **EuI$_2$(pyz)$_{5/2}$** and **EuI$_2$(bipy)$_{5/2}$**.
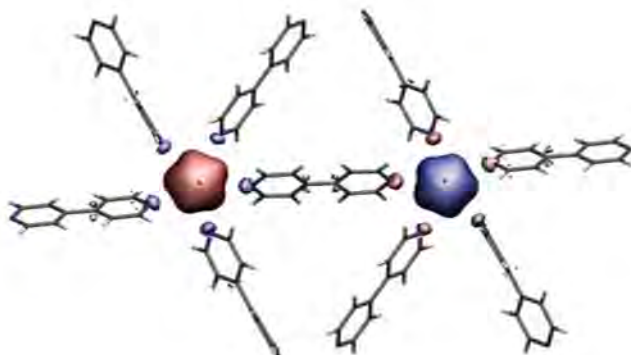
Figure S15. DFT-calculated spin density of the (7,7)-broken symmetry state of a [Eu$_2$I$_4$(bipy)$_9$] fragment in **EuI$_2$(bipy)$_{5/2}$** plotted at an iso-surface value of ±0.001 a.u.
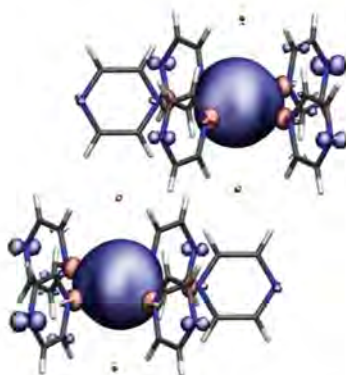
Figure S16. DFT-calculated spin density of the high-spin state of two adjacent [EuI$_2$(pyz)$_5$] fragments in **EuI$_2$(bipy)$_{5/2}$** plotted at iso-surface value of ±0.001 a.u.

148

References

[1] L. J. Bourhis, O. V. Dolomanov, R. J. Gildea, J. A. K. Howard, H. Puschmann, *Acta Cryst.* **2015**, *A71*, 59-75.

[2] O. V. Dolomanov, L. J. Bourhis, R. J. Gildea, J. A. K. Howard, H. Puschmann, *J. Appl. Cryst.* **2009**, *42*, 339-341.

[3] G.M. Sheldrick, *Acta Cryst.* **2015**, *71*, 3-8.

[4] A. Rogalev, J. Goulon, C. Goulon-Ginet and C. Malgrange, *Lecture Notes in Physics*, edited by: E. Beaurepaire, F. Scheurer, G. Krill, J. P. Kappler, **2001**, 565, 60.

[5] R. T. Azuah, L. R. Kneller, Y. M. Qiu, Philip L. W. Tregenna-Piggott, C. M. Brown, J. R. D. Copley, R. M. Dimeo, *J. Res. Natl. Inst. Stand. Technol.* **2009**,114, 341-358.

[6] F. Neese, *WIREs Comput. Mol. Sci.* **2018**, *8*,1327-1332.

[7] a) E. van Lenthe, E. J. Baerends, J. G. Snijders, *J. Chem. Phys.* **1993**, *99*, 4597-4610; b) C. J. van Wüllen, *J. Chem. Phys.* **1998**, *109*, 392-399.

[8] (a) D. A. Pantazis and F. Neese, *J. Chem. Theory Comput.* **2009**, 5, 2229-2238. (b) J. D. Rolfes, F. Neese and D. A. Pantazis, *J. Comput. Chem.* **2020**, 41, 1842-1848.

[9] (a) F. Weigend, Phys. Chem. Chem. Phys. **2006**, 8, 1057-1065. (b) D. A. Pantazis and F. Neese, *J. Chem. Theory Comput.* 2009, 5, 2229-2238. (c) D. A. Pantazis, X. Y. Chen, C. R. Landis and F. Neese, *J. Chem. Theory Comput.* **2008**, 4, 908-919. (d) D. A. Pantazis, F. Neese, *Theor. Chem. Acc.* **2012**, 131, 1292-1298. (e) D. A. Pantazis, F. Neese, *J. Chem. Theory Comput.* **2011**, 7, 677-684.

[10] (a) K. Yamaguchi, Y. Takahara, T. Fueno, in *Applied Quantum Chemistry*; V. H. Smith, H. F. Schaefer, K. Morokuma, Eds.; D. Reidel: Boston, **1986**; p. 155; (b) S. Yamanaka, T. Kawakami, H. Nagao, K. Yamaguchi, *Chem. Phys. Lett.* **1994**, *231*, 25-33.

[11] a) W. Humphrey, A. Dalke, K. Schulten, *J. Molec. Graphics* **1996**, 14, 33-38. b) Website: http://www.ks.uiuc.eu/Researcg/vmd.